THESIS FOR THE DEGREE OF LICENTIATE OF ENGINEERING

Engineering model for curve squeal formulated in the time domain

Ivan Zenzerovic

Department of Civil and Environmental Engineering
Division of Applied Acoustics, Vibroacoustics Group
Chalmers University of Technology
Gothenburg, Sweden, 2014

Engineering model for curve squeal formulated in the time domain
Ivan Zenzerovic

Lic / Department of Civil and Environmental Engineering,
Chalmers University of Technology
Technical report no. lic 2014:4
ISSN 1652-9146

Department of Civil and Environmental Engineering
Division of Applied Acoustics, Vibroacoustics Group
Chalmers University of Technology
SE-412 96 Gothenburg
Sweden
Telephone: +46 (0)31-772 2200

Printed by
Chalmers Reproservice
Gothenburg, Sweden 2014

Engineering model for curve squeal formulated in the time domain

Ivan Zenzerovic

Department of Civil and Environmental Engineering
Division of Applied Acoustics, Vibroacoustics Group
Chalmers University of Technology

Abstract

Curve squeal is a type of railway noise that may arise when a railway vehicle negotiates a relatively tight curve. Squeal is common in curves of a radius lower than 200 meters. A single frequency dominates the radiated sound, which makes squeal a very tonal noise. The high number of tight curves in cities and urban areas, the tonal nature and high noise levels, make squeal a serious source of noise pollution. The rising awareness of the impact of noise on public health increases the need to address the squeal problem. Consequently, there is a need for practical squeal simulation tools. The aim of this thesis is to develop a computationally fast squeal model in the time domain suitable for practical use. For this purpose, an existing squeal model is modified. The tangential contact is modelled using a point-contact model, which considers the contact variables in a global manner. This is in contrast to Kalker's variational contact model which discretizes the contact area into elements. The friction model and contact compliance are defined in a stringent way in relation to Kalker's model. In this way, the point-contact model is able to describe the transition of contact conditions from full stick to full slip. Although the proposed contact model is steady-state, it performs well at high frequencies. An upper limit of applicability of at least 5 kHz was found in the validation of the contact model within the squeal model. Compared to the classical validation with prescribed motion, the inclusion of the system dynamics puts different demands on the contact model. This indicates that contact models should be validated/compared in conditions that replicate their specific application as closely as possible. The engineering model is completed by implementing an existing model for sound radiation from the railway wheel, the implementation of which is validated against BEM results. A parameter study involving lateral creepage, wheel/rail contact position and friction is performed using the proposed squeal model. The investigated parameters show a strong influence on squeal occurrence and amplitudes. With the wheel being an important factor in squeal, the influence of the wheel modal damping is also investigated. Results indicate that increasing only the damping of the mode excited in squeal may not be sufficient. Squeal may then occur involving another mode with another frequency and amplitude. The amount of modal damping required to prevent squeal is relatively low.

Keywords: *Curve squeal, rolling contact, time domain, frictional instability, non-Hertzian contact, tangential point-contact model*

Words, as is well known, are the great foes of reality.

—Joseph Conrad

List of publications

This thesis is written as a self-contained monography. The work presented is based on the following two papers, which are not included due to overlapping material.

Paper I
Towards an Engineering Model for Curve Squeal.
I. Zenzerovic, A. Pieringer and W. Kropp
In *Proceedings of the 11th International Workshop on Railway Noise (IWRN11)*, Uddevalla, Sweden, September 9-13, 2013, pp. 495-502.

Paper II
An engineering time-domain model for curve squeal: tangential point-contact model and Green's functions approach.
I. Zenzerovic, A. Pieringer and W. Kropp
To be submitted, 2014.

Acknowledgements

I started my PhD studies on the 1^{st} of June 2012. Before that time, I can hardly say I understood what research really is. Now, after two and a half years I have come to understand that it's a mix of ups and downs and, of course, luck. My luck is that I'm not alone and there are a number of people I have to thank for their help and support through this "first half" of my PhD "game".

First and foremost, I would like to thank my supervisor, Professor Wolfgang Kropp for his extensive guidance, interesting ideas and discussions that got me to this point. However, if it was not for Dr. Astrid Pieringer, my assistant supervisor who very often acted as the "voice of reason", I would have had a very hard time understanding what I was actually doing. Thank you both for your support and for the extensive guidance.

Thanks to all the PhD students and colleagues at the Department of Applied Acoustics. Guys and girls, it's a pleasure to work with you and to be part of the Applied Acoustics family. Thanks to Börje and Gunilla for their help with all the technical and administrative angles and tasks.

The work presented in this thesis is performed within the project "Abatement of curve squeal noise from trains" (VB11) within the Centre of Excellence CHARMEC (CHAlmers Railway MEChanics). It would be impossible to carry out the present work without the financial support from CHARMEC and the companies supporting it, in particular Bombardier Transportation, Trafikverket, SL and Interfleet Technology. I would like to thank all the people from CHARMEC and the project reference group members.

Thanks to my friends in Croatia and Sweden for their support and all the nice, fun and relaxing moments.

Zahvaljujem se svojim roditeljima i bratu koji su mi svojim primjerom upornog i ustrajnog rada usadili radne navike. Hvala vam na podršci i strpljenju.

Last but not least: Željka, hvala ti na izuzetnom strpljenju koje imaš. Znam da nije uvijek lako biti pored mene, pogotovo dok stvari zaguste, ali nemaš pojma koliko mi to znači.

Contents

List of Figures

List of Tables

List of Symbols

Symbol	Unit	Definition
R	m	Curve radius
W	m	Vehicle bogie wheelbase length
v	m/s	Rolling (vehicle) velocity
v_x,v_y,v_z	m/s	Linear velocity components in the xyz system
ω_z	rad/s	Angular velocity, z component
γ_x	-	Longitudinal creepage
γ_y	-	Lateral creepage
γ_ω	1/m	Spin creepage
μ	-	Coulomb friction coefficient
μ_{RF}	-	Regularized friction coefficient
p_1	Pa	Longitudinal traction
p_2	Pa	Lateral traction
p_3	Pa	Normal contact pressure
s_τ	m/s	Slip velocity components, $\tau = 1, 2$
s	m/s	Absolute value of slip velocity
w_τ	m/s	Creepage contribution to slip-velocity, $\tau = 1, 2$
u_j	m	Wheel/rail displacement difference, $j = 1, 2, 3$
t	s	Time
Δt	s	Simulation time-step length
a_x	m	Contact length in the rolling direction
L	m	Characteristic wavelength of the motion
f	Hz	Frequency
f_d	Hz	Discrete frequency
f_r	Hz	Mode r eigen-frequency
k	-	Carter's creepage coefficient
c	-	Contact ellipse semi-axes ratio
a, b	m	Contact ellipse semi-axes
G	Pa	Material shear modulus
C_{ij}	-	Kalker's creepage coefficients, $i, j = 1, 2, 3$
Δy^{WR}	mm	Wheelset lateral offset
G_{ij}	m/N	Receptance, $i, j = 1, 2, 3$
$S_{G,ij}$	m/N	Constructed receptance-spectrum, $i, j = 1, 2, 3$
g_{ij}	m/N	Green's functions, $i, j = 1, 2, 3$

ξ_i	m	Body displacement response, $i = 1, 2, 3$
Φ_r	-	Mode shape of mode r
m_r	-	Modal mass of mode r
ζ_r	-	Modal-damping factor of mode r
z^W, z^R	m	Wheel and rail undeformed profiles
$d\,(x, y)$	m	Displacement function
Δx, Δy	m	Contact-discretization elements dimensions
N_P	-	Number of elements in the contact discretization
$A_{i,j}$	m^3/N	Elastic half-space influence coefficients, $i, j = 1, 2, 3$
A_τ	m/N	Tangential contact compliances, $\tau = 1, 2$
r	m	Wheel radius
W^W	W	Radiated sound power from the wheel
S	m^2	Surface area
σ_a, σ_r, σ_t	-	Sound-radiation efficiencies
n	-	Number of wheel nodal diameters
w, w_{web}	m	Wheel tyre and web width
$\overline{\tilde{v}^2}$	m^2/s^2	Spatially-averaged mean-square velocity
L_W	dB rel. $10^{-12}W$	Sound power level
v_X, v_Y, v_Z	m/s	Wheel BE model velocities
v_x, v_y, v_φ	m/s	Wheel cross-section model velocities
φ	rad	Circumferential angle
L_{F_2}	dB rel. 1 N	Lateral-contact force level

Chapter 1

Introduction

1.1 Background

Railways are nowadays considered as one of the most efficient means of transportation of both people and material. They are also regarded as an environmentally friendly means of transportation because of their low CO_2 emission levels. Railways are responsible for 0.2% of greenhouse gas emissions (2012 year levels) in the 28 European Union member states (EU-28) [3]. Moreover, CO_2 emission levels from railways decreased by 46.8% between the years 1990 and 2012 [3]. At the same time, railways account for 10.8% of transported goods (year 2012) [20]. In comparison, road transport accounts for 18.6% of greenhouse gas emissions [3] and 44.9% of freight transport volume (2012 year levels, EU-28) [20]. Despite the large difference in transported goods, railways are indeed environmentally friendly.

Compared to the emission of greenhouse gasses, noise is not considered an environmental pollution in the classical sense. However, the concern of noise impact on public health is rising and noise pollution is being considered more often [1]. This influences the operation of existing railway systems and development of new systems.

The location of railways, tram and metro systems in areas with high population densities has led to an increased awareness of railway noise. Awareness has risen in particular since the 1960s, along with the amount of conducted research [72]. Research provided many insights in the mechanisms behind railway noise and measures used to mitigate it. Still, the treatment of certain railway noise issues is complaint-driven [2].

The overall costs of railway operation increase with the addition of noise mitigation measures. This increase is further driven by the fact that different noise sources require different measures. The most important sources of railway noise caused by forces from the wheel/rail contact are rolling noise, curve squeal and ground borne vibration and noise. They are usually referred to as wheel/rail noise and are significant noise sources in a broad range of vehicle speeds (roughly 30 - 200 km/h).

Other sources of railway noise include aerodynamic noise (high speeds) and power unit noise (low speeds). Despite the fact that different wheel/rail noise types originate from the same area, the nature of these types of noise is very different. There is no universal solution for the mitigation of wheel/rail noise and each source has to be approached differently.

In curve squeal and rolling noise, contact forces excite the wheel and rail, which are the main sound radiators. Rolling noise is the most common type of wheel/rail noise. The vertical force oscillation develops due to wheel and rail roughness. This force then excites the wheel and rail into vibration, which results in sound radiation, see Figure 1.1. This source of railway noise is well investigated and effective mitigation measures exist. Rail grinding, wheel re-profiling and rail and wheel dampers are all effective mitigation measures for rolling noise [72, 2].

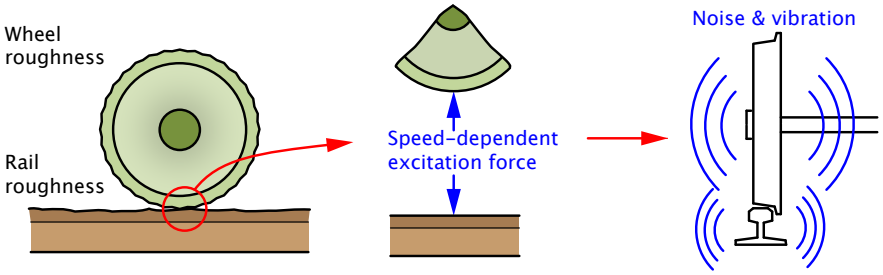

Figure 1.1: Generation of rolling noise from wheel and rail roughness [2].

Compared to rolling noise, which is present as long as the vehicle is moving, curve squeal noise originates at discrete locations (curves) along the track. In contrast to rolling noise, squeal is a consequence of the tangential contact phenomena. Significant research has also been conducted in this topic, although questions about the excitation mechanisms and influencing parameters still remain open. Mitigation measures like track lubrication, friction-modifier application, wheel dampers and special bogie designs were used with mixed results [2]. The application of friction modifiers on the track is a common and efficient measure for squeal mitigation. However, it is related to relatively high costs of implementation and requires regular maintenance. In addition, the use of friction modifiers may also have a negative environmental impact (ground pollution).

Mitigation of railway noise is becoming increasingly important for railway vehicles and components manufacturers, infrastructure administrators and traffic operators. When devising and implementing mitigation measures, the sustainability aspect should be considered as well. This is something neither simply nor often done. Mitigation measures should be implemented in the design phase of new vehicles and tracks, instead of being implemented on a complaint-driven base. For this purpose, manufacturers have to be provided with tools to verify their designs and eliminate guess-work.

TWINS [73] is a commercial tool used for prediction of radiated sound from railways. The tool is suitable for rolling noise computations with limited applicability

to curve squeal. In spite of the existence of a number of models for curve squeal, commercial tools for its prediction are virtually non-existent. Reasons behind this are threefold. Firstly, many uncertainties related to the curve squeal phenomenon exist. Secondly, the target group for such a tool is rather limited. Finally, current legislation is not concerned with the tonality of railway noise, which is what makes curve squeal a significant annoyance.

Once the legislative policy makers start imposing limits on squeal noise levels and its tonal content, simulation tools for curve squeal will become a necessity. Therefore, it is worthwhile to work towards a prediction tool for curve squeal, which can be used in engineering practice. The same is true for the development of a better understanding of squeal, its generation mechanisms and influencing parameters.

1.2 Aim and scope of the thesis

The aim of this thesis is to develop a computationally fast model for curve squeal in the time domain, which is suitable for practical engineering use. Of special interest is the model of the wheel/rail rolling contact and the required level of modelling detail. Apart from the model formulation, efforts have been put into the investigation of parameters that influence curve squeal.

The engineering model for squeal is based upon the time domain wheel/rail interaction model developed by Pieringer [55, 56]. An efficient tangential contact model is formulated and implemented in the interaction model. The squeal model is then extended with an existing simple model for sound radiation from the railway wheel developed by Thompson and Jones [74]. This completes the engineering model for curve squeal.

Contact models differ in their properties, consideration of contact variables and computational costs. Special emphasis is put on the contact modelling approach, including the definition of contact variables. The friction model and the contact stiffness are defined in a stringent manner for the proposed contact model. This is of utmost importance if the results of the proposed models are to be compared to the reference model [56]. Moreover, the stringent definition of friction and contact stiffness are important if the contact phenomena are to be modelled in the same way.

Curve squeal is a complex phenomenon and, owing to its high non-linearity, small variations in kinematic or dynamic parameters can lead to significantly different results. To investigate this, the most important kinematic and material parameters are considered in the lateral creepage/friction and wheel modal damping parameter studies.

Several simplifying assumptions limit the proposed model. Firstly, roughness of the wheel and rail is not considered in the model. Secondly, curving is considered to be steady-state, meaning that the kinematic parameters of the wheelset do not change throughout the curve. Friction properties are constant along the track as well. Finally, the model includes only one suspended wheel with a single contact

point between the wheel and the rail.

1.3 Outline

The thesis is divided into six main parts as follows.

Chapter 2 introduces the problem of curve squeal. A general characterization of the problem is given, along with the necessary conditions for squeal to occur. The mechanisms considered to be responsible for squeal are discussed as well. Finally, the commonly used mitigation measures for curve squeal are described. The aim of this chapter to point out the still incomplete understanding of squeal and give the motivation for further research on curve squeal. In general, *Chapter 2* introduces basic concepts and the terminology used in later chapters.

Chapter 3 gives a review of existing models for curve squeal. Special attention is given to the classification of squeal models into time-domain and frequency-domain models, with a greater emphasis on time-domain models. Models for the rolling contact are also reviewed because of their importance in the squeal model. Additionally, the conditions present in the contact area during squeal are discussed.

The engineering model for curve squeal is elaborated in *Chapter 4*. The complete chain from source to radiated sound power is covered. Parts of the model are explained in detail, with special emphasis on the contact model formulation.

Validations of the sound-radiation model implementation and the rolling-contact model are presented in *Chapter 5*. The implementation of the simple model for sound radiation is validated first, followed by the detailed validation of the contact model. A two-fold approach is proposed for validating the contact model. The proposed approach gives more information about the applicability of a contact model in squeal simulations.

Chapter 6 presents the application of the engineering model for parameter studies. The influence of lateral creepage and wheel/rail contact position, which are related to the vehicle curving behaviour, is investigated, along with wheel/rail friction and wheel modal damping. Besides being a showcase for the engineering model, these studies serve as investigations of the influencing parameters of curve squeal.

Finally, conclusions are given in *Chapter 7*, along with some feasible directions for future work.

Chapter 2

On curve squeal

2.1 The phenomenon of curve squeal

Curve squeal is a strong tonal noise that may occur when a railway vehicle negotiates a relatively tight curve. The definition of a tight curve is given in relation to the vehicle bogie wheelbase. According to Rudd [63] and Remington [62], the curve radius/bogie wheelbase ratio R/W is a good indicator whether squeal will occur or not. Generally, if R/W<100, curve squeal is expected to occur. However, this rule is not universal and squeal can be encountered even for R/W ratios higher than 100. A practical guideline for squeal occurrence in curves of different radius was given by Thompson [72]:

$R \geq 500\,\mathrm{m}$,	mostly no squeal;
$200\,\mathrm{m} < R < 500\,\mathrm{m}$,	sporradic occurrence;
$R \leq 200\,\mathrm{m}$,	common occurence.

During squeal a single frequency (tone) dominates the radiated sound. Main tones of curve squeal are found in the frequency range 250 Hz - 5 kHz [72, 23], and sometimes even up to 10 kHz [77]. The combination of the tonal nature and sound pressure levels of up to 130 dB at 0.9 m from the wheel [63] make squeal one of the loudest and most disturbing types of railway noise. Additionally, the high number of tight curves in cities and urban areas leads to a significant proportion of urban population being exposed to curve squeal. This makes it a potential hazard for public health.

The tonal nature of squeal is related to the railway wheel dynamics. Frequencies observed during squeal events correspond to eigen-frequencies of axial wheel modes with zero nodal circles [77, 42]. Besides the excited wheel mode eigen-frequency, frequencies corresponding to higher harmonics of the excited mode are often observed. These observations point to the non-linear nature of squeal [23]. Moreover, the close match between squeal frequencies and wheel eigen-frequencies indicates the importance of the wheel dynamics. The higher vibration response of the wheel compared

to that of the rail [77], coupled with its high sound radiation efficiency [74, 72] make the wheel a very important factor in squeal.

In order to develop and sustain squeal, the wheel/rail vibrating system needs an energy input. It is recognized that this comes from the relative motion between the wheel and rail during curving. Rudd [63] distinguished between three different energy sources, calling them *"models for the mechanism of wheel squeal"*:

1. Flange rubbing;

2. Differential longitudinal slip;

3. Lateral creepage.

Remington [62] also referred to these energy sources as mechanisms. However, in the present work, they are referred to as energy sources as they actually only provide the input energy for the vibrating system. The case of flange rubbing should be considered separately because not only can it be considered as a separate energy source, but it can also result in a phenomenon different than curve squeal. Mechanisms that are held responsible for the generation of squeal are discussed in Section 2.2.

Energy inputs by flange rubbing and differential longitudinal slip were discredited for the case of curve squeal by field observations and laboratory measurements [62, 42]. This seems to leave lateral creepage as the only energy source during squeal.

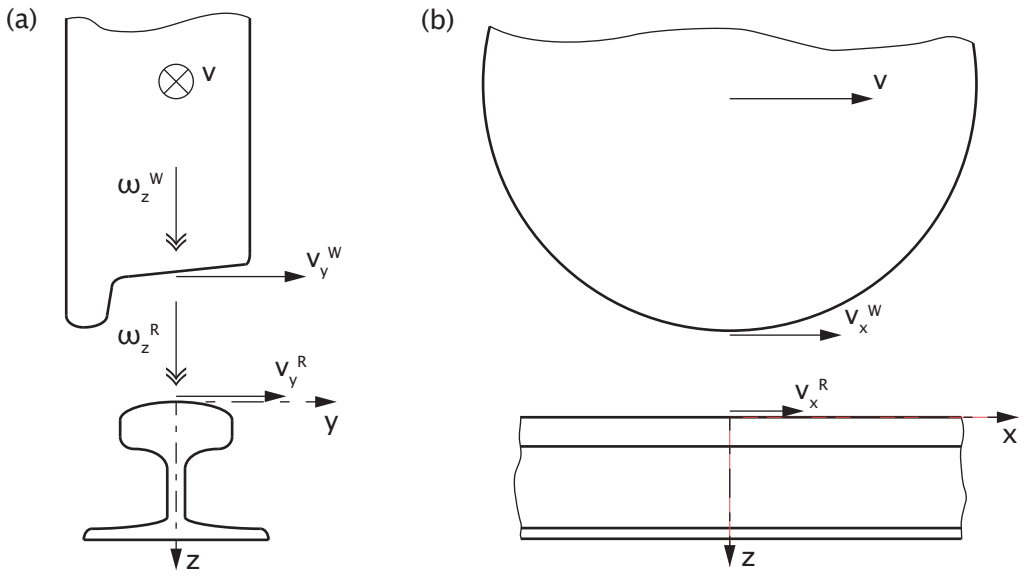

Figure 2.1: Relative velocities between wheel and rail: (a) lateral velocities; (b) longitudinal velocities.

Creepage is defined as the relative velocity between wheel and rail normalised with the rolling (vehicle) velocity v. Three types of creepage are observed in the

wheel/rail contact area: longitudinal (γ_x), lateral (γ_y) and spin creepage (γ_ω), defined as:

$$\gamma_x = \frac{v_x^W - v_x^R}{v}, \tag{2.1}$$

$$\gamma_y = \frac{v_y^W - v_x^R}{v}, \tag{2.2}$$

$$\gamma_\omega = \frac{\omega_z^W - \omega_z^R}{v}. \tag{2.3}$$

The relative rail (superscript index R) and wheel (superscript index W) velocities are defined in Figure 2.1 (a) and (b). Longitudinal creepage arises in cases of braking, acceleration and due to differential slip during curve negotiation of rigid wheelsets (rigid connection between left and right wheel). Spin creepage is a consequence of the wheel/rail contact angle (due to wheel conicity) and vehicle yaw velocity during curving [6]. Finally, lateral creepage arises mainly during curve negotiation when the wheel forms an angle of attack (yaw angle) relative to the rail in the travel direction, see Figure 2.2. Both the lateral and the longitudinal creepage are crucial for the build-up of contact forces required for acceleration, braking and curving.

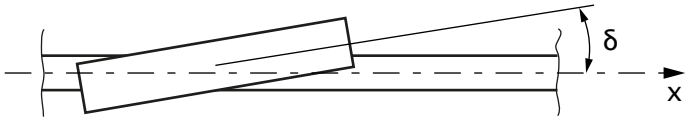

Figure 2.2: Definition of the wheel/rail angle of attack.

It is the front wheelset of the leading vehicle bogie that develops the largest angle of attack during curve negotiation. The exact amount of the angle of attack, and consequently the amount of lateral creepage, depends on the vehicle curving behaviour and curve radius. The wheelset kinematics and the dynamic forces that act on the vehicle cause the wheelset to displace towards the curve outer rail. The outer wheel tends to come into flange contact for high values of the angle of attack and of the wheelset lateral displacement, which arise in tight curves. With the contact positioned on the rail head and wheel tread, and with high lateral creepage, the inner wheel is considered to be most susceptible to squeal [72]. However, squeal was occasionally observed on the outer wheel, which is in flange contact [23, 18, 69]. Flange contact may therefore contribute to squeal, but the conditions leading to this situation are still unknown.

Besides the described kinematic parameters, curve squeal was found to be strongly influenced by friction properties in the wheel/rail contact [62]. The root of this influence comes from the contact, which couples the wheel and rail dynamics. In this coupling, the friction law determines the relation between vertical and tangential forces.

The parameters influencing squeal can be classified in three groups [77]:

1. Local kinematic parameters of the wheel/rail contact;

2. Contact friction law;

3. Wheel modal parameters.

Each group is related to a specific railway vehicle property or environmental factor. As discussed above, local kinematic parameters are mainly related to the vehicle curving behaviour and track geometry. In addition, the wheel and rail profiles have an influence as well. The friction law is closely influenced by weather conditions, track pollutants and eventual lubrication, while the wheel modal parameters depend solely on the wheel design and material.

Due to the large number of factors influencing curve squeal [2] many researchers found squeal to be an erratic phenomenon strongly influenced by small variations of operating and weather conditions [23, 77, 62]. Repeatability of measurements can also be an issue and a significant scatter of measured data is observed [62]. In addition, squeal seems to be related to specific trains [23]. Different trains show different squeal behaviour possibly due to different curving behaviour and/or different wheel profiles in the worn state. Moreover, the possibility of varying conditions along the curve complicates matters further.

As discussed, a high level of uncertainty is related to curve squeal. Despite the fact that significant research on curve squeal has been made, no conclusive evidence is found about the exact conditions nor excitation mechanisms behind squeal. In the next section, excitation mechanisms that are held responsible for squeal are discussed in more detail. This creates a foundation for a further discussion of existing squeal models and mitigation measures.

2.2 Mechanisms responsible for curve squeal

As discussed in Section 2.1, curve squeal is a phenomenon in which the wheel and rail dynamics, wheel/rail contact mechanics and friction law interplay and result in unstable vibrations. These self-induced vibrations with lateral creepage as the energy source are the result of non-linearities present in the wheel/rail system. Non-linearities are present in the wheel/rail contact, but the contact itself is not enough for the development of self-sustained vibrations.

For squeal to develop and persist, additional mechanisms are needed. The two most discussed mechanisms are the falling friction law and the geometric (modes) coupling.

2.2.1 Slip-velocity dependent friction law

Rudd [63] proposed the falling friction curve as the mechanism responsible for curve squeal. The friction coefficient between the wheel and rail is considered to be a function of slip velocity with a negative friction slope as shown in Figure 2.3.

Measurements of wheel/rail friction [62, 72] show a decrease of the friction coefficient with increasing slip velocity (or creepage). This decrease has direct consequences on the contact force. Sliding occurs when the tangential force reaches the

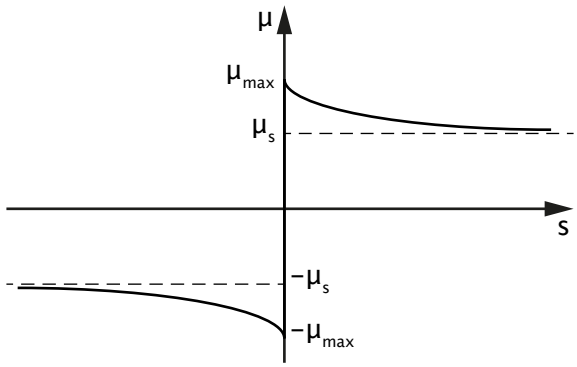

Figure 2.3: Example of a slip-velocity dependent friction law with decreasing friction value for increasing relative slip velocity.

static friction limit $\mu_{max}F_3$, where F_3 is the vertical contact force and μ_{max} is defined in Figure 2.3. The friction coefficient value then decreases with increasing slip velocity $s \neq 0$. With the dynamic (sliding) friction lower than the static one, sliding continues until the restorative (elastic) forces of the wheel drop below the dynamic friction force value. Stick between wheel and rail is then re-established and the force builds up until it again reaches the static friction limit. This process repeats itself with frequency dictated by the wheel dynamics.

The falling friction law was interpreted by Rudd [63] as negative damping. The negative slope of the friction curve is responsible for feeding energy into the system in each period of vibration. This results in self-induced and self-sustained vibrations of the wheel and rail which persist as long as there is an external source of energy (as lateral creepage during curve negotiation).

2.2.2 Geometric coupling of wheel modes

Geometric coupling between the degrees of freedom of the system is another mechanism held responsible for the occurrence of stick-slip motion. In contrast to the falling friction mechanism, in geometric coupling the wheel deformation pattern is responsible for the sustained energy input. This mechanism is well investigated in the context of automotive disc-brake squeal [68, 29, 67].

In Figure 2.4 the schematics of the single degree of freedom systems commonly used to illustrate the mechanisms behind stick-slip are shown. The model layout depends on the excitation mechanism considered. In case of the falling friction mechanism, Figure 2.4 (a), a single stiffness element is enough. The friction law between the mass and the sliding surface is responsible for stick-slip, as discussed in Section 2.2.1.

In geometric coupling, Figure 2.4 (b), at least two stiffness elements are required to describe the coupling between directions. Because of the coupling, forces acting in the vertical direction cause displacements in both vertical and lateral directions. In addition, friction couples the lateral and vertical forces, which adds to the coupling

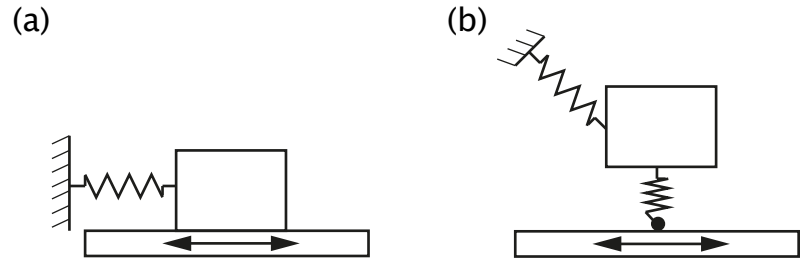

Figure 2.4: Schematic of the single degree of freedom model usually used to illustrate the mechanism behind the stick-slip instability [33]: (a) falling friction mechanism; (b) geometric coupling mechanism.

of displacements. The friction coefficient affects the coupling strength and instability is expected to occur if friction is above a certain threshold value [33]. The geometric coupling mechanism implies that stick-slip instability can also occur in cases with constant friction. This is supported by simulation results from Brunel et al. [12], Glocker et al.[23] and Pieringer [56], and experimental evidence presented by Koch et al. [42].

When considering a railway wheel, the geometric coupling of different directions may be present within a single wheel mode. Sometimes the coupling is due to the presence of more wheel modes with closely spaced eigen-frequencies. Glocker et al. [23] found that in their case three modes have to be present with similar eigen-frequencies for squeal to occur. The exact number of required modes may depend on the wheel properties, friction and the wheel/rail contact position, which all influence the coupling strength. Because geometric coupling is observed in mode shapes of the wheel, this mechanism is sometimes referred to as modes coupling.

While the falling friction law leads to negative damping in the system equations, geometric coupling results in the asymmetry of the system's stiffness matrix [56]. Both terms, when appearing in the system equations, can be used to mathematically explain the occurrence of instabilities and stick-slip oscillations.

Finally, results from Chiello [14], Glocker [23] and Pieringer [56] indicate the possibility that both falling friction and coupling mechanisms may coexist in reality.

2.3 Mitigation measures

Two groups of mitigation measures can be identified with respect to their working principle. The first group mitigates squeal by disabling the generation mechanism responsible for squeal. The second group reduces the input energy in the wheel/rail system. In practice, mitigation measures influence both the generation mechanism and the input energy at the same time, but to various degrees.

Mitigation measures can be also classified according to where the measure is implemented. Infrastructure and rolling stock measures can be identified accordingly. In the following section, mitigation measures are classified according to the location

where the measure is implemented.

2.3.1 Infrastructure measures

Infrastructure measures found in practice mainly aim at controlling friction, either by lowering it or changing the shape of the friction curve. Lubricants are used to lower the friction value, which should not be too low and thus affect traction and braking performance [2]. Lubricants should therefore be applied only on the rail gauge corner and wheel flange.

Control of the friction curve is carried out by application of friction modifiers. They do not aim at lowering friction and are suitable for application on the rail head and wheel tread [2]. Modifiers are usually applied to reduce wheel/rail wear and rail corrugation in curves [2, 46]. Practical applications have shown that friction modifiers help to avoid squeal and flanging noise as well [2]. The characteristic of different friction modifiers is presented in Figure 2.5.

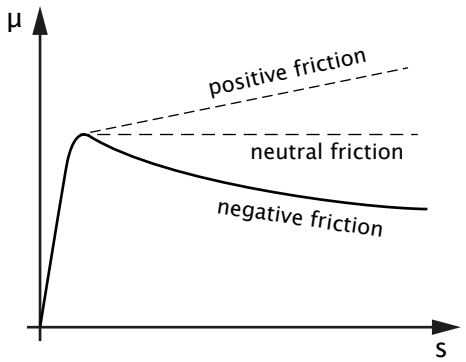

Figure 2.5: Characteristics of different friction modifiers [46].

Friction modifiers are efficient in cases where squeal is a result of the falling friction mechanism discussed in Section 2.2.1. The negative slope of the friction curve is altered either into a neutral or a positive friction curve, as shown in Figure 2.5.

Friction modifiers may provide significant benefits, but are inevitably followed by implementation and maintenance costs. Controlled field tests are important when applying such a system, along with proper maintenance and the determination of optimal dosage under various weather conditions [2]. Curve squeal was observed to occur much more seldom during wet weather [72]. Application of water as a friction modifier may therefore give satisfactory results and also provide a viable and environmentally friendly solution.

Field observations show mixed results in the case of application of friction modifiers. Observations vary from significantly shorter duration of squeal events, but with the same overall noise level, to significant attenuation of tonal components and overall noise levels [2]. Limited benefits of friction modifiers were observed in mea-

surements on Australian railway lines [18]. In general, friction modifiers are unable to completely eliminate squeal.

Rail gauge corner and wheel flange lubrication show promising results in cases where flange contact influences curve squeal. Measurements on the Australian railway lines [18], where the outer rail gauge face and gauge corner were lubricated, have shown promising results. Squeal was successfully mitigated in that case. However, the mechanism responsible for squeal in the Australian case is not completely clear.

Of other infrastructure measures, asymmetric rail profiles (originally used for reducing wear) and gauge narrowing can produce beneficial results. These measures aim at improving the vehicle curving behaviour and therefore lower the input energy in the wheel/rail system (lower lateral creepage). A different curving behaviour may also result in a change of the wheel/rail contact position, with the contact located at a more favourable position. This is beneficial for cases where squeal is caused by geometric coupling, as the strength of the coupling depends on the location on the wheel tread.

Mixed results were obtained with asymmetric rail profiles [72, 2]. Where benefits were noticed, lower noise levels were measured, but the number of squeal events remained the same [2]. Tests with narrower track gauges have also shown promising results [72, 2].

2.3.2 Rolling stock measures

Rolling stock measures include vehicle-mounted lubrication and/or friction modifier application systems, wheel dampers and special bogie designs. Lubrication and the application of friction modifiers were already discussed in Section 2.3.1.

Special bogie design are primarily used for improving the vehicle curving behaviour. As a consequence, lateral creepage is reduced and a potentially more favourable wheel/rail contact position is achieved. Designs with steerable axes, independent wheel axles and active steering control are some possible options [72, 2]. However, high-speed stability has to be considered in the bogie design. Unfortunately, the stability and curving performance requirements stand in contradiction [6].

Wheel damping solutions were shown to be effective in reducing rolling noise [72]. They were also found useful for mitigation of squeal. Frequently used wheel damping treatments include resilient wheels, constrained layer damping solutions, tuned absorbers, ring dampers and multi-material wheels [72]. Figure 2.6 shows some examples of wheel damping treatments.

Damping reduces the wheel response amplitudes at resonances, which has a twofold effect on curve squeal. First, the strength of the geometric coupling is reduced, and second, the sound radiation from the wheel is reduced. Unfortunately, in practice it is very hard, if not impossible, to determine which effect is responsible for the reduction in noise levels.

According to Thompson [72], small increases in wheel damping may be enough to eliminate squeal. Squicciarini et al. [69] have shown that squeal does occur on

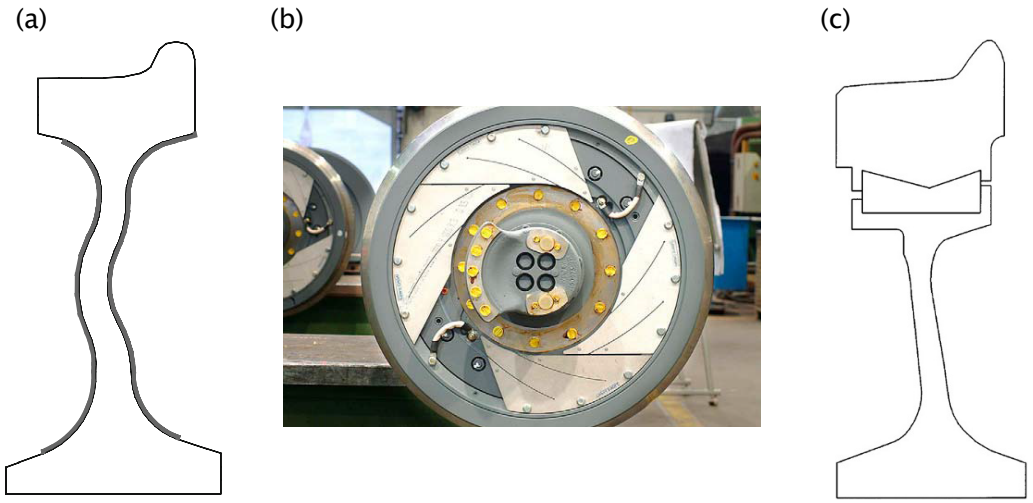

Figure 2.6: Examples of wheel damping treatments [72]: (a) constrained layer damping; (b) tuned absorber; (c) resilient wheel.

vehicles equipped with resilient wheels. However, various practical cases were observed where wheel damping did not prevent squeal [2]. Cigada et al. [15] concluded that the use of resilient wheels to combat curve squeal is not expected to provide any benefits. This conclusion is based on the vibro-acoustic characterization of a resilient wheel. Wheel modes excited in squeal were not found to be sufficiently damped in order to eliminate squeal. This conclusion may be true for the case of squeal caused by the falling friction mechanism, but resilient wheels show a significantly weaker geometric coupling between the lateral and vertical directions [15], which might be beneficial.

When damping is low, small variations in damping lead to high variations of the radiated sound, as shown by Merideño et al. [48] and in line with the earlier statement from Thompson [72]. When damping is high, variations in it do not affect the radiated sound significantly. A correct determination of wheel damping values is therefore very important.

From the discussion above, two different critical wheel damping values can be deduced. The first is related to the squeal generation mechanism (squeal does not develop), and the second is related to the sound radiation from the wheel (attenuation of noise). Critical damping in the latter case should be defined in relation to a satisfactory attenuation of noise levels. Both could be important in practical considerations.

This section is concluded with a reference to Remington [62], who identified the main ways to mitigate curve squeal rather early. He recognized the importance of all parameters discussed above: wheel/rail friction, curving performance and wheel damping.

Chapter 3

Review of existing models

In this chapter a review of existing models for curve squeal is given first. The models are categorized according to the domain in which they operate. Models in the frequency and the time domain are distinguished.

Secondly, a review of wheel/rail rolling contact models is given. Types of contact relevant to wheel/rail contact situations are presented, along with different solution approaches. Specific contact conditions present during squeal are discussed as well. The general structure of a contact model is then presented, followed by the review of selected contact models.

3.1 Models for curve squeal

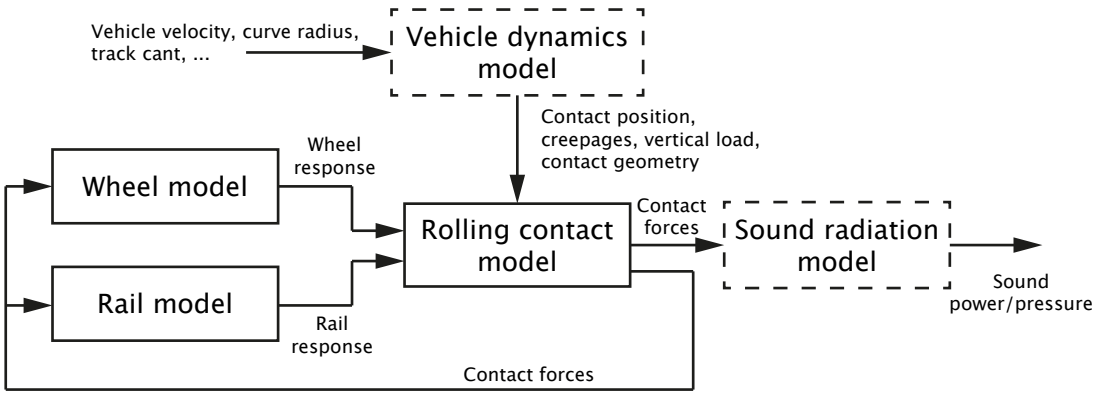

Figure 3.1: Typical structure of a model for curve squeal

A typical structure of models for curve squeal can be identified, which is independent of whether the model is in the frequency or time domain. Figure 3.1 shows the typical structure of a squeal model. Models typically consist of three or more sub-models where the most important are the wheel and rail dynamics and the rolling

contact sub-models. The friction law is usually included in the contact model. Some models are extended with the sound radiation sub-model, while others even include simulations of the vehicle curving behaviour.

For each model reviewed in the following sections, the considered instability mechanism is mentioned, along with a short description of the wheel and rail models and the contact model. Some general findings and main conclusions are given for some models.

3.1.1 Frequency-domain models

Frequency-domain models are obtained either from simple linear models of the wheel/rail system, or by linearisation of non-linear equations that belong to complex models. The exact shape and form of the system governing equations depends on the level of modelling detail. This varies among the reviewed models and is influenced by the wheel and rail dynamic models, contact modelling and the used friction law.

With frequency-domain models the system response is evaluated over the frequency range relevant for squeal, usually 20 Hz to 5 kHz. The occurrence of squeal is determined, along with the excited wheel modes and squeal frequency. Different parameters and curving situations can be investigated in a systematic way using frequency-domain models. In the reviewed literature, they are used to:

- determine the stability of wheels in the vehicle bogie, i.e. which wheels are prone to squeal [23, 49, 81];
- determine the stability of wheel modes, i.e. which modes are prone to squeal [14, 27];
- determine the wheel damping required to eliminate or mitigate squeal [63, 75];
- investigate the influence of kinematic parameters like rolling velocity [75], lateral contact position [19, 49], curve radius [63] and presence of two wheel/rail contact points [69];
- investigate the relation between friction properties and squeal [30].

One of the first models for curve squeal was developed by Rudd [63], further elaborating on the work of Stappenbeck [70]. Rudd considered the wheel as a single degree of freedom system, which was introduced in the model with its impedance. The impedance was experimentally measured and the lateral dynamics were considered. The rail dynamics were not included, which can be interpreted as if the rail was rigid.

Rudd considered a point contact on the wheel. At the contact point, the vertical and lateral forces are coupled by the friction law. The falling friction law adds a term in the governing equations, which was interpreted as negative damping. From the mathematical point of view, this damping term causes instability and therefore squeal.

A significant number of subsequent models were based on Rudd's approach. For example, van Ruiten [75] used Rudd's model to investigate the influence of rolling velocity and wheel damping on curve squeal. Van Ruiten's main question was how the occurrence of squeal can be controlled. In order to answer this question he compared simulation results with measurements and, thus, he validated Rudd's model [63].

Later frequency-domain models were inspired by Fingberg's time-domain model [21], see Section 3.1.2. Fingberg used three sub-models: the wheel, the rail and the contact. Following suit, de Beer et al. [19] developed a frequency-domain model containing the three sub-models. The wheel and rail dynamics were included with mobilities obtained from the TWINS software [73], along with the contact spring mobility. Kalker's linear theory [35] was used to solve the contact problem. The friction law of Kraft [43] was implemented, which is an analytical formulation of measured falling friction characteristics. The vertical, lateral and vertical-lateral coupling dynamics were considered. The inclusion of the coupling dynamics is a significant extension of the model. This was included to investigate the influence of the normal force variation on squeal. The coupling dynamics were seen to have a significant influence on squeal frequencies. Especially the lateral wheel/rail contact position is seen as important because it influences the coupling dynamics. Nonetheless, de Beer et al. [19] concluded that the falling friction is the main cause of squeal. Conclusions were based on stability analyses: the friction law was linearised and the Nyquist criterion applied.

Xie et al. [81] extended de Beer's model to include simulations of the vehicle curving behaviour. Kalker's FASTSIM [36] with the falling friction model from Kraft [43] was used for curving behaviour simulations. The incidence of curve squeal for different curving cases and vehicles was then investigated using the model of de Beer et al. [19].

Hsu et al. [30] applied de Beer's model in a similar way. The model was simplified and the normal contact force was now considered constant. The model was validated against test-rig measurements. This can be also considered as a validation of de Beer's model [19], though a simplified version of it was used.

Monk-Steel et al. [49] took a similar approach to Hsu et al. The model was extended to take into account displacements in all three directions plus the three rotations. The wheel and rail were included with mobilities obtained from their modal parameters. A finite element (FE) model of the wheel was used, while the rail was described using two models: one for the vertical dynamics and another for the lateral and torsional dynamics. The contact model was also more complex, consisting of two sub-models. Kalker's linear theory [35] was used for the linearly increasing portion of the friction curve. The model from Vermeulen and Johnson [76] was used for the negative-sloped portion of the curve.

Heckl and Abrahams [27] developed a frequency-domain model from the time-domain model described in Section 3.1.2. The model was developed for the purpose of determining wheel modes susceptible to squeal. The complex eigen-frequencies were determined from the integro-differential equation of the linear system.

Finally, a recent model for squeal was developed by Squicciarini et al. [69]. A frequency-domain model similar to Hsu's model [30] was extended to account for two-point contact on the wheel. This is a significant extension, as squeal was observed in conjunction with flange contact. Squicciarini included the wheel using its mobilities with wheel parameters tuned to match measurements. A resilient wheel was considered. The rail was modelled using the same approach as in Monk-Steel et al. [49]. Kalker's FASTSIM [36] was implemented to couple the wheel and rail, along with Kraft's falling friction model [43]. The system was then linearized and unstable frequencies determined for a defined parameter space.

3.1.2 Time-domain models

Time-domain models have the capability to include non-linearities present in the wheel/rail system. Moreover, they are able to determine the amplitudes of squeal, which is a very important factor in evaluating squeal severity. Higher harmonic components in the system response can also be determined.

Schneider and Popp's model [64] for curve squeal is among the first squeal models formulated in the time domain. The motion time-history was determined from non-linear differential equations that describe the system dynamics using a Runge-Kutta routine. While the rail was considered rigid, the wheel FE model was based on ring elements from which modal parameters were obtained. Modal transformation techniques were used in the determination of the wheel displacement response. The wheel/rail contact was treated as a point contact where the friction is described by Kraft's falling friction model [43]. In addition, the radiated sound was evaluated using the Rayleigh integral for a baffled plate.

A subsequent model by Fingberg [21] included more elaborate wheel and rail models, a semi-transient rolling-contact model and evaluation of the radiated sound. While the wheel was still modelled using FE, half of a wheelset was considered. The rail was described using two models: one for the lateral dynamics and the other for the longitudinal dynamics. Modal expansion techniques were used to determine both the wheel and rail receptances. For the contact model, Fingberg [21] used Kalker's linear theory [35] extended with the first-order system of Knothe and Groß-Thebing [39]. This semi-transient model was an attempt to take into account transient contact conditions present during squeal[1]. The friction law of Kraft [43] was implemented.

To determine the radiated sound from the wheel, Fingberg combined the boundary element method and modal expansion techniques. The contribution of each wheel mode to the radiated sound was evaluated separately. The partial contributions of wheel modes are then summed to obtain the overall radiated sound.

Periard [54] further extended Fingberg's model. The wheelset model was mainly retained, but a discretely supported rail was included. The rail modal parameters were obtained from a FE model and the rail was, as the wheel, included with its

[1] As will be seen in Section 3.2.3 the implemented contact model is not a fully transient model.

differential equations. Moreover, two contact models with falling friction characteristics were used: Kalker's FASTSIM [36] and the theory from Vermeulen and Johnson [76]. To extend the model further, Periard included simulations of the vehicle curving behaviour and an evaluation of the radiated sound using the Rayleigh integral. In the sound radiation model, the contribution of each mode to the overall sound was evaluated separately. This is a combination of Schneider's [64] and Fingberg's [21] approach to the evaluation of the radiated sound.

Sound radiation was also addressed in the squeal model by Huang et al. [31]. He implemented the sound radiation model developed by Thompson and Jones [74], which is similar to Fingberg's approach [21]. Huang's model considered both wheel and rail with their mobilities in the lateral, vertical and longitudinal directions. The wheel/rail contact was solved using Kalker's FASTSIM [36]. Several falling friction models were used, which describe the influence of different creepages on the lateral force.

In their model, Heckl and Abrahams [26] used convolution instead of numerical integration to determine the system response. The wheel was represented as a circular disc with the Green's function (impulse response) obtained from the superposition of the disc modes. Only the lateral dynamics was considered and the rail was not included in the model. A point contact on the wheel with a piecewise-linear falling friction characteristic was implemented. The wheel response was then obtained by convolution of the contact force and the Green's function. From their time-domain model, Heckl and Abrahams also developed a frequency-domain model [27] described in Section 3.1.1.

Chiello et al. [14] used a combination of frequency and time-domain models. The stability analysis was carried out using the frequency-domain model and the unstable cases were simulated in the time domain. The wheel was described with its modal parameters, while the rail was considered as rigid. The contact problem was solved with Kalker's linear theory in which a falling friction model was implemented.

The governing equations in Chiello's model have an asymmetric stiffness matrix due to the coupling of the vertical and lateral dynamics. This is, however, only the case in the time-domain model. The frequency-domain model was solely based on the falling friction mechanism. Consequently, the model predicts squeal caused by the falling friction mechanism, but includes the coupling in time-domain computations of squeal cases.

Measurements from [77, 12, 42] correlated well with the theoretical model of Chiello et al. [14]. However, the falling friction characteristic was not observed in measurements. This brought about the question of the friction model formulation. Chiello et al. argued that an instantaneous friction model (valid for high-frequency phenomena) may have a falling characteristic. But measurements are only able to measure the average friction, which was constant. Transient phenomena in the contact area were held responsible for influencing the friction law.

In contrast to Chiello's model, Brunel et al. [12] obtained squeal in cases with a constant and a falling friction model. Brunel developed an axi-symmetric FE model of the wheel with the contact excitation force decomposed using the Fourier

series. The problem was then solved for each harmonic component separately, with harmonic components characterized by the number of nodal diameters in wheel modes. The rail was not considered. Results have shown that squeal occurrence may be insensitive to the exact shape of the friction model.

The work of Glocker et al. [23] focused on squeal being the result of geometric coupling alone. They also argue that squeal is rather insensitive to the exact shape of the friction curve, as properties change along the curve due to wear, surface irregularities and contamination. Moreover, Glocker et al. question whether the common understanding of stick-slip makes sense in the case of small displacements. Namely, the displacements of particles during stick-slip are in the order of the size of asperities, which in their opinion reduces the importance of the friction model. They put the focus on the wheel dynamics.

As Chiello et al. [14], Glocker et al. also used a combination of frequency and time-domain models. The frequency-domain model was used to study the stability of wheels in a bogie, while the time-domain model was used to simulate squeal cases.

The wheel was included with its mass and stiffness matrices obtained from an FE model. The rail was not considered. A point contact was assumed and modelled as a hard unilateral constraint with constant friction (Coulomb model). A suitable time-integration scheme was also developed.

Glocker et al. found that, for squeal to occur, a number of wheel modes has to be present with closely spaced eigen-frequencies. When combined, these modes show a strong coupling between the vertical and tangential degrees of freedom.

The time-domain models presented above consider the rolling contact as steady state or use certain approximations to include transient phenomena (for example Fingberg [21]). In contrast, Pieringer [56] implemented a fully transient contact model by using Kalker's variational contact theory [37], which is a three-dimensional, non-linear and transient rolling contact model.

Pieringer combined the approaches of Heckl and Abrahams [26] and Glocker et al. [23]. The wheel and rail were included with Green's functions for the lateral, vertical and vertical-lateral coupling dynamics. Convolution was used to determine the wheel/rail displacements from the contact forces and Green's functions. The friction coefficient was kept constant (Coulomb model), thus considering the geometric coupling mechanism. The circumvention of numerical integration, implementation of an elaborate contact model and inclusion of the rail dynamics are significant improvements over Glocker's model. However, the computational cost of the detailed contact model was high, resulting in long computation times.

3.2 Models for the rolling contact

Wheel/rail contact models are used to determine contact variables: forces in the vertical (normal[2]), lateral and longitudinal direction, normal pressure and tangential traction[3] distributions, along with the contact area shape and size. Knowledge of the contact forces usually suffices in simulations of vehicle dynamics, evaluation of rolling noise and even curve squeal. However, for certain purposes the normal pressure and tangential traction distributions are important, along with displacements in the contact area. Determination of wear is one example where this detailed information is required. The interest in details of the stick-slip process during squeal is another example.

Contact variables are dependent on a number of parameters: wheel and rail material parameters, kinematic and geometric parameters that determine the wheel/rail relative motion (creepages, see Section 2.1), contact position and the geometry of the contacting surfaces. Additionally, environmental parameters play a crucial role mostly by influencing friction. The mentioned parameters form the input to the contact model.

Material parameters and the material behaviour are important for computation of the displacements in the contact. Wheels and rails are almost always made out of the same material - steel, which is regularly considered as a linear-elastic material in contact models used in squeal modelling. Therefore, all contact models encountered in squeal models assume linear elasticity in the force-displacement relations.

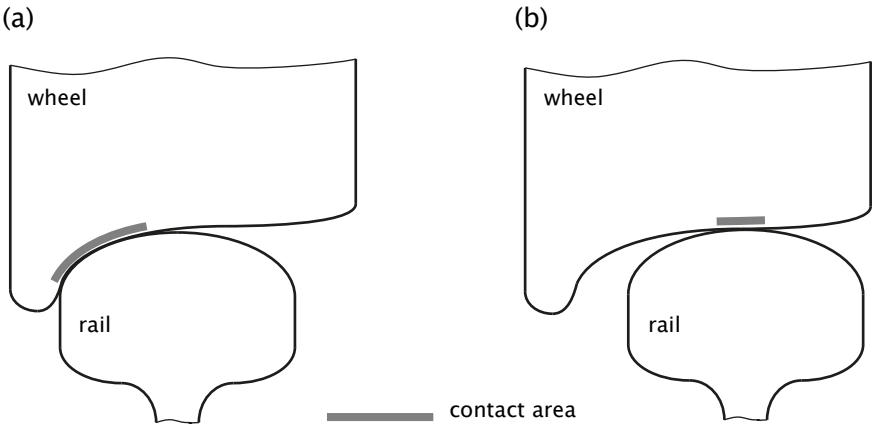

Figure 3.2: Wheel/rail contact: (a) conformal flange contact; (b) non-conformal wheel tread/rail head contact.

The geometry of the contacting surfaces is an important aspect in contact mod-

[2]Vertical forces are also called "normal", by which it is meant forces acting along the direction normal to the wheel and rail surface. Both names, "vertical" and "normal" are used in this work to refer to the same forces (directions).

[3]The surface stress in the normal direction is referred to as "pressure". Despite having the same unit, the surface stress acting along a tangential direction (lying in the contact plane) is referred to as "traction".

elling as it has a significant impact on the distribution of stresses in the contacting bodies. With regards to the surface geometry, conformal and non-conformal contacts are distinguished. Figure 3.2 shows examples of both conformal and non-conformal contacting surfaces. In the context of wheel/rail contact, non-conformal contact occurs in wheel tread/rail head contact (Figure 3.2 (b)). Conformal contact, on the other hand, occurs when wheel flange and rail gauge corner are in contact (Figure 3.2 (a)).

A contact is considered conformal when the dimension of the contact area is in the order of the characteristic dimensions of the bodies in contact [34]. In flange contact, the radii of curvature of the wheel and rail surfaces at the contact point are comparable to the contact size [55]. The stress distribution over the complete body has to be considered in that case.

Approaches to the solution of the conformal contact problem in the general case require numerical methods [34]. Finite-element and boundary-element approaches, like the model of Paul and Hashemi [53], can be used to solve the problem. Still, according to Knothe et al. [41] and Pieringer [55], FE-based solution of the time-dependent problem is not yet available.

Non-conformal contacts are simpler to model compared to conformal contacts. The contact stresses are concentrated close to the contact region, not affecting the stress distribution in the complete body [34]. The contact stresses can be computed with the bodies considered to be semi-infinite, bounded by a plane surface [34]. This corresponds to the so-called elastic half-space, which is one of the few geometries in three-dimensional elasticity for which influence functions are explicitly known [55]. Influence functions describe the deformation of the elastic half-space due to a unit load acting in a point of the half-space.

Finally, the distinction between Hertzian and non-Hertzian contact is made. Hertzian contact comprises contact of surfaces that can be described with second-order polynomials in the vicinity of the contact area [47, 55]. In this case, the function describing the distance between the undeformed surfaces is also a second-order polynomial. This characterizes the so-called Hertzian surfaces. In addition, for a contact to be Hertzian, surfaces must be smooth, without friction, and the material linear elastic and the half-space assumption must hold true [34]. Hertzian contact leads to an elliptical contact area and an ellipsoidal normal-contact pressure distribution.

The definition of the Hertzian contact automatically excludes conformal contact. While conformal contact is non-Hertzian by definition, non-conformal contact can be both Hertzian and non-Hertzian.

Non-Hertzian contact of the wheel and rail is, in the first place, a result of the contacting surfaces, which cannot be described using second-order polynomials. The radii of curvature may change significantly for small lateral displacements on the wheel tread [82]. The change in curvature is even more pronounced for worn wheel and rail profiles [55]. Discontinuities in the radii of curvature may lead to multiple contact patches, besides the non-elliptical contact area.

Surface roughness may also lead to non-Hertzian contact [55, 58]. In reality all

surfaces have a degree of roughness and contact occurs at distinct locations within the contact area. At these locations, asperities of the two surfaces touch, leading to local pressures several times higher than the maximum predicted by the Hertz theory [41]. However, asperities in contact show plastic deformations due to high contact pressures, which in turn lower the contact pressure by increasing the real contact area. Elastic models can be used with acceptable accuracy [32].

The review of models used in squeal modelling given in Section 3.2.3 is limited to models for non-conformal contact. Both Hertzian and non-Hertzian models are considered. This is motivated by observations that curve squeal commonly occurs on the curve inner wheel (see Section 2.1). The contact on the inner wheel is located towards the field side of the wheel, where the wheel tread and rail head are in contact. As can be seen in Figure 3.2 (b), this is clearly a non-conformal contact. However, the possibly changing radii of curvature may result in non-Hertzian contact. In these cases, the elastic half-space assumption is valid and the corresponding solution is widely used.

3.2.1 Contact conditions during squeal

In this section, the processes taking place in the contact area are discussed. These processes should be well understood in order to make an educated choice of contact model for the specific purpose. The focus of this discussion is laid upon processes leading to squeal - the wheel/rail stick-slip motion.

The overall relative motion between wheel and rail is defined by the creepages, Equations (2.1) to (2.3) in Section 2.1. In the finite-sized contact area, this overall relative motion is compensated[4] in two ways. One by the local deformations of the wheel and rail in the contact area [55, 34] due to the wheel and rail elasticity. The other by the relative motion between particles in contact.

Figure 3.3 (a) shows the deformation of the wheel and rail particles in contact. Regions where compensation is achieved only by deformation of the contacting particles (stick region), and regions where compensation is achieved by relative motion and elastic deformation (slip region) are distinguished. A pure longitudinal creepage is assumed in this example.

Figure 3.3 (b) shows the corresponding distribution of the longitudinal traction, which was obtained by Carter [13]. In the stick region, wheel and rail particles do not move relative to each other because the tangential tractions limit defined by the friction coefficient and normal pressure is not reached. From the leading edge of the contact towards the trailing edge, the traction p_1 builds up, leading to the build-up of deformations. However, at one point the longitudinal traction reaches the traction limit. The contacting particles cannot stick any longer and relative motion occurs. The rest of the contact area is in slip.

[4]The rail is fixed on the ground, while the wheel rolls on the rail. The wheel/rail relative motion is then seen as the difference between the wheel-tread tangential velocity and the rolling velocity. The term “compensation” is used because the contact area has to “compensate” for the relative motion of the moving wheel on the static rail.

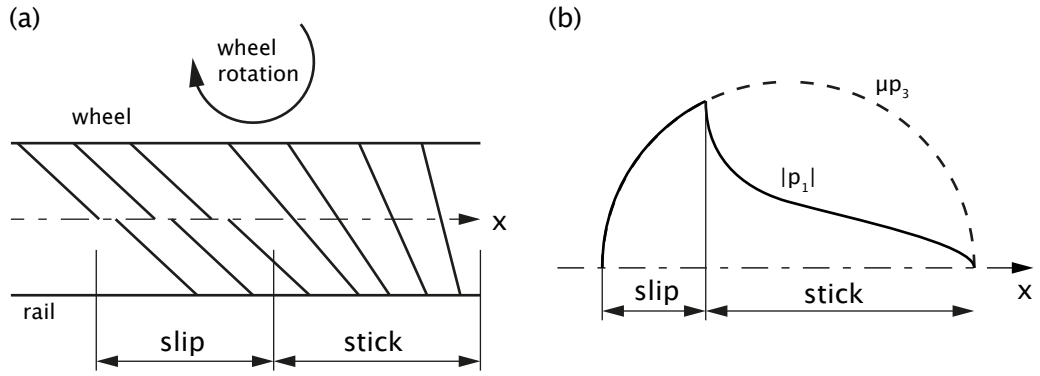

Figure 3.3: Division of the contact area into stick and slip regions: (a) deformations of the contacting particles; (b) tangential tractions distribution according to Carter [13].

Whenever creepage is present between wheel and rail, slip will occur in the contact area. Moreover, the relative motion between wheel and rail gives rise to the tangential-contact forces. In the case of longitudinal creepage, these forces are known as traction or braking forces.

Slip between particles in contact is defined as [37]:

$$s_\tau = w_\tau - v\frac{\partial u_\tau}{\partial x} + \frac{\partial u_\tau}{\partial t}, \qquad \tau = 1, 2, \tag{3.1}$$

where v is the rolling velocity, s_τ the local slip between particles and u_τ the displacement difference between wheel and rail. The term w_τ is the contribution of creepage to the slip velocity. Kalker [37] refers to w_τ as rigid slip. This contribution depends on the creepages and, only when spin creepage is present, on the particle location in the contact area:

$$w_1 = (\gamma_x - \gamma_\omega y)\, v, \qquad\qquad w_2 = (\gamma_y + \gamma_\omega x)\, v. \tag{3.2}$$

The x direction (index 1) corresponds to the longitudinal direction, while the y direction (index 2) denotes the lateral direction.

Equation (3.1) has to be solved in order to determine the distribution of stick and slip regions in the contact. This equation describes the general case of transient rolling. The last two terms denote the material derivative of the particle deformations, which can depend on both space and time. In the steady-state problem, time dependency vanishes: $\partial u_\tau/\partial t = 0$.

As early as 1926, Carter [13] investigated the steady-state tractive rolling of a cylinder. He carried out a two-dimensional analysis of the problem and was the first to solve the tractive rolling contact problem, obtaining the traction distribution shown in Figure 3.3 (b). However, for squeal modelling purposes the steady-state assumption may not be valid.

During squeal, the stick and slip distribution in the contact changes with time, following the stick-slip instability process. The distinction between global and local

(contact-particle level) motion is very important for the correct understanding of the stick-slip process.

On the global level, stick-slip motion comprises the continuous interchange of stick and slip phases between the wheel and rail at the contact point. These phases can be clearly distinguished within a single oscillation period, as shown in Figure 3.4 (a).

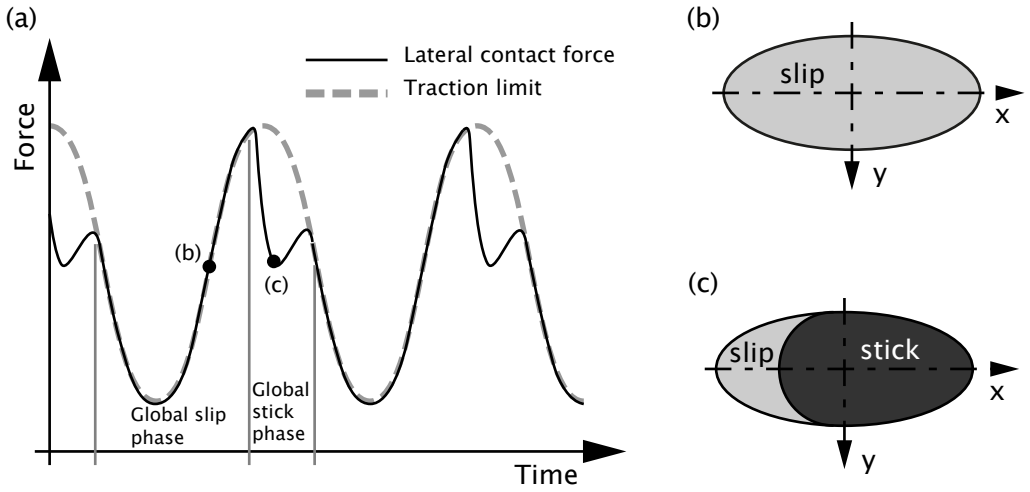

Figure 3.4: Detail of wheel/rail contact-forces time history during squeal showing the characteristics of stick-slip (a). Contact conditions characteristic for the slip phase (b) and for the stick phase (c) are depicted.

On the local level, stick-slip motion results in an interchange of periods with full-contact slip (Figure 3.4 (b)) and periods with stick regions present in the contact area (Figure 3.3 (c)). Processes occurring at local level are the consequence of the global motion.

If considered from the energy aspect, stick-slip instability can be looked upon as an interchange of potential and kinetic energy. During the stick phase the wheel and rail deformations[5] build up, increasing the stored potential energy. The maximum deformation is limited by the tangential-force limit μF_3 in the contact area, which is defined with the normal load F_3 and the friction coefficient μ. Once that limit is reached, gross sliding between wheel and rail occurs. The stored potential energy is then transformed into kinetic energy and deformations are relieved. As deformations and, consequently, force decreases, stick is re-established, and the input energy from creepage is again stored as potential energy (deformation) and the process repeats.

The exact process of stick-slip is influenced by the inertia of the wheel and rail, which defines the amount of kinetic energy that can be stored in the wheel and rail. In consequence, this defines the inertia forces and influences the magnitude and shape of the tangential-force response. Stick-slip can be best noticed in the

[5]The global elastic deformations of the wheel and rail are discussed at this point. Though playing an important role, deformations in the contact are not seen as critical to the interchange of energy. Rather, contact phenomena are considered a consequence of the global wheel/rail motion.

lateral force time-history (Figure 3.4 (a)), which also explains the presence of higher harmonics in squeal. The traction limit, proportional to the normal force and friction coefficient, does not change in shape throughout stick and slip phases. In contrast, the lateral force shows a sharp decline as stick takes place, thus introducing higher harmonics.

The high frequency of curve squeal leads to fast changes in contact conditions, which are expressed via the contact variables defined on the contact particle level. In this case of fast changing conditions, a particle will see a significant change during the time it travels through the contact area. Such conditions are called transient contact conditions, and contact models able to describe such processes, transient contact models.

Figure 3.5 illustrates the above described change of variables along the contact area. Two cases are presented: a low frequency motion and a high frequency motion, each characterized by its characteristic wavelength L, used to describe the variable rate of change. For the low frequency motion case the rate of change is rather low. The change of contact variables along the contact area can then be neglected without introducing a significant error in the results. However, for the high frequency case of Figure 3.5, the variable change is significant. In theory, this should not be neglected [40, 39].

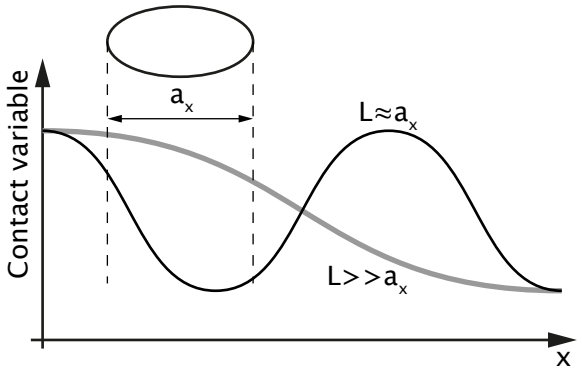

Figure 3.5: Variation of the contact variable along the contact length for case of a low frequency motion ($L \approx a_x$) and a high frequency motion ($L >> a_x$) [40].

Knothe and Groß-Thebing [40, 39] used the ratio L/a_x of the characteristic motion wavelength L and the contact length in the rolling direction a_x to characterize contact conditions. A ratio lower than ten characterizes transient conditions [40]. Although they considered rail corrugation, the same approach can be used to determine conditions during squeal. A case of $f = 2$ kHz squeal with $v = 50$ km/h rolling velocity and $a_x = 12$ mm contact length gives the characteristic motion wavelength of $L = v/f = 0.007$ m and the L/a_x ratio is 0.58. The contact conditions during squeal are, thus, transient.

Whether a transient contact model is required for squeal modelling is still not clear. Guidelines from Knothe and Groß-Thebing [40, 39] indicate a clear need for a transient model. However, in response Kalker [37] compared steady-state and tran-

sient analyses results of a rail corrugation case. The steady-state approach resulted in a slight overestimation of the frictional work compared to the full transient model results. Kalker concluded that the effect of transient contact conditions is not pronounced, questioning conclusions of Knothe and Groß-Thebing [39]. He concludes that transient contact processes can be described as a succession of steady-states.

Baeza et al. [9] investigated the influence of transient processes on contact variables. A harmonically varying force was imposed on the contact and the resulting creepages were observed. In cases with rapid force variations, steady-state models did not give satisfactory results. Differences between steady-state and transient model results were found to depend on the L/a_x ratio. Specific values that would define the validity limit of steady-state models were not given.

3.2.2 Structure of a contact model

In this section, the general structure of a rolling contact model is described. Focus is put on the peculiarities of the wheel/rail contact that influence the formulation of a contact model.

As mentioned at the beginning of the previous section, a contact model relates contact forces, pressure and tractions to the wheel/rail relative motion and imposed load. The model transforms inputs into outputs in a number of steps shown in Figure 3.6. Three main sub-models are distinguished: the normal contact, the tangential contact and the friction model. Inputs and outputs of each sub-model are noted as well.

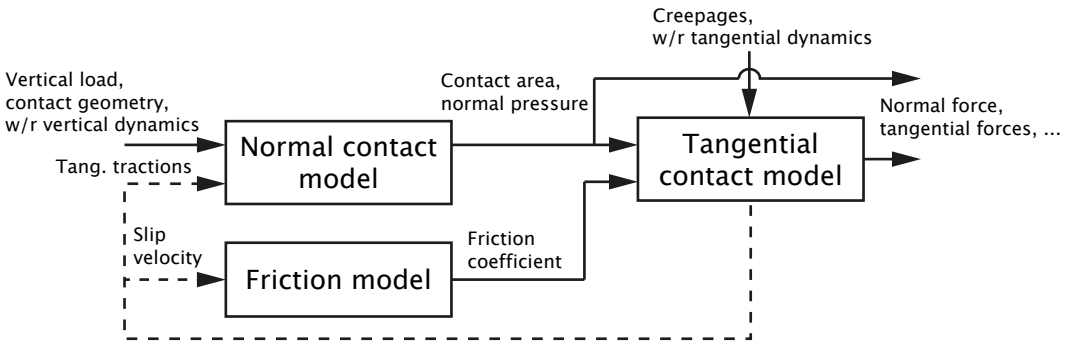

Figure 3.6: Typical structure of a rolling contact model.

The first step of solving the complete contact problem is the determination of the contact area shape and size, along with the normal-contact pressure distribution. For that the vertical load, the wheel and rail contact-surface geometries and (eventually) the wheel/rail vertical dynamics response is required. Also, the material parameters have to be known. The results of the normal problem form the input of the tangential problem.

A feedback from the tangential model to the normal contact model is present in Figure 3.6. In the general case of the elastic half-space, the solution of the normal problem is influenced by the tangential tractions. The reason behind this is

the behaviour of the elastic half-space, where tangential loading causes deformations in both normal and tangential directions. The converse is also true: normal loading causes both normal and tangential deformations [34]. The magnitude of the deformation depends on material parameters and for contacting bodies of different materials deformations will differ. According to Newton's third law, pressure and tractions must be equal and opposite on the solids in contact. The difference in deformations leads to the coupling of the normal and of the tangential contact problem, which have to be solved simultaneously.

In practice, however, the wheel and rail are almost always made out of the same material, steel. Deformations of wheel and rail are then equal in magnitude and opposite in direction, thus removing the feedback loop. This uncouples the normal and tangential problems, which are then solved independently. First, the normal problem is considered, followed by the tangential problem solution. More details and mathematical considerations can be found in Kalker [37] and Johnson [34].

Another feedback loop runs from the tangential model to the friction model, and depends on the friction law formulation. Besides the tangential tractions, results of the tangential problem include the tangential deformations and slip velocities between wheel and rail. A slip-velocity dependent friction model requires slip velocity as the input parameter for which the friction coefficient is determined or defined. The feedback loop is required in this situation.

In the case of Coulomb friction, the friction coefficient is constant and independent of contact variables and system dynamics. This eliminates the need for the feedback loop and simplifies the contact model.

3.2.3 Review of contact models used in squeal modelling

In this section, the contact models commonly used in squeal models are reviewed. In particular, tangential contact models are described in more detail due to their importance for squeal. The review includes, but is not limited to, rolling contact models used in the squeal models of Section 3.1:

- **point contact**, used by: Rudd [63], van Ruiten [75], Heckl et al. [26, 27], Schneider et al. [64], Brunel et al. [12] and Glocker et al. [23];

- **Kalker's linear theory** [35], used by: Fingberg [21], de Beer et al. [19], Xie et al. [81], Hsu et al. [30], Chiello et al. [14] and Monk-Steel et al. [50];

- **Vermeulen and Johnson's model** [76], used by: Periard [54] and Monk-Steel et al. [49];

- **Kalker's variational theory** [37], used by Pieringer [56];

- **Kalker's simplified theory - FASTSIM** [36], used by: Periard [54], Huang et al. [31] and Squicciarini et al. [69].

Point-contact models are simple models, which describe processes on the global contact level. Both the normal and the tangential problem can be considered as point contacts. This modelling approach leads to very fast algorithms, especially when used for the tangential problem. Point-contact models are based on analytical formulas used to represent the creepage/creep force relationship. Sometimes they are even formulated in terms of the friction model.

Hertz's theory of normal contact [28] is suitable for the wheel tread/rail head contact case, which often fulfils the requirements for the Hertzian contact (see Section 3.2). Combined with the simplicity of the model, this makes the model widely used. In its core, Hertz's theory can be considered as a point contact, as all variables are determined from analytical expressions. Details about the Hertz theory of contact can be found in [34, 47], along with a comprehensive description of the model.

A large number of contact models apply Hertz's theory for normal contact. Moreover, in a number of squeal models [31, 19, 81, 30, 69] the normal contact was introduced with the non-linear spring characteristics obtained from the Hertz theory.

The formulation of the tangential point-contact varies between models. A common approach to the one-dimensional problem is based on the relationship between normal and tangential forces:

$$F_\tau = \mu\,(s)\,F_3, \qquad \tau = 1 \text{ or } 2. \tag{3.3}$$

Indices 1 and 2 denote the longitudinal and lateral directions, x and y, while index 3 denotes the vertical z direction. In-contact-plane forces are simply related to the normal force by the friction coefficient. Equation (3.3) is valid only for the one tangential direction, either $\tau = 1$ or $\tau = 2$.

The complexity of the tangential point-contact model depends on whether the friction model is slip-velocity dependent or not, and whether both tangential directions are considered. If both directions are considered, the slip velocity is determined as $s = \sqrt{s_1^2 + s_2^2}$ and the right-hand side of Equation 3.3 has to be multiplied by s_τ/s. A non-linear system of equations then describes the problem. However, if a single tangential direction is taken into account the model is simple, with a single linear equation to be solved.

Despite their simplicity and computational efficiency, point-contact models have a significant downside stemming from the global contact consideration. Processes taking place in the contact area on the contact-particles level cannot be well described. This in particular concerns transient contact processes. As the friction model determines the relation between force and creepage, some information about the contact processes has to be included in the friction model.

More elaborate models include information about local contact processes separately from the friction model. They may, however, still be similar to point-contact models in nature. A typical example is Kalker's linear theory [38].

The linear theory was developed by linearising Carter's solution [13]. Carter's solution is exact for the case of a cylinder rolling on a plane, which is a two-dimensional

problem. Carter's creepage-force relationship is non-linear [38]:

$$\frac{F_1}{\mu F_3} = \begin{cases} -k\gamma_x + \frac{1}{4}k^2\gamma_x|\gamma_x| & \text{if } k|\gamma_x| \leq 2, \\ -\text{sign}\,(\gamma_x) & \text{if } k|\gamma_x| > 2, \end{cases} \tag{3.4}$$

where $k = 4R_W/(\mu a)$ is Carter's creepage coefficient, R_W the cylinder radius and a half of the contact width. This non-linear equation describes the transition from the no-slip (full stick) contact case towards the full slip (gross sliding) case. Figure 3.7 shows Carter's solution, Equation (3.4).

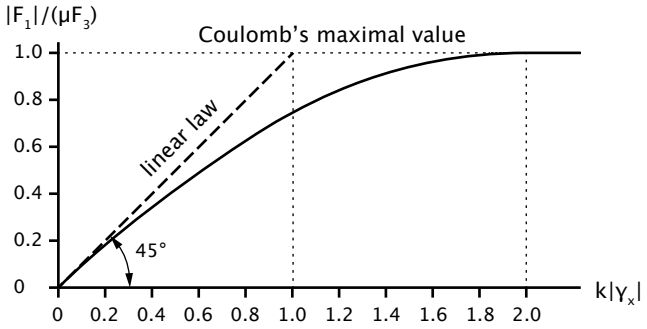

Figure 3.7: Creepage-force relationship according to Carter's theory (solid line) and Kalker's linear theory (dashed line). Adopted from [38].

Kalker's linear theory gives the exact solution of the tangential-contact problem for the limiting case of no slip in the contact area. Moreover, Kalker generalized Carter's theory so that all three creepages are considered, thus making it a three-dimensional contact model. The quadratic term in Equation (3.4) is disregarded for small creepage and the linear relationship between creepage and force is obtained [38]:

$$F_1 = -c^2 G C_{11} \gamma_x, \tag{3.5}$$

$$F_2 = -c^2 G C_{22} \gamma_y - c^3 G C_{23} \gamma_\omega. \tag{3.6}$$

The normal problem is solved using the Hertz theory. The quantity c is determined from the contact ellipse semi-axes a and b as $c = \sqrt{ab}$. Kalker's creepage coefficients C_{11}, C_{22} and C_{23} depend only on the contact-ellipse semi-axes ratio a/b and the Poisson ratio of the material. Creepage coefficients can be found tabulated in [38]. The shear modulus of the material is denoted with G.

The linear theory does not consider any interaction between longitudinal and lateral forces, and the contributions of the two directions can be superposed [34].

Knothe and Groß-Thebing [39, 24] extended the linear theory to transient problems. They calculated frequency-dependent creepage coefficients valid for small harmonic variation of creepages. In [39], Kalker's assumption of vanishing creepages (no-slip condition) was kept. However, in [24] the model was extended to a more general case of contact conditions, where finite creepages are considered. In his squeal

model, Fingberg [21] implemented Kalker's linear theory [38] with the frequency-dependent creepage coefficients from Knothe and Groß-Thebing [39]. As this model is not fully transient, but rather an extension of Kalker's linear theory, it was referred to as semi-transient in Section 3.1.2.

The model by Vermeulen and Johnson [76] is an approximate non-linear model. The model is valid for elliptical contact areas, making it a suitable addition to Hertz's normal contact theory. The stick region was also assumed to be elliptical, which introduced an error in the model [34]. Still, a good correlation between model results and measurements is found [76]. The model is steady-state and unable to account for spin creepage.

To include the effects of spin, Shen, Hedrick and Elkins [65] extended the model of Vermeulen and Johnson. Shen et al. note that with increasing spin creepage the differences between their method, Kalker's FASTSIM and Kalker's variational theory increase. Moreover, Kalker [38] noted that their theory is suitable only for small-spin calculations.

Polach [61] developed a tangential contact model for the case of large creepages. Under these circumstances the contact is dominantly in slip and the resulting tangential force close to the traction limit. Polach applied Kalker's linear theory to determine contact shear stiffness and to approximate the effects of spin. The effects of running on the traction limit were included by different reduction factors. These factors are determined by comparison of measurements and simulation results [61]. However, the model is limited to elliptical contact areas and steady-state contact conditions.

All models above are limited to Hertzian contact. As it was mentioned in the introduction of Section 3.2, non-Hertzian contact is often encountered in wheel/rail interaction. Significant work has been performed on non-Hertzian contact models as well.

Multiple contact patches were addressed in a model by Piotrowski and Chollet [59]. They developed two approximate solutions: one based on multi-Hertzian methods and another based on the virtual penetration method. Other models that use similar approaches to multiple patches include those by Piotrowski and Kik [60] and Ayasse and Chollet [8]. The most accurate solution of such contact problems can be obtained using FE, but at a high computational cost. The mentioned models and approaches are, however, concerned with the normal contact problem.

Theories developed by Kalker prevail in the topic of the tangential problem in non-Hertzian contacts. The most detailed, fully transient and non-linear theory is Kalker's variational contact theory [37], which he calls the "exact" theory. This theory is implemented in Kalker's CONTACT program. Details about the formulation and implementation of Kalker's variational theory can be found in [37, 55].

Kalker's variational method is based on the principle of maximum complementary energy. The model consists of two algorithms: NORM for the normal and TANG for the tangential problem. Both algorithms apply an iterative solution procedure, which Kalker calls active-set algorithm [37]. The potential contact area is discretized into rectangular elements in which pressure and tractions are con-

stant. The NORM algorithm solves the normal contact problem and determines the contact shape and size, along with the normal pressure distribution. The contact deformations are obtained from the elastic half-space assumption. It is because Kalker implemented the exact Boussinesq-Cerruti equations for the elastic half-space influence coefficients, that he calls this theory "exact".

The TANG algorithm solves the kinematic Equation (3.1) for the transient rolling contact for each discretization element in contact. The division of the contact area in stick and slip regions is determined, along with the distribution of tangential tractions. The model can handle both vanishing and large creepages, making it very versatile for many practical problems.

To sum up, Kalker's variational theory, in its general formulation, is applicable to [41, 55]:

- steady-state and transient processes;
- Hertzian and non-Hertzian contacts;
- considerations with any combination of the three creepages;
- contact of bodies made out of different materials;
- cases with varying normal force, creepages and/or contact geometry.

However, Kalker's model is limited by the elastic half-space assumption. Conformal contact cannot, therefore, be solved using this model. In addition, the price is high for this detailed and capable rolling contact model in terms of high computation time [41].

Originally, Kalker developed the model with a constant friction coefficient in mind, but a slip-velocity dependent friction law can be implemented as well. This was done by Croft [17] and Pieringer [55], who implemented the friction model from Kraft [43]. They, however, had issues with multiple solutions of the tangential contact problem and unphysical instabilities. Vollebregt [78] also implemented a falling friction law, but introduced what he calls "friction memory" to reduce the irregularity of results. This topic is still a subject of on-going research

An effort to minimize the computational cost while retaining accuracy was made by Kalker and resulted in the simplified theory [36, 38]. This theory is better known under the name FASTSIM, which is how Kalker named the corresponding solution algorithm. While the model includes both normal and tangential contact, the normal contact solution is not reliable [80]. Kalker [38] states that the best results are achieved in the case of Hertzian contact.

In contrast to the variational theory, the elastic half-space was abandoned in favour of a bedding of independent springs[6]. The deformation of one point in the contact area, according to the simplified theory, is proportional to the traction at that same point only. Kalker determined the flexibility of the springs in the bedding on the base of his linear theory.

[6]This is also known as the Winkler bedding.

The contact area is discretized, and the implementation of independent springs results in a simple solution algorithm. Tangential tractions are evaluated within strips of elements along the rolling direction. A gradual build-up of deformations and tractions is obtained within a strip. According to Kalker [37], this approach is about 400 times faster than the CONTACT program. The simplified theory is considered to have the best precision-to-computational cost ratio [5], but it is, however, a steady-state model.

Significant research is concentrated on improving the simplified theory to include transient effects and falling friction laws. Inclusion of falling friction is rather common in curve squeal modelling. For example, Periard [54], Xie et al. [81], Huang et al. [31] and Squicciarini et al. [69] implemented a falling friction law in FASTSIM for squeal modelling purposes. Xie et al. applied it for simulations of the vehicle curving behaviour to determine input creepages for the squeal model. Vollebregt and Schuttelaars [79] and Giménez et al. [22] also performed work on including the slip-velocity dependent friction law into FASTSIM.

Significant work in extending Kalker's simplified theory to transient processes has been made by Shen and Li [66], Alonso and Giménez [5] and Guiral et al. [25]. Shen and Li [66] considered the case of moderate creepage and small spin in the transient case. They included transient effects by including the transient term $\partial u_\tau/\partial t$ in the kinematic equation of the simplified model. Good correlation with the variational theory results was found, except for the case with significant spin.

To better describe transient effects, Alonso and Giménez [5] introduced an additional term next to Kalker's flexibility coefficient. While Shen and Li [66] used Kalker's flexibility coefficient for both steady-state and transient terms, Alonso and Giménez introduced the dynamic flexibility coefficient. This additional coefficient relates only to the transient term, while Kalker's flexibility coefficient were retained next to stationary term. The contact area was assumed to be elliptical and only one creepage was considered to vary in time. They pointed out that the model can be easily extended to include non-Hertzian contacts [5, 4]. In [25], Guiral et al. extended the model by Alonso and Giménez [5] to address the more general case. An arbitrary combination of creepages was included, along with the variation of the normal contact force. Good agreement with Kalker's variational theory results was found in the case of large harmonic variation of creepages.

The more elaborate and transient contact models are seldom used in squeal modelling. Uncertainties whether a transient contact model is needed are part of the explanation (see Section 3.2.1). Also, the contact model behaviour depends upon the formulation of the contact model. For example, Zenzerovic et al. [83] have shown that the use of FASTSIM within Pieringer's squeal model [56] leads to unphysical instabilities. In contrast, Huang et al. [31], Periard [54] and Squicciarini et al. [69] successfully used FASTSIM in their squeal models.

Chapter 4

Formulation of the engineering model for curve squeal

Requirements for the engineering squeal model are specified based on the literature review presented in Chapter 3. The formulation of the contact model is based on the discussion of rolling contact models in Section 3.2.

The model is formulated in the time domain, as the ability to predict squeal amplitudes is considered central to the engineering model. The engineering model for squeal is, therefore, based upon the detailed squeal model developed by Pieringer [55, 56]. To make Pieringer's model more efficient and thus suitable for engineering use, an efficient tangential contact model is formulated and implemented in the interaction model. Moreover, the model was also extended with a simple model for sound radiation from the railway wheel from the literature. The structure of the proposed engineering model for squeal is shown in Figure 4.1.

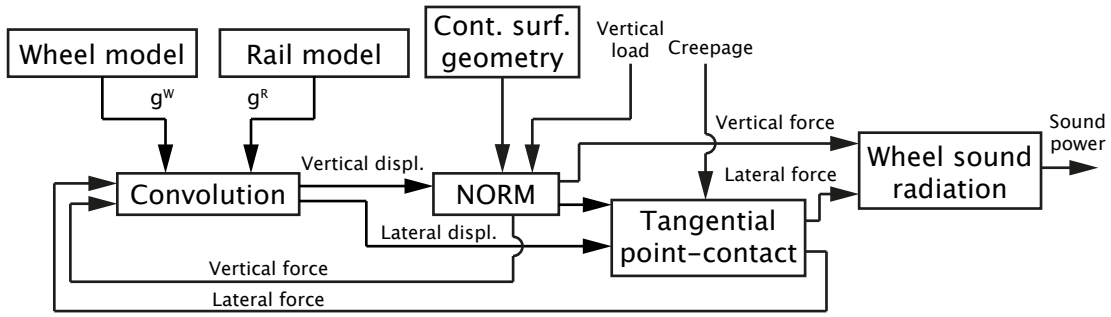

Figure 4.1: Structure of the time-domain engineering model for curve squeal.

The premise of an engineering model is that it is versatile, fast and reasonably accurate. The versatility of a model for curve squeal means that different wheel and rail combinations can be investigated without the need to change the mathematical formulation. In an engineering model this is ever more important and allows for

a streamlined use of the model. The representation of wheel and rail dynamics by Green's functions makes the model versatile. Green's functions (g^W and g^R in Figure 4.1) can be predetermined before running squeal simulations as they depend only on the wheel and rail geometry, material data and wheel suspension. Because Green's functions are used, only linear wheel and rail models, presented in Section 4.2, can be considered. Adding to the model versatility, real geometries of contacting surfaces can be easily included. Even the surface roughness can be easily included, as was done by Pieringer [58].

Computation time is important in engineering practice where tight deadlines are often encountered. The engineering model should therefore require relatively short computation times. The use of Green's functions and convolution, described in Section 4.2, gives a significant advantage in computation time over numerical integration techniques. This approach was used by Pieringer [56] and Heckl and Abrahams [26]. Further improvements in computation times of Pieringer's model [56] can be achieved by means of an efficient contact model. To retain the option of evaluating non-Hertzian contact, Kalker's NORM [37] was kept as the solver for the normal contact problem. However, as the tangential contact model is the most computationally expensive part of the model, a tangential point-contact model was formulated.

In the global contact consideration used in the point-contact model, the friction model was determined using Kalker's variational theory. On the local contact level used in Kalker's model, friction is described by Coulomb's model. In contrast to Kalker's model, the global consideration of the contact in the point-contact model leads to a steady-state model. The contact model is presented in Section 4.3.

Ideally, an engineering model for curve squeal should address the complete source-to-receiver chain. To cover at least part of the excitation force-to-receiver chain, a simple model for sound radiation from the railway wheel was implemented. The model computes the radiated sound power and was originally developed by Thompson and Jones [74]. An outline of the model is given in Section 4.4.

The squeal model was developed with the assumption that creepages and the wheel/rail contact position do not change during the time the vehicle negotiates a curve. In addition, the creepages and contact position are assumed to be known in advance, either precomputed using a vehicle dynamics software or assumed. An additional assumption in the model is that spin creepage can be neglected. The tangential point-contact model is therefore formulated without considerations of the spin creepage.

Before moving on to the model formulation, the coordinate systems used in this work are described in the following section.

4.1 Coordinate systems

Two Cartesian coordinate systems and one cylindrical coordinate system, shown in Figure 4.2, are used. The wheel model is defined in the cylindrical $\left(y^W, z^W, \varphi^W\right)$ coordinate system, while the rail model is defined in the Cartesian $\left(x^R, y^R, z^R\right)$ system. The $(1, 2, 3)$ system is the contact coordinate system[1], in which the contact problem is solved.

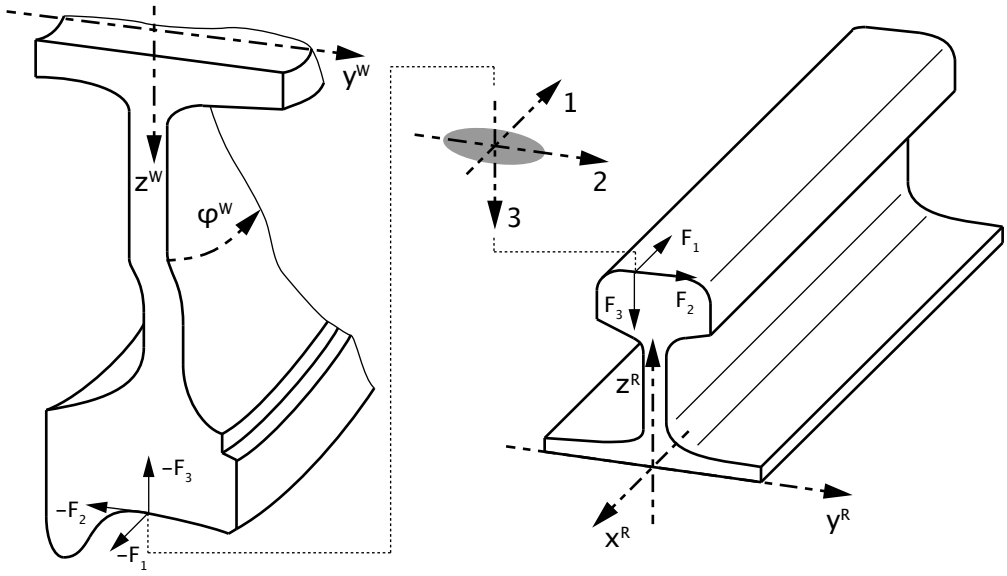

Figure 4.2: Coordinate systems and wheel/rail contact-forces definition.

The wheel and rail coordinate systems are fixed to the wheel and rail respectively. The rail x^R-axis is oriented opposite to the rolling (longitudinal) direction, the y^W- and y^R-axes are oriented towards the field side of the track, and z^W- and z^R-axes are vertical axes, pointing from the ground up. The wheel azimuth angle is φ^W, which describes the wheel circumferential direction. These coordinate systems are, however, only important when considering the wheel and rail models.

The contact variables and forces are defined in the contact coordinate system. Its position is defined by the point at which the wheel and rail make first contact for a given lateral displacement of the wheelset (see Section 4.1.1). The longitudinal axis 1 lies in the contact plane and is positive in the direction of travel. Axis 2 lies in the contact plane as well, perpendicular to axis 1 and positive towards the field side of the wheel and rail. Finally, axis 3 is the vertical axis, perpendicular both to 1 and 2, positive towards the ground. This coordinate system travels with the contact point along the rail with rolling velocity v. Its absolute position along the rail at a time t is $x^R_{ccs} = vt$.

The contact forces F_1, F_2 and F_3 are defined in the contact coordinate system $(1, 2, 3)$. As defined, the contact forces are acting positive on the rail, while the

[1]This coordinate system is often referred to as the (x, y, z) system.

forces on the wheel are reactive forces and are therefore oriented in the opposite direction. Figure 4.2 shows the directions of contact forces acting on the wheel and on the rail.

4.1.1 Wheel/rail nominal contact positions

Three distinct nominal contact points are used in the present work. The contact points were obtained from measured wheel and rail profiles in [56], and are defined with the lateral displacement (offset) Δy^{WR} of the wheelset on the rail. To each wheelset lateral displacement corresponds a lateral coordinate on the wheel tread y^W and a lateral coordinate on the rail head y^R:

$$\Delta y^{WR} = \begin{cases} -5 \text{ mm}, & \text{where } y^W = 5 \text{ mm}, \, y^R = -16 \text{ mm}, \\ -10 \text{ mm}, & \text{where } y^W = -4 \text{ mm}, \, y^R = -12 \text{ mm}, \\ -15 \text{ mm}, & \text{where } y^W = -32 \text{ mm}, \, y^R = 12 \text{ mm}. \end{cases} \tag{4.1}$$

Wheel tread and rail head points coming into contact are represented with the same markers in Figure 4.3 (b) for the wheel, and in Figure 4.5 (b) for the rail. For each contact position, the actual wheel and rail surface profiles around the nominal-contact point are considered.

4.2 System dynamics

As mentioned, the wheel and rail dynamics are included in the model by means of Green's functions. Green's functions are commonly used in mathematics for solving inhomogeneous differential equations subject to specific initial or boundary conditions. The inhomogeneity is considered concentrated in a point, meaning that it can be described by the Dirac delta (δ) function. The response of the system described with the differential equation and excited by the δ function is the Green's function for the problem [16]. Because the Dirac δ function describes a unit impulse, Green's functions are often called impulse response functions.

In the case of mechanical systems, the Green's function $g(x, y, t)$ is seen as the time response of the system at point x due to the unit point forcing at y and $t = 0$ [16, 10]. The Green's functions of the wheel and rail are, therefore, easily obtained from the respective receptances defined in the frequency domain. Receptance is defined as the ratio between displacement and force. For the case when the excitation acts in the same point in which the displacement response is evaluated, the receptance is called point receptance:

$$G_{ij}(f) = \frac{\xi_i(f)}{F_j(f)}, \qquad i, j = 1, 2, 3. \tag{4.2}$$

The term $\xi_i(f)$ is the displacement response in the coordinate direction i due to the excitation force $F_j(f)$ acting in the direction j.

The method used for obtaining the Green's functions (time domain) from the receptances (frequency domain) was proposed by Kropp [44] and is described in [7]. The method is widely used within the Vibroacoustics Group of the Division of Applied Acoustics, Chalmers University of Technology. The advantages of the method, which is described below, are that the obtained Green's function is causal and that Gibbs' phenomenon is avoided.

The assumption behind the method is that the system is sufficiently damped so that the system response decays to zero after a finite period of time. The method consists of constructing the frequency spectrum by taking the real part of the receptances and doubling it:

$$S_{G,ij}\left(f_d\right) = 2\mathfrak{Re}\left\{G_{ij}\left(f_d\right)\right\}, \qquad i,j = 1,2,3, \tag{4.3}$$

where f_d is the discrete frequency. The inverse Fourier transform is then applied to obtain $s_{G,ij}\left(n\Delta t\right)$:

$$s_{G,ij}\left(n\Delta t\right) = \mathcal{F}^{-1}\left\{S_{G,ij}\left(f_d\right)\right\}, \qquad i,j = 1,2,3, \tag{4.4}$$

which gives a time signal with the period $n = 0,\ldots,(N_t - 1)$, where N_t is the number of samples. The discrete time-step length is Δt. The time-domain signal $s_{G,ij}\left(n\Delta t\right)$ contains the Green's function $g_{ij}\left(n\Delta t\right)$, which is obtained as:

$$g_{ij}\left(n\Delta t\right) = \begin{cases} 0.5\Delta t s_{G,ij}\left(n\Delta t\right) & \text{for } n = 0, \\ \Delta t s_{G,ij}\left(n\Delta t\right) & \text{for } n = 1,\ldots N_t/2. \end{cases} \tag{4.5}$$

At $\left(N_t/2\right)\Delta t$, the Green's function is assumed to have decayed to zero.

Green's functions can be used to determine the system response to arbitrary excitation. The solution of an inhomogeneous differential equation is the superposition of elementary solutions (Green's functions) weighted by the excitation function [16]. This can be seen as a discretization of the excitation function into impulses. Green's functions for each discrete impulse are then superposed and the final system response follows. This approach is known as convolution. However, this approach has a limitation: for the superposition principle to be valid the dynamic system must be linear.

Mathematically, the displacement response at time t is defined by the convolution integral of the excitation F and Green's function g:

$$\xi\left(t\right) = F \otimes g = \int_0^t F\left(\tau\right) g\left(t - \tau\right) \mathrm{d}\tau. \tag{4.6}$$

In the case of discrete Green's functions and excitation forces acting in multiple directions, the convolution of Equation (4.6) takes the form:

$$\xi_i\left(t_d\right) = \mathbf{F} \otimes \mathbf{g_i} = \sum_{\tau=0}^{t_d} \sum_{j=1}^{3} F_j\left(\tau\right) g_{ij}\left(t_d - \tau\right), \qquad i = 1,2,3, \tag{4.7}$$

where t_d is the current discrete time-point. As will be discussed later, under certain circumstances the first value of the Green's functions $g_{ij}(0)$, corresponding to $\tau = t_d$, can be neglected. It is therefore convenient to separate the convolution defined in Equation (4.7) into two parts:

$$\xi_i(t_d) = \sum_{j=1}^{3} F_j(t_d)\, g_{ij}(0) + \sum_{\tau=0}^{t_d-\Delta t} \sum_{j=1}^{3} F_j(\tau)\, g_{ij}(t_d - \tau), \qquad i = 1,2,3, \tag{4.8}$$

where $F_j(\tau)$ is the force time-history.

The first part of the convolution given in Equation (4.8) defines the response $\xi_i(t_d)$ due to the force acting at the same time t_d. This term is presents difficulties as the current time-step force $F_j(t_d)$ is not always known and can depend on the system response. The first value of Green's function gives the local instantaneous deformation of the body due to a contemporaneous unit-excitation force. This value can be treated as a dynamic flexibility coefficient, which takes into account the dynamic effects of the system [7].

The second, double sum in the convolution of Equation (4.8) depends only on forces acting in previous instants of time. However, this term is not a convolution any more. By introducing $t'_d = t_d - \Delta t$ in Equation (4.8) the second term again takes the convolution form:

$$\xi_i(t_d) = \sum_{j=1}^{3} F_j(t_d)\, g_{ij}(0) + \sum_{\tau=0}^{t'_d} \sum_{j=1}^{3} F_j(\tau)\, g_{ij}(t'_d - \tau + \Delta t), \qquad i = 1,2,3. \tag{4.9}$$

In the following sections a description of the wheel and rail models is given. The wheel and rail models are taken from Pieringer [55, 56].

4.2.1 Wheel dynamics

The wheel used in the squeal model is a C20-type wheel with a nominal rolling diameter of 780 mm. This wheel type can be, for example, found on vehicles in the Stockholm metro system.

The wheel was modelled using finite elements. The axial symmetry of the wheel enabled the use of axi-symmetric elements, by means of which only the wheel cross section had to be modelled [55]. Figure 4.3 (a) shows the FE mesh of the wheel cross section. Additionally, the primary suspension of the wheelset is included in the model, which can be also considered as a half-wheelset model.

Along the wheel circumference a harmonic solution is assumed, which leads to a complete three-dimensional wheel model. The harmonic variation along the circumference is described with $\hat{a}\cos(n\varphi)$ and $\hat{a}\sin(n\varphi)$ terms. The amplitude $\hat{a}$ is given at a specific position on the wheel cross section. Which harmonic term describes the axial[2], radial and circumferential direction deformations depends on the excitation

[2]When considering the wheel out of the context of the wheel/rail interaction, the longitudinal, lateral and vertical directions can be referred to as circumferential, axial and radial respectively. This nomenclature stems from the directions of the cylindrical coordinate-system axes, which is a suitable system for describing axi-symmetric bodies.

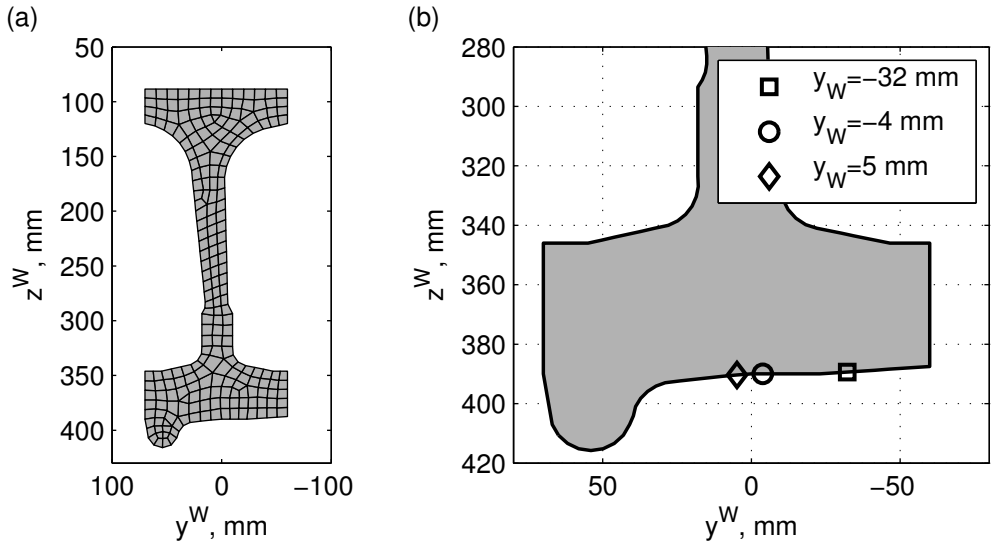

Figure 4.3: C20 wheel cross section: (a) FE mesh; (b) detail of the wheel tread with the three contact points for which receptances are evaluated.

force direction. In case of radial or axial excitation force, the radial and axial deformations are described with cosine terms, while the circumferential deformation is given with the sine term. On the other hand, when a circumferential excitation is applied, the radial and axial deformations are described with the sine term and the circumferential with the cosine term.

Using commercial FE analysis software, the wheel eigen-frequencies and eigen-modes were determined in [55] for frequencies up to 7 kHz. The wheel eigen-modes with their corresponding eigen-frequencies are listed in Table 4.1. Wheel modes are denoted as (n, m, Class), where n is the number of nodal diameters and m is the number of nodal circles. The term *Class* refers to the dominant motion of the wheel: axial (a), radial (r) and circumferential (c). More information about the classification of wheel modes and the wheel vibration characteristics can be found in [72, 71, 55].

The wheel receptances $G_{ij}^W(\Omega)$ are determined from the wheel mode shapes Φ_r, eigen-frequencies ω_r ($\omega_r = 2\pi f_r$) and modal damping factors ζ_r by modal superposition [72, 55]:

$$G_{ij}^W(\Omega) = \sum_r \frac{\Phi_{ri}\Phi_{rj}}{m_r\left(\omega_r^2 - \Omega^2 + \mathrm{i}2\zeta_r\omega_r\Omega\right)}. \tag{4.10}$$

The receptance G_{ij}^W gives the response in the degree of freedom i due to the excitation acting in the degree of freedom j. The term m_r is the modal mass of mode r and Ω ($\Omega = 2\pi f$) is the angular frequency of the harmonic-excitation force.

The wheel modal-damping factors are a common source of uncertainty in wheel models. The reason behind the uncertainty is that damping factors cannot be measured precisely and their determination usually involves some kind of approximation. A good starting point for the wheel modal-damping factors, used in [55] and pro-

$\mathbf{f_r}$, Hz	$(\mathbf{n}, \mathbf{m}, \mathbf{Class})$
243.2	$(1, 0, a)$
332.8	$(0, 0, a)$
429.9	$(2, 0, a)$
721.9	$(0, 0, c)$
1143.2	$(3, 0, a)$
1586.4	$(1, 0, r)$
1923.9	$(0, 1, a)$
2058.3	$(4, 0, a)$
2089.4	$(1, 1, a)$
2242.5	$(2, 0, r)$
2584.8	$(2, 1, a)$
2834.1	$(3, 0, r)$
3070.8	$(5, 0, a)$
3193	$(3, 1, a)$
3535.8	$(4, 0, r)$
3625.1	$(0, 0, r)$
3880.8	$(4, 1, a)$

$\mathbf{f_r}$, Hz	$(\mathbf{n}, \mathbf{m}, \mathbf{Class})$
3886.2	$(1, 0, c)$
4131.1	$(6, 0, a)$
4176.8	$(0, 2, a)$
4236.6	$(1, 2, a)$
4349.6	$(5, 0, r)$
4417.2	$(2, 2, a)$
4635.2	$(5, 1, a)$
4871.7	$(3, 2, a)$
5215.9	$(7, 0, a)$
5227.5	$(2, 0, c)$
5267.8	$(6, 0, r)$
5454.1	$(6, 1, a)$
5546.6	$(4, 2, a)$
6268.7	$(7, 0, r)$
6315.6	$(8, 0, a)$
6343	$(7, 1, a)$
6405.5	$(5, 2, a)$

Table 4.1: C20 metro wheel eigen-modes classification and corresponding eigen-frequencies of modes below 7 kHz.

posed by Thompson [72] is:

$$\zeta_r = \begin{cases} 10^{-3} & \text{for modes with } n = 0, \\ 10^{-2} & \text{for modes with } n = 1, \\ 10^{-4} & \text{for modes with } n \geq 2. \end{cases} \tag{4.11}$$

These damping factors were determined for a free wheel without the axle. Additionally, Thompson [72] has shown that the axle introduces significant damping in the radial mode with one nodal diameter and zero nodal circles. The $(1, 0, r)$ mode damping factor is therefore set to one.

Figure 4.4 shows the vertical and lateral point receptances and the vertical-lateral cross receptance for the three wheel-tread contact points marked on Figure 4.3 (b). The vertical-lateral cross coupling is a result of the asymmetry of the wheel cross section. As can be seen from Figure 4.4 (c), the strength of the coupling depends on the position on the wheel tread. Differences between receptances at different points on the wheel tread are largest in the vertical-lateral cross receptance. The vertical point receptance of Figure 4.4 (a) hardly shows any differences between wheel-tread points. Some differences can be noticed in the lateral point receptance of Figure 4.4 (b), but they are not as pronounced as in the cross receptance. The position of the contact point on the wheel tread is therefore very important for the occurrence and amplitudes of squeal. This is especially true for curve squeal caused by the geometric coupling mechanism.

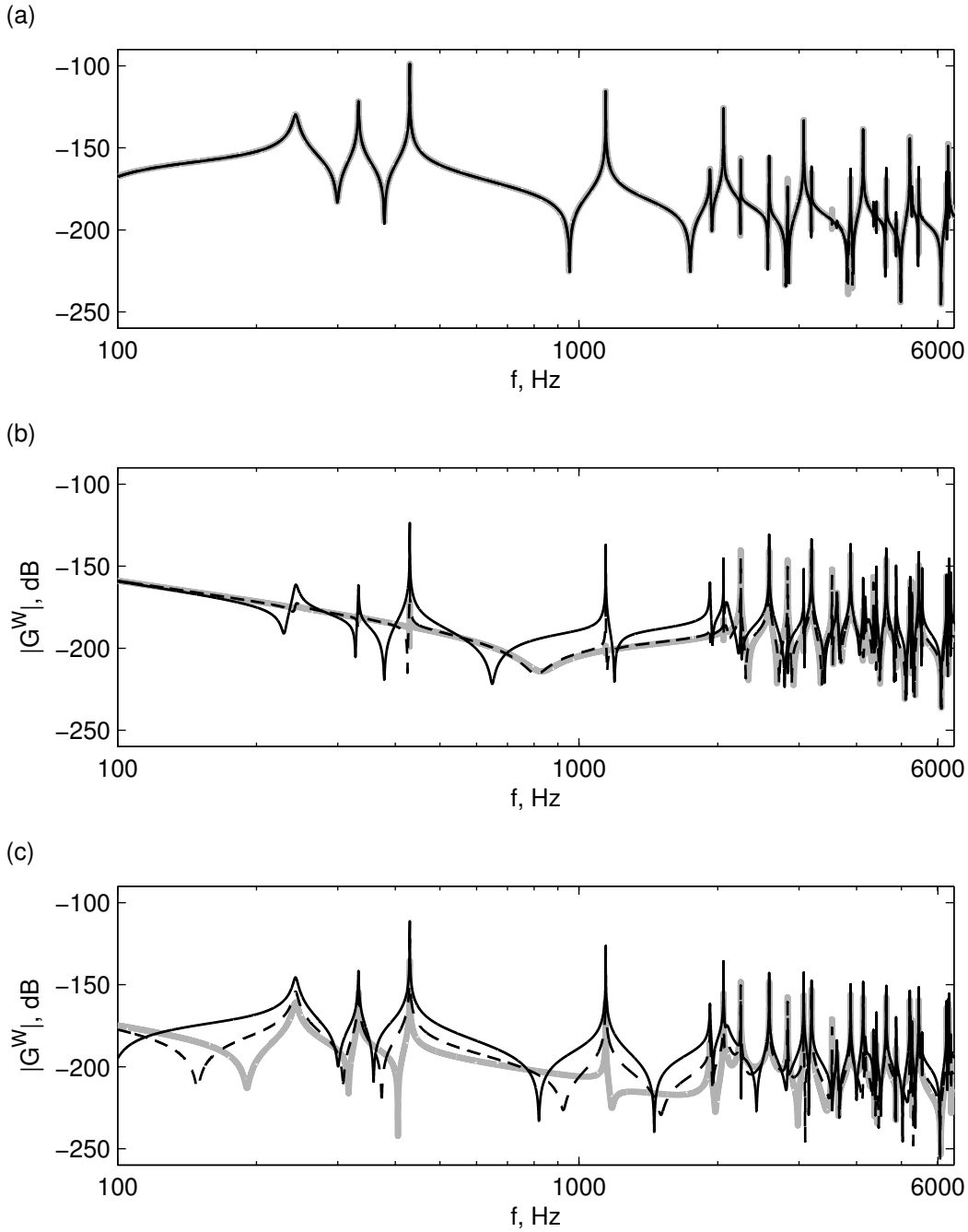

Figure 4.4: Receptances of the C20 wheel: (a) vertical receptance, (b) lateral point receptance and (c) vertical-lateral cross receptance. Receptances are evaluated for the three contact points on the wheel tread marked in Figure 4.3 and defined in Section 4.1.1: (— black) $y^W = -32$ mm; (- - black) $y^W = -4$ mm; (— grey) $y^W = 5$ mm. Magnitudes are given in levels (dB rel. 1 m/N) for the frequency range of 100 Hz to 6.5 kHz.

The effects of wheel rotation are neglected. A study performed by Pieringer [57] has shown that the effects of wheel rotation on eigen-frequencies and, consequently, receptances, do not significantly influence the results of the squeal model. This is at least true for the contact forces, as the influence of wheel rotation on the radiated sound was not evaluated.

As described in Section 4.2, the wheel Green's functions g_{ij}^W are obtained from the receptances G_{ij}^W by means of an inverse Fourier transform, Equation (4.4). The wheel displacement response is then obtained from the discrete convolution, analogous to Equation (4.9):

$$\xi_i^W(t_d) = -\sum_{j=1}^{3} F_j(t_d)\, g_{ij}^W(0) - \sum_{\tau=0}^{t'_d} \sum_{j=1}^{3} F_j(\tau)\, g_{ij}^W(t'_d - \tau + \Delta t), \qquad i = 1, 2, 3. \tag{4.12}$$

The negative signs in Equation (4.12) come from the direction of the contact forces acting on the wheel, but are defined in the contact coordinate system (see Figure 4.2 in Section 4.1).

In the squeal model by Pieringer [55], two simplifications have been made. The first is that only the lateral and vertical dynamics of the wheel and rail are considered. The second is the omission of the first values in the wheel and rail Green's functions.

Longitudinal dynamics are not considered to play an important part in the squeal process. Rudd [63] and Remington [62] recognized early that longitudinal creepage is not a cause of curve squeal (see Section 2.1). It is therefore expected that the longitudinal dynamics should not influence curve squeal.

As discussed in Section 4.2, the first value of Green's functions describes the local instantaneous deformation. In order for this value to be realistic, the wheel and rail models have to be very detailed around the contact point. However, the wheel FE model is not detailed enough to provide accurate values of the Green's functions' first term $g_{ij}^W(0)$ [55]. The first value of the wheel Green's functions are therefore set to zero ($g_{ij}^W(0) = 0$). Instead, the local instantaneous deformation is, at least partly, accounted for in the contact model. Equation (4.12) simplifies to:

$$\xi_i^W(t_d) = -\sum_{\tau=0}^{t'_d} \sum_{j=1}^{3} F_j(\tau)\, g_{ij}^W(t'_d - \tau + \Delta t), \qquad i = 2, 3. \tag{4.13}$$

The displacement response of the wheel given by Equation (4.13) is dependent only on previous time-step forces. This leads to a simpler equation system where the current time-step displacement response does not depend on current time-step variables [55].

4.2.2 Rail dynamics

The rail used in the squeal model is a BV50-type rail, a common Swedish rail type. The rail was modelled as continuously supported, with the rail pad included in the model [55].

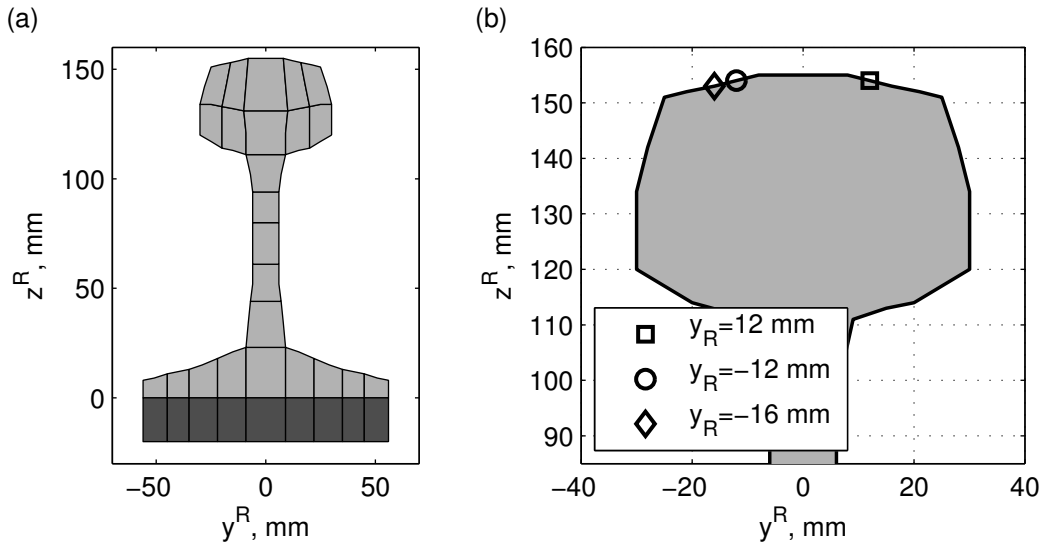

Figure 4.5: BV50 rail cross section: (a) FE mesh; (b) detail of the rail head with the three contact points for which receptances are evaluated.

The two-dimensional cross section of the rail with the rail pad was modelled using finite elements. The FE mesh is shown in Figure 4.5 (a). To extend the model in the third dimension, an analytical wave-type solution is assumed in the rail longitudinal direction. This takes advantage of the constant two-dimensional rail cross-section. The resulting model is referred to as waveguide finite element (WFE) model [51].

The rail receptances were obtained by Pieringer [55, 56] using the software package WANDS [51]. Figure 4.6 shows the vertical and lateral point receptances and the vertical-lateral cross receptance for the three rail-head contact points marked in Figure 4.5 (b).

The rail has considerably less resonance peaks in the frequency region of interest (25 Hz to 6.5 kHz) compared to the wheel. In addition, the rail vertical-lateral coupling dynamics is not so strongly influenced by the lateral contact position on the rail head. This is seen from Figure 4.6 (c) that shows the rail vertical-lateral cross receptance. Consequently, the rail may be of lesser importance for curve squeal.

In analogy to the wheel model, the rail Green's functions g_{ij}^R are obtained from the rail receptances G_{ij}^R by means of the inverse Fourier transform, Equation (4.4). However, a crucial difference is present between wheel and rail Green's functions. Because the wheel rotation is neglected and the lateral contact position is assumed constant in time, the wheel-excitation force is fixed to one wheel-tread point. In contrast, the rail-excitation force travels along the rail with the rolling velocity v,

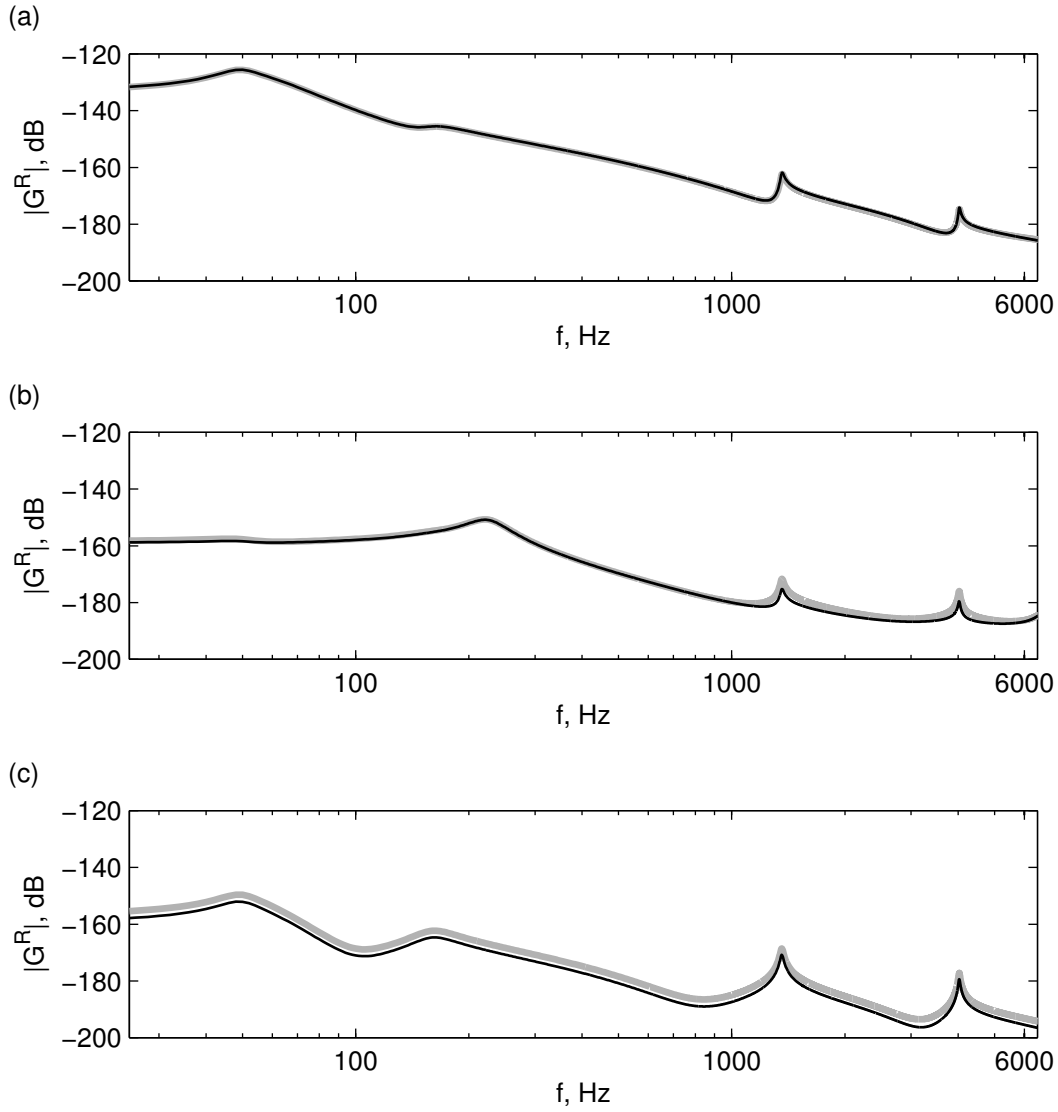

Figure 4.6: Receptances of the BV50 rail: (a) vertical receptance, (b) lateral point receptance and (c) vertical-lateral cross receptance. Receptances are evaluated for the three points on the rail head marked in Figure 4.5 and defined in Section 4.1.1: (— black) $y^R = \pm 12$ mm; (— gray) $y^R = -16$ mm. Magnitudes are given in levels (dB rel. 1 m/N) for the frequency range of 25 Hz to 6.5 kHz.

which cannot be neglected. A special kind of Green's functions, called moving Green's functions [52], are therefore defined for the rail.

Moving Green's functions describe the displacement response at a point moving along the rail, away from the excitation, with the rolling velocity v. The moving contact point case can be looked upon as a case where the observer moves along the rail. Both time and spatial information have to be included in the moving Green's functions to properly describe the rail response. The spatial information, which

describes the previous time-steps contact locations, does not appear explicitly in the functions. Instead, this information is included during the construction of the functions. Details about the construction of moving Green's functions can be found in [55].

With the same analogy to the determination of the wheel response, the convolution for the rail displacement response is given with

$$\xi_i^R(t_d) = \sum_{j=1}^{3} F_j(t_d)\, g_{ij}^{R,x_0^R+vt_d}(0) + \sum_{\tau=0}^{t'_d}\sum_{j=1}^{3} F_j(\tau)\, g_{ij}^{R,x_0^R+v\tau}(t'_d-\tau+\Delta t), \quad i=1,2,3. \tag{4.14}$$

The contact forces defined in the contact coordinate system are active forces on the rail and have a positive sign in Equation (4.14). As discussed in Section 4.2.1, only the vertical and lateral displacement responses are considered and the first value of the rail Green's function $g_{ij}^{R,x_0^R+vt_d}(0)$ is omitted. Equation (4.14) simplifies to:

$$\xi_i^R(t_d) = \sum_{\tau=0}^{t'_d}\sum_{j=1}^{3} F_j(\tau)\, g_{ij}^{R,x_0^R+v\tau}(t'_d-\tau+\Delta t), \qquad i=2,3. \tag{4.15}$$

4.3 The rolling contact model

The general structure of a rolling contact model was discussed in Section 3.2.2. Moreover, in Figure 4.1 where the structure of the engineering model for curve squeal is shown, the sub-models of the rolling contact model were introduced . In this section, the normal and the tangential contact models are described in more detail. Additionally, a method for the determination of the friction model is proposed in Section 4.3.4.

4.3.1 The normal contact model

The consideration of the normal contact problem starts with the definition of the contact kinematics. Figure 4.7 shows the contact kinematics in the normal direction for the case of two non-conformal surfaces. Not shown in the figure, the y-axis is pointing towards the reader. For clarity, the contacting surfaces are denoted with indices W and R indicating the wheel and the rail.

The term $\xi_3 = \xi_3^R - \xi_3^W$ is the displacement-response difference between the wheel and the rail. The vertical displacement responses are given by Equation (4.13) and (4.15) for the wheel and rail, respectively. It should be noted that the vertical displacement response ξ_3 is assumed to be constant over the contact area and is evaluated at the point of initial contact.

The undeformed wheel and rail profiles, $z^W(x,y)$ and $z^R(x,y)$, depend on the location in the contact coordinate system. Real wheel and rail surface profiles are used (see Section 4.1.1). Finally, the wheel and rail contact area deformations are denoted with $u_3^W(x,y)$ and $u_3^R(x,y)$.

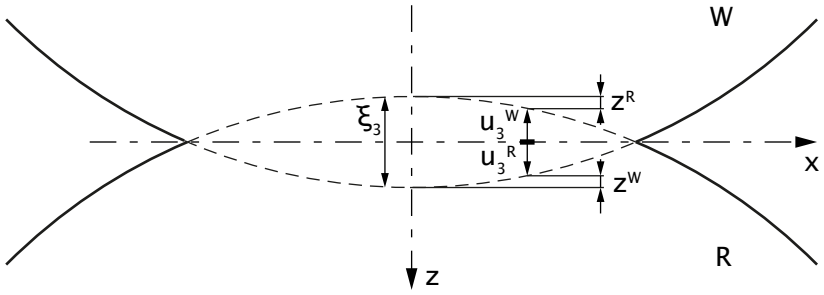

Figure 4.7: Kinematics of two non-conformal surfaces in contact.

The distance between wheel and rail surfaces is given by the distance function $d(x, y)$:

$$d(x, y) = \xi_3 + z^R(x, y) - z^W(x, y) + u_3(x, y), \tag{4.16}$$

where $u_3(x, y) = u_3^R(x, y) - u_3^W(x, y)$ is the deformation difference between the wheel and the rail. The value of the distance function defines whether wheel and rail particles are in contact. Admissible values in the case of wheel/rail contact include positive and zero values. Negative values of the distance function would mean that the bodies penetrate one another.

Positive values of the distance function indicate that the particles at the considered coordinate (x, y) do not come into contact. For particles in contact, the distance function is zero ($d(x, y) = 0$) and Equation (4.16) transforms to

$$u_3(x, y) = -\xi_3 - z^R(x, y) + z^W(x, y), \tag{4.17}$$

which is called the displacement function. Solving Equation (4.17) for coordinates (x, y) around the point of initial contact reveals the contact area shape and size. However, the deformation difference $u_3(x, y)$ is not known in advance, as it depends on the normal contact pressure $p_3(x, y)$. To solve the problem, the relationship between pressure and deformation in the contact area has to be defined.

In Kalker's variational contact model [37] the wheel and rail are locally represented as elastic half-spaces. The relationship between pressure and deformation is thus known in analytical form. Kalker discretized the potential contact area into a finite number of rectangular elements, with each element having constant deformation and pressure values. Figure 4.8 shows the discretization of the potential contact area P into $N_P = n_x \times n_y$ rectangular elements of size $\Delta x \times \Delta y$. In simulations of rolling, the longitudinal dimension of the elements has to satisfy the kinematic relation $\Delta x = v\Delta t$. This assures that in each time-step of the simulation the contact area moves for one element length.

The kinematic Equation (4.16) is solved for each element $I \in P$ with the element location defined by its centre-coordinates (x_I, y_I). Using the elastic half-space solution, the displacement difference defined in Equation (4.17) is obtained for the element I as:

$$u_{I3} = \sum_{J=1}^{N_P} A_{I3,J3} p_{J3}. \tag{4.18}$$

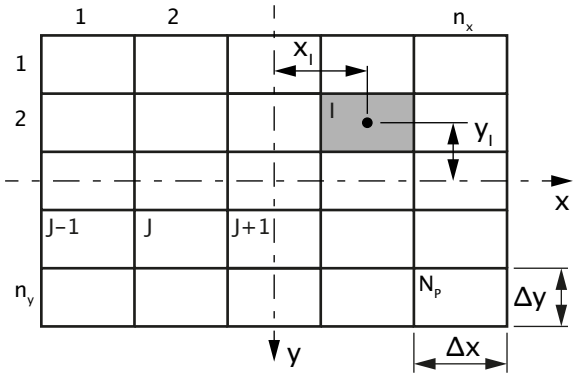

Figure 4.8: Discretization of the potential contact area P into N_P rectangular elements.

The elastic half-space influence coefficient $A_{I3,J3}$ gives the vertical deformation at the centre of element I due to a unit normal pressure acting on element $J \in P$. Expressions for the influence coefficients can be found in [55] and [37]. It is seen that pressures on all elements $J \in P$ influence the deformation of element I. In addition, the wheel and rail are assumed to be of the same material, which leads to the influence coefficients coupling the tangential and normal directions ($A_{I1,J3}$, $A_{I3,J1}$, $A_{I2,J3}$ and $A_{I3,J2}$) to be zero. This simplification was discussed in Section 3.2.2.

The distance function, Equation (4.16), and the displacement function, Equation (4.17), are defined in the discrete form for each element $I \in P$:

$$d_I = \xi_3 + z_I^R - z_I^W + u_{I3}, \tag{4.19}$$

$$u_{I3} = -\xi_3 - z_I^R + z_I^W. \tag{4.20}$$

The contact conditions are formulated in terms of the distance function and the normal contact pressure for each element:

$$d_I \geq 0, \tag{4.21}$$

$$p_{I3} \geq 0, \tag{4.22}$$

$$d_I p_{I3} = 0. \tag{4.23}$$

Equation (4.21) defines the contact kinematics with excluded penetration ($d_I < 0$). Adhesion ($p_{I3} < 0$) between the surfaces is excluded by Equation (4.22), while Equation (4.23) defines the contact condition itself. In the case contact is established the distance function is zero and pressure is positive. If no contact occurs, the distance function is positive, but the pressure is zero. To solve the problem defined by Equations (4.18) to (4.23), Kalker developed an iterative procedure he calls “active set algorithm” implemented in the NORM algorithm [37].

Kalker’s algorithm differs between two sets of elements based on the inequality constraint defined by Equation (4.22). The active set E contains elements where the inequality constraint is active ($p_{I3} = 0$), i.e. elements that are not in contact. The

contact set C contains elements that are in contact and satisfy $p_{I3} > 0$. A detailed description of the algorithm operation is found in [55, 37].

The active set algorithm solves the contact problem for the normal pressure distribution and the contact geometry. The size and shape of the contact area are determined from the contact set C and the element dimensions. Finally, the normal contact force is calculated by summing partial forces acting on each element as:

$$F_3(t_d) = \sum_{I=1}^{N_P} p_{I3} \Delta x \Delta y. \tag{4.24}$$

4.3.2 The tangential contact model

The tangential contact model used in this work is a point-contact model, where the contact is treated globally and contact variables are defined for the complete contact. General properties of point-contact models were discussed in Section 3.2.3 and the discussion is continued in the present section.

The difference between the tangential point-contact model and Kalker's variational tangential-contact algorithm TANG [37] is shown graphically in Figure 4.9. The different nature of the two contact models is immediately noticed. Kalker's TANG relies on the discretization of the contact area to model processes for each particle in contact, Figure 4.9 (a). In contrast, the point-contact model considers processes on the global contact level, Figure 4.9 (b).

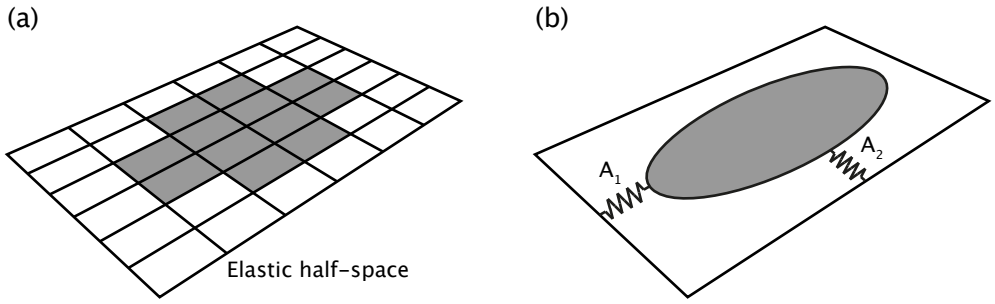

Figure 4.9: Two approaches to the consideration of the contact: (a) discretization and the elastic half-space assumption (Kalker [37]); (b) point-contact and the global-contact springs.

In the global view, the changes of contact variables throughout the contact area cannot be described. While the contact area shape and size do not directly influence the tangential point-contact model, they are considered in the global friction model formulation, Section 4.3.4. The global approach results in a significantly lower number of equations that have to be solved to obtain the tangential problem solution. In Kalker's approach, equations that define the tangential problem have to be solved for each element in contact.

Equation (3.3) is the starting point for the definition of the tangential point-contact model. Both the lateral and the longitudinal directions are considered. The

tangential contact forces in the current time step t_d are defined as:

$$F_\tau(t_d) = -\mu_{RF}(s)\, F_3(t_d)\, \frac{s_\tau(t_d)}{s(t_d)}, \qquad \tau = 1, 2, \tag{4.25}$$

with the absolute slip velocity s in the contact area defined as:

$$s(t_d) = \sqrt{s_1^2(t_d) + s_2^2(t_d)}. \tag{4.26}$$

The longitudinal component s_1 and the lateral component s_2 of the slip velocity s follow from Equation (3.1). Because of the global consideration of the contact, the contact variables are independent of the location in the contact area. The spatial derivative $\partial u_\tau / \partial x$ is then disregarded and Equation (3.1) transforms to:

$$s_\tau = w_\tau + \frac{\partial u_\tau}{\partial t}, \qquad \tau = 1, 2. \tag{4.27}$$

The rigid slip term w_τ is defined in Equation (3.2), while the partial derivative of the displacement with respect to time is approximated with a finite difference:

$$\frac{\partial u_\tau}{\partial t} = \frac{u_\tau(t_d) - u_\tau(t_d - \Delta t)}{\Delta x} v, \qquad \tau = 1, 2, \tag{4.28}$$

where $u_\tau(t_d)$ and $u_\tau(t_d - \Delta t)$ are the current and previous time-step contact deformations, respectively. In the squeal model, only the lateral and vertical dynamics are considered. Additional dynamic terms are, therefore, introduced in the slip equation for the lateral direction (direction 2). As with the contact deformation, it is the difference between two adjacent time-step values that counts towards the slip velocity. Taking that into consideration and using the approximation of Equation (4.27), the final expressions for the slip velocity components are:

$$s_1(t_d) = \left(\gamma_x + \frac{u_1(t_d) - u_1(t_d - \Delta t)}{\Delta x}\right) v, \tag{4.29}$$

$$s_2(t_d) = \left(\gamma_y + \frac{u_2(t_d) - u_2(t_d - \delta t)}{\Delta x} - \frac{\xi_2(t_d) - \xi_2(t_d - \Delta t)}{\Delta x}\right) v, \tag{4.30}$$

where $\xi_2(t_d)$ and $\xi_2(t_d - \Delta t)$ are the current and the previous time-step combined wheel/rail responses, respectively. The term Δx has to satisfy the kinematic relationship $\Delta x = v \Delta t$.

The contact deformation compensates only for part of the rigid slip and wheel/rail dynamic response contribution. The rest is compensated through slip, which is, according to Equation (4.30), the difference between the rigid slip and a combination of the contact deformation and the wheel/rail dynamic contribution.

The mathematical formulation of the tangential point-contact model consists of two non-linear equations, given by Equation (4.25). In comparison, Kalker's variational model defines two equations (linear or non-linear) for each element in contact. In Kalker's model a finer discretization leads to increased precision, but

the computational cost becomes high. The global consideration of the contact avoids discretization and significantly improves computational efficiency.

The price for improved efficiency is the steady-state nature of the point-contact model. This is not immediately noticed as the transient term is retained in Equation (4.27). It is the global consideration of the contact that results in the inability to describe changes in contact variables within the contact area. According to Knothe and Groß-Thebing [40], to model transient phenomena in the contact a model should be able to describe the change of variables on a particle travelling through the contact area. Transient contact phenomena may therefore not be described properly by the tangential point-contact model as they would be with Kalker's model [37].

To completely define the point-contact model, two quantities used in Equations (4.25), (4.29) and (4.30) have to be defined. First, a method for the determination of the global contact deformations u_τ in the tangential directions 1 and 2 is proposed. Second, the friction model $\mu_{RF}(s)$ is defined in a stringent manner.

4.3.3 Determination of the contact compliances

The global consideration of the contact requires the contact deformation to be defined in global terms as well. The need to model the instantaneous contact deformation is further driven by the omission of the first values of the wheel and rail Green's functions (see Sections 4.2.1 and 4.2.2). Two springs with compliances A_τ are therefore introduced in the model, as seen in Figure 4.9. The contact deformation is calculated as:

$$u_\tau = A_\tau F_\tau, \qquad \tau = 1, 2. \tag{4.31}$$

Though not explicitly noted, the contact compliance is non-linear and depends on the contact forces.

The method for the determination of the contact compliance is based on the following assumptions:

- the wheel and rail can be locally represented as elastic half-spaces;
- the tangential contact forces do not change significantly between two adjacent time steps $t_d - \Delta t$ and t_d;
- stick vanishes in the contact area;
- the contact pressure and traction distributions are ellipsoidal.

The first assumption enables for simple determination of the deformation at different points in the contact area. The other assumptions define the loading of the elastic half-space so that its deformations can be calculated. By assuming that the contact forces do not change significantly between two time steps, the compliances can be determined based on the previous time-step values. This avoids two additional non-linear equations that would otherwise be present in the tangential problem formulation. The third assumption defines the distribution of tangential tractions, which are equal to the normal pressure distribution scaled by the friction coefficient.

The method starts from the normal contact problem solution, where the contact area shape and size are taken into consideration. The following steps are performed in each simulation time-step to determine the actual contact compliances:

1. Compute the full-slip tangential tractions distribution from the previous time-step tangential forces $F_\tau\left(t_d-\Delta t\right)$, the current time-step normal force $F_3\left(t_d\right)$ and the normal pressure distribution p_{I3}:

$$p_{I\tau}^{fs}=p_{I3}\frac{F_\tau\left(t_d-\Delta t\right)}{F_3\left(t_d\right)},\qquad \tau=1,2. \tag{4.32}$$

2. Compute the elastic half-space deformation field caused by the tangential tractions determined in step 1:

$$u_\tau^{fs}=A_{\tau1}p_{I1}^{fs}+A_{\tau2}p_{I2}^{fs},\qquad \tau=1,2, \tag{4.33}$$

where $A_{\tau k}$ ($\tau=1,2$, $k=1,2$) are the elastic half-space influence coefficients.

3. Compute the tangential compliances:

$$A_\tau=\frac{\bar{u}_\tau^{fs}}{F_\tau\left(t_d-\Delta t\right)},\qquad \tau=1,2. \tag{4.34}$$

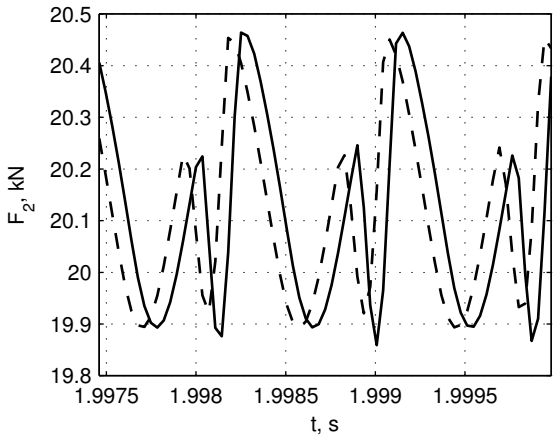

Figure 4.10: Detail of the lateral force time-history for two tangential-contact compliances: (—) Equation (4.34); (- -) double value of Equation (4.34). Squeal case: $\gamma_y=-0.01$, $\mu=0.3$, $\Delta y^{WR}=-10$ mm, $v=50$ km/h.

To compute the mean deformation of the contact area $\bar{u}_\tau^{fs}$, the assumption of ellipsoidal distribution of deformations in the elliptical contact area is used. It is also implicitly assumed that the contact area is elliptical or quasi-elliptical. These assumptions simplify the computation of the mean deformation. The sum of deformations, calculated as a half-ellipsoid volume, is divided by the contact ellipse area to obtain the mean deformation value:

$$\bar{u}_\tau^{fs}=\frac{V_{hel}}{A_{el}}=\frac{\frac{4}{6}\pi ab\cdot\max\left(u_\tau^{fs}\right)}{\pi ab}=\frac{2}{3}\max\left(u_\tau^{fs}\right),\qquad \tau=1,2, \tag{4.35}$$

where a and b are the contact ellipse semi-axes.

On the one hand the assumptions used in the method introduce errors, but on the other hand the squeal model is rather insensitive to variations in the contact compliances. In Figure 4.10, a detail of the time-history of the lateral contact force is presented. The proposed model for curve squeal was used to obtain the results and two different tangential contact compliances were used. The first value of the compliance was obtained directly from Equation (4.34), while the second value was obtained by doubling the first. Despite a two-fold difference in compliances, the results for the contact force do not show any significant differences. It is concluded that the error introduced by the assumptions above is negligible.

4.3.4 Determination of the friction model

The main drawback of the point-contact model is its inability to model processes within the contact area, which includes the inability to determine the contact stick and slip regions. The contact area gradually transitions from complete stick to complete slip conditions with increasing creepage. This results in a gradual build-up of tangential forces from zero for complete stick, to the traction bound μF_3 for complete slip in the contact. In the tangential point-contact model this transition is included in the friction model. Due to the continuous nature of the transition, the friction model is also continuous and is called regularized friction (RF).

When compared to the Coulomb friction model used in Kalker's variational contact model, the regularized friction model is a global friction model that describes friction properties of the complete contact. The Coulomb friction model is a local friction model that defines friction properties on the contact particles level, see Figure 4.11. As a consequence, the slip velocities of the Coulomb and regularized friction models don't have the same physical meaning. In the Coulomb model, the slip velocity represents the micro-slip between contact particles. In contrast, the slip velocity in the regularized friction model represents the slip of the complete contact area.

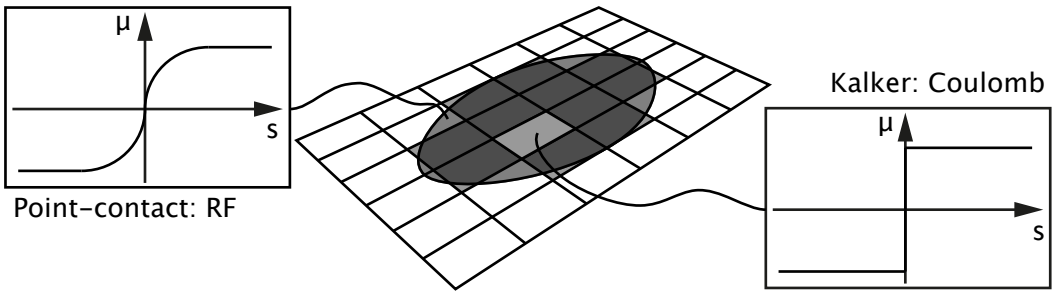

Figure 4.11: Local and global friction models and the level on which the models are defined.

For the local (Coulomb) and global (RF) friction models to describe the same friction properties, the RF model has to be determined in a stringent manner. A

method for the determination of the RF model is proposed. The method applies Kalker's variational contact model and takes into account the contact area shape and size.

A RF model is determined for each value of the Coulomb friction coefficient and for each nominal contact point that leads to a different contact area shape and size. The lateral creepage input into Kalker's variational model is defined to vary according to:

$$\gamma_y^{RF} = \gamma_y^{lim} \frac{t}{t_{end}}, \tag{4.36}$$

where the creepage limit is $\gamma_y^{lim} = -0.05$, and the end time is $t_{end} = 2$ s. The wheel and rail dynamics are not considered and the wheel/rail displacement response terms (ξ_3, ξ_2) are not included in the contact kinematic equations[3]. The lateral contact force F_2^{RF} is obtained from Kalker's contact model, which relates the force value to a certain lateral creepage value. The normal contact force F_3^{RF} is constant as there are no dynamic effects.

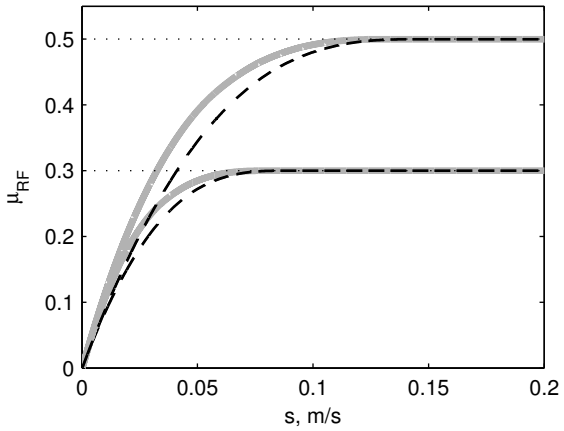

Figure 4.12: Regularized friction curves for friction coefficient values $\mu = 0.3$ and $\mu = 0.5$ and wheel/rail contact geometries obtained for the lateral wheelset offset $\Delta y^{WR} = -15$ mm (— grey) and $\Delta y^{WR} = -10$ mm (- - black).

Although Kalker's model is transient, a steady-state solution is assumed in each time step. This assumption is valid as long as the input creepage is slowly varying in time. Steady-state contact conditions are then achieved in every time step. The RF friction model is defined with the $\mu_{RF}(s)$ characteristic[4]:

$$\mu_{RF}(s) = \frac{F_2^{RF}(s)}{F_3^{RF}}. \tag{4.37}$$

[3]For the normal contact problem the kinematic equation is given by Equation (4.19). Kalker's variational model for the tangential contact is not part of the present work. The relevant kinematic equations can be found in [37, 55].

[4]The regularized friction model, calculated as the ratio of the lateral and vertical force is often called "traction coefficient" in the literature specific to rail vehicle dynamics.

The slip velocity of the contact is related to the lateral creepage by the rolling velocity $s = \gamma_y^{RF} v$. Because the wheel and rail dynamics are not included, the slip velocity is equal to the rigid slip of Equation (3.2).

In Figure 4.12 four regularized friction models are presented. The models were obtained for different values of the Coulomb friction coefficient and different wheel/ rail contact geometries. Besides a higher asymptotic value, a higher friction coefficient results in a longer transition region from complete stick ($s = 0$) to complete slip (high s). The contact geometry influences only the shape of the transition region.

4.4 Sound radiation from a railway wheel

The ability to evaluate the radiated sound is considered important for an engineering model for curve squeal. Squeal is a noise disturbance and its severity is best evaluated by considering its sound levels. As discussed in Section 2.1, the railway wheel shows a high vibration response in comparison to the rail. In combination with the high sound-radiation efficiency of the wheel, this makes it the dominant sound radiator in curve squeal. The evaluation of the radiated sound is therefore limited to the wheel contribution. The rail is not considered to contribute significantly [77].

The task of evaluating the radiated sound can be a computationally very expensive task, as in the case of the boundary element method (BEM). For engineering purposes, a computationally efficient and simple sound radiation model is desirable, even at the cost of accuracy. A suitable model was developed by Thompson and Jones [74], which is based on modal expansion techniques. The model is also implemented in the TWINS software and additional information can be found in [73].

Thompson and Jones used the boundary element method to determine the radiation efficiencies of each wheel mode. In BEM, the sound field radiated from the wheel was evaluated over a spherical mesh surrounding the wheel model [74]. Radiation efficiencies of each mode were computed for a defined frequency range and analytical functions were fitted to the computed data. These functions take into account the geometry of the wheel and make the model applicable to wheels of different geometries. The determined analytical functions for the radiation efficiencies form the backbone of the sound radiation model.

Contributions to the overall sound radiated from the wheel were identified for the axial, radial and torsional motion of the wheel cross section. In Figure 4.13 (a) the motions of the cross section are shown.

The model evaluates the radiated sound power W^W at a frequency f for wheel modes with the same number of nodal diameters n from the wheel velocity field $\overline{\tilde{v}^2}$:

$$W^W(n,f) = \rho c_0 \sum_n \left[\sigma_a(n,f) \sum_{q=1}^{N_a} \left(S_{aq} \overline{\tilde{v}_{aq}^2}(n,f) \right) + \sigma_r(n,f)\, S_r \overline{\tilde{v}_r^2}(n,f) + \sigma_t(f)\, S_t \overline{\tilde{v}_t^2}(n,f) \right]. \quad (4.38)$$

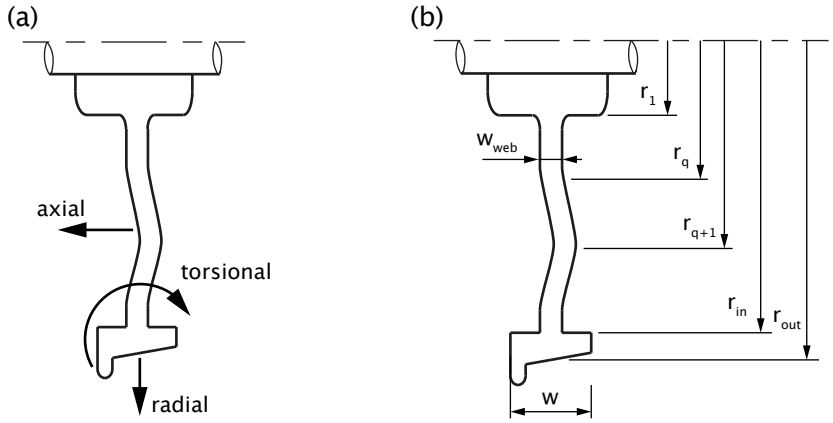

Figure 4.13: Railway wheel cross section: (a) possible motions; (b) dimensions of the sound radiation surfaces.

The speed of sound in air is denoted with c_0 and the air density with ρ. The axial, radial and torsional motion radiation efficiencies are σ_a, σ_r and σ_t, respectively. The sound radiation surfaces from which sound is radiated due to the three cross-section motions are denoted with S_{aq}, S_r and S_t. The axial surface is divided into N_a annular surfaces S_{aq}, each defined with two radii r_q and r_{q+1}, $r_1 \leq r_q < r_{out}$. Figure 4.13 (b) shows the main dimensions of the wheel cross section from which the surface areas are determined.

In the following sections the relationships that define the axial, radial and torsional radiation efficiencies are given. After the radiation efficiencies are defined, the surface areas and the velocity field on the C20 wheel are described.

4.4.1 Radiation efficiencies

The radiation efficiencies depend on both frequency f and the number of nodal diameters n of the wheel mode. The expressions for the radiation efficiencies are originally found in [73] and are repeated here for the sake of completeness.

Axial motion

The axial motion radiation efficiency has the form of a monopole [74]:

$$\sigma_a(n, f) = \frac{1}{1 + \left(\frac{f_{ca}(n)}{f}\right)^{2n+4}}, \tag{4.39}$$

where f_{ca} is the critical (transition) frequency for the axial motion of the wheel cross section:

$$f_{ca}(n) = \frac{c_0 \kappa(n)}{2\pi r}. \tag{4.40}$$

The radius r is the nominal rolling radius of the wheel and the coefficient κ is defined as:

$$\kappa(n) = 1.9 + 1.015n - 0.0189n^2. \tag{4.41}$$

Note that both radiation efficiency and critical frequency are dependent on the number of nodal diameters n, i.e. the wheel mode shape.

Radial motion

The radiation efficiency for the case of the wheel cross-section radial motion is more complex due to the wheel geometry and sound cancellation [74]:

$$\sigma_r(n, f) = \begin{cases} \frac{\Gamma}{1+\left(\frac{f_{r2}(n)}{f}\right)^2}, & \text{for } n = 0, \\ \frac{\Gamma}{1+\left(\frac{f_{r1}(n)}{f}\right)^{2n}} \cdot \frac{1}{1+\left(\frac{f_{r2}(n)}{f}\right)^2}, & \text{for } n > 0, \end{cases} \tag{4.42}$$

where the critical frequencies f_{r1}, f_{r2} and f_{r3} are:

$$f_{r1}(n) = \frac{120n}{\sqrt{\frac{r}{0.42}}}, \tag{4.43}$$

$$f_{r2} = \frac{800}{\sqrt{\frac{r}{0.42}}}, \tag{4.44}$$

$$f_{r3}(n) = \frac{280 + 150n}{\sqrt{\frac{r}{0.42}}}. \tag{4.45}$$

The parameter Γ takes into account the cancellation between the inner and outer tyre[5]:

$$\Gamma = \begin{cases} \sqrt{\frac{S_{out}-S_{in}}{S_{out}+S_{in}}}, & \text{for } f < f_{r3}, \\ 1, & \text{for } f > f_{r3}, \end{cases} \tag{4.46}$$

with the tyre tread and inner tyre surfaces calculated from:

$$S_{out} = 2\pi r w, \tag{4.47}$$

$$S_{in} = 2\pi r_{in}(w - w_{web}). \tag{4.48}$$

Torsional motion

The radiation efficiency for the torsional motion of the wheel cross section is independent of the number of nodal diameters:

$$\sigma_t(f) = \frac{1}{1 + \left(\frac{f_{ct}}{f}\right)^4}, \tag{4.49}$$

[5]The wheel tyre is the ring-shaped part of the wheel on which the wheel flange and wheel tread are located, up to the point where the wheel web starts.

where the critical frequency f_{ct} is

$$f_{ct} = \frac{2c_0}{\pi w}. \tag{4.50}$$

The contribution of the torsional motion is generally neglected in the overall radiated sound from the wheel [73].

4.4.2 Sound radiation surfaces

The cross section of the C20 wheel is shown in Figure 4.14, where the FE nodes on the wheel cross-section boundary are marked. Main dimensions that determine the sound radiation surface areas are noted in the figure.

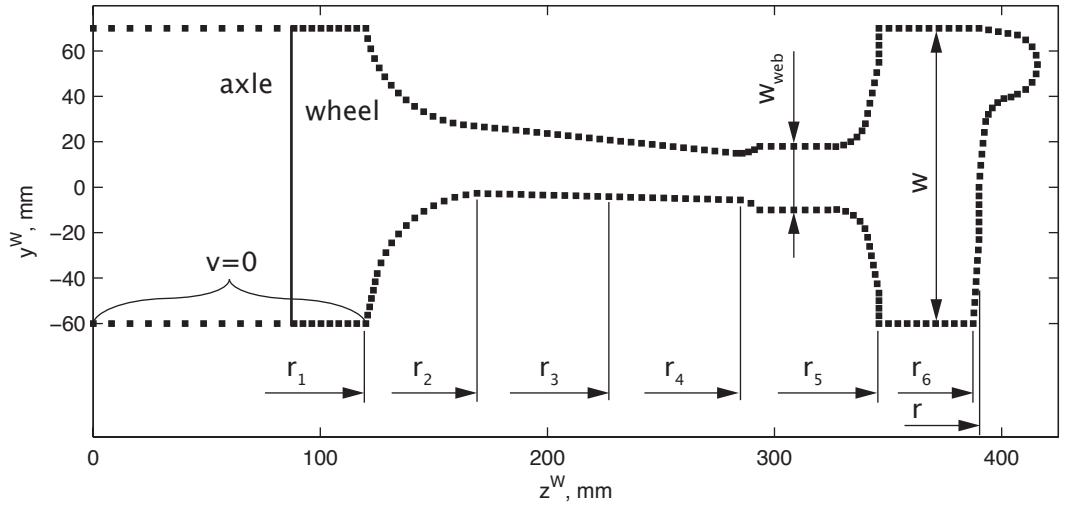

Figure 4.14: C20 wheel cross-section nodes and division into axial-surface sections.

The axial surface of the wheel is divided into five ($n_q = 5$) annular surfaces S_{aq} bounded by radii r_{q+1}, $q = 1, \ldots, n_q$. The greatest part of the axial surface belongs to the wheel web and only a small portion to the wheel tyre axial surface. Surface areas of the annuli are calculated as:

$$S_{aq} = 2\pi \left(r_{q+1} - r_q\right), \qquad q = 1, \ldots, 5. \tag{4.51}$$

The surface areas from which sound is radiated due to radial motion of the wheel cross section are surfaces with a normal vector that is parallel (or close to parallel) to the radial direction. These surfaces include the wheel tread and the inner surface of the wheel tyre:

$$S_r = 2\pi \left[rw + r_5 \left(w - w_{web}\right)\right]. \tag{4.52}$$

Finally, despite torsional motion not being included in the model, relations for the torsional motion surfaces are nonetheless provided. The torsional velocity has the dimension of rad/s, thus the corresponding surface has the dimension of m^4

to convert the angular velocity into volume velocity (m^3/s). The related surfaces consist of the wheel tread surface, the inner surface of the wheel tyre and the two axial surfaces of the wheel tyre:

$$S_t = \frac{\pi}{6}\left[rw^3 + r_5\left(w^3 - w_{web}^3\right) + (r + r_5)(r - r_5)^3\right]. \tag{4.53}$$

4.4.3 Wheel velocity field

In Equation (4.38) the velocity fields on wheel surfaces are weighed with the corresponding surface areas and radiation efficiencies. The velocity fields on surfaces are expressed with spatially averaged, mean-square velocities $\overline{\tilde{v}^2}$. The velocities are obtained at nodes of the wheel cross section in the axial direction y^W for axial surfaces and the radial direction z^W for radial surfaces.

The complex velocity at a degree of freedom i due to the complex excitation $\hat{F_{jk}}(f)$ at the node j (nominal contact point) and in direction k is obtained from the wheel receptances G_{ijk}^W of Equation (4.2):

$$v_{ij}(n, f) = \mathrm{i}2\pi f G_{ijk}^W(n, f)\,\hat{F_{jk}}(f). \tag{4.54}$$

Together, indices j and k determine the excitation degree of freedom. In the receptances G_{ijk}^W only modes with the same number of nodal diameters n are included and the velocity field is evaluated for every n separately. Both the axial and the radial excitation are included in the model and $\hat{F_{jk}}(f)$ is the amplitude spectra of the contact forces. As the longitudinal dynamics is not included in the engineering squeal model, circumferential excitation of the wheel is not included in the sound radiation model. Therefore, the complex velocity $v_{ij}(n, f)$ of Equation (4.54) consists of two contributions:

$$v_{ij}(n, f) = 2\pi f\left[\mathrm{i}G_{ij2}^W(n, f)\,\hat{F_{j2}}(f) + \mathrm{i}G_{ij3}^W(n, f)\,\hat{F_{j3}}(f)\right]. \tag{4.55}$$

The receptances G_{ij2}^W and G_{ij3}^W give the response in the degree of freedom i due to the lateral and vertical excitation at the wheel/rail nominal contact point.

The mean-square velocity is obtained as

$$\tilde{v_i}^2(n, f) = \begin{cases} |v_i(n, f)|^2, & \text{for } n = 0, \\ 0.5|v_i(n, f)|^2, & \text{for } n \neq 0. \end{cases} \tag{4.56}$$

The factors 1 and 0.5 in front of the $|v_i(n, f)|^2$ term come from the mean-square value of the $\sin(n\varphi)$ term that describes the velocity field along the wheel circumference. Spatial averaging is performed over the number n_i of degrees of freedom i according to

$$\overline{\tilde{v}^2}(n, f) = \frac{\sum_i \tilde{v_i}^2(n, f)}{n_i}. \tag{4.57}$$

The wheelset axle is included in the model, but it is considered fixed and velocities on its surface are set to zero. Because of the negligible amplitudes of the velocities on the wheel surface near the axle, the circular surface area $r_1^2\pi$ is not considered (see Figure 4.14).

Chapter 5

Validation

In this chapter the validation of the implementation of the simple model for sound radiation is carried out, along with the validation of the tangential point-contact model. The sound-radiation model is validated against results of the boundary element method (BEM) in Section 5.1. In the case of the tangential point-contact model a two-fold validation procedure is proposed in Section 5.2. The contact model is validated against Kalker's variational model within the squeal model, i.e. with the included dynamics of the wheel and rail (Section 5.2.2). Additionally, a traditional approach to validation is carried out, where the creepage variation is imposed and the contact model is considered independently (stand-alone, Section 5.2.1). The proposed validation procedure gives more information about the applicability of different rolling contact models for curve squeal modelling.

5.1 Validation of the sound-radiation-model implementation

The simple sound-radiation model, described in Section 4.4, has been developed by Thompson and Jones [74] from BEM analyses of sound radiation from a railway wheel. The model implementation is therefore validated against results of BEM analyses, which were carried out using the BEM code developed by Brick [11]. The wheel tread is lifted for 0.15 m (approx. the rail height) above the hard ground and ground reflections are taken into account. The ensuing sound field is evaluated over a half-sphere surrounding the wheel, as shown in Figure 5.1 (a). Evaluation points of the sound field are located far enough from the wheel for the far-field assumption to be valid.

The simple sound-radiation model is validated in two different cases. Firstly, the radiated sound power is evaluated for the case with unit excitation force at frequencies around selected wheel modes. Secondly, the radiated sound power is evaluated for a simulated squeal case.

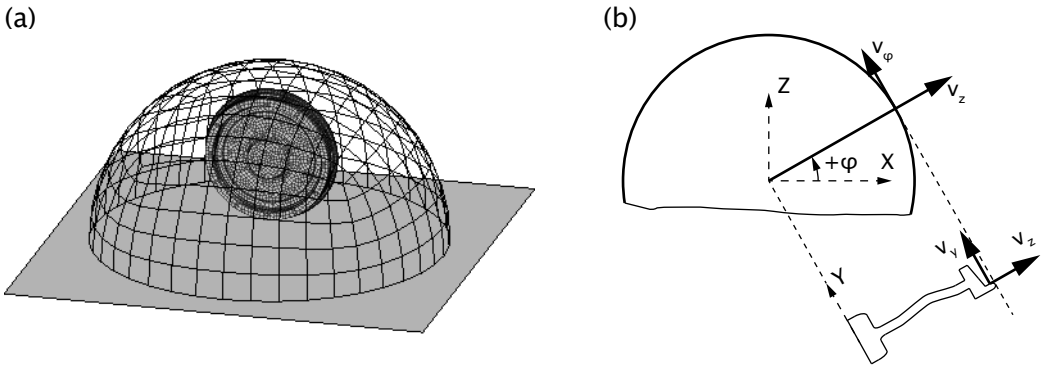

Figure 5.1: C20 wheel boundary element model: (a) BE mesh, the reflecting ground and the sound-field evaluation mesh; (b) coordinate transformation.

Velocities at the nodes of the BE model have to be determined from the wheel FE model velocities defined in Equation (4.55). The coordinate systems transformation between the wheel BE and FE models[1] has to be determined. Additionally, the circumferential distribution of the velocity field (described by $\sin(n\varphi)$ or $\cos(n\varphi)$, Section 4.2.1) has to be taken into account. The velocities in the BEM (X, Y, Z) coordinate system are obtained from the FE model velocities v_x, v_z and v_φ for each circumferential angle φ and number of nodal diameters n as:

$$v_X(n,\varphi) = v_x \cos(n\varphi)\cos(\varphi) - v_\varphi \sin(n\varphi)\sin(\varphi), \tag{5.1}$$

$$v_Y(n,\varphi) = v_y \cos(n\varphi), \tag{5.2}$$

$$v_Z(n,\varphi) = v_x \cos(n\varphi)\sin(\varphi) + v_\varphi \sin(n\varphi)\cos(\varphi). \tag{5.3}$$

As used in the equations above, the terms $\sin(n\varphi)$ and $\cos(n\varphi)$ are valid for the case of radial (vertical) and axial (lateral) wheel excitation.

In both validation cases the wheel is excited at the nominal wheel/rail contact point defined with $\Delta y^{WR} = -15$ mm ($y^W = -32$ mm, Figure 4.3 (b)).

5.1.1 Validation with unit-force excitation

Axial wheel modes with zero nodal circles are commonly found to be excited during squeal [77, 42]. The sound model validation is therefore performed for frequencies around modes $(0,0,a)$, $(1,0,a)$, $(2,0,a)$ and $(3,0,a)$.

The BE model of the wheel has a typical element dimension of $l_{elem} = 0.034$ m. Of the selected modes, mode $(3,0,a)$ has the highest eigen-frequency of about $f_{max} = 1144$ Hz, resulting in the number of elements per wavelength of $n_{elem/\lambda} = c_0/(f_{max} l_{elem}) = 8.8$. This is well within the range of six to ten elements per acoustic wavelength recommended in the literature [48].

[1]The superscript W, which denotes the wheel, is omitted from the FE model axes notation. In this chapter, the wheel model coordinate system (y^W, z^W, φ^W) is denoted with (y, z, φ).

The frequency resolution required to describe the resonance peaks reasonably well is determined from the wheel receptances, Figure 4.4. About five to seven frequency points should be present in the frequency region around a resonance peak. This frequency region is determined from points in the receptance magnitude plot which are 3 dB lower than the receptance value at the resonance. Table 5.1 shows the selected wheel modes, corresponding eigen-frequencies and the required frequency resolution. Figure 5.2 shows the shape of the lateral velocity field on the wheel surface obtained by exciting the wheel with a unit lateral excitation at the wheel tread. The excitation frequency corresponds to the wheel mode under consideration. Mode shapes of the four wheel modes are clearly distinguished.

Mode	$\mathbf{f_r}$, **Hz**	$\mathbf{\Delta f}$, **Hz**
$(0, 0, a)$	332.8	0.13
$(1, 0, a)$	243.2	0.8
$(2, 0, a)$	429.9	0.012
$(3, 0, a)$	1143.2	0.045

Table 5.1: Wheel modes selected for the sound-model validation: eigen-frequencies and the required frequency resolution.

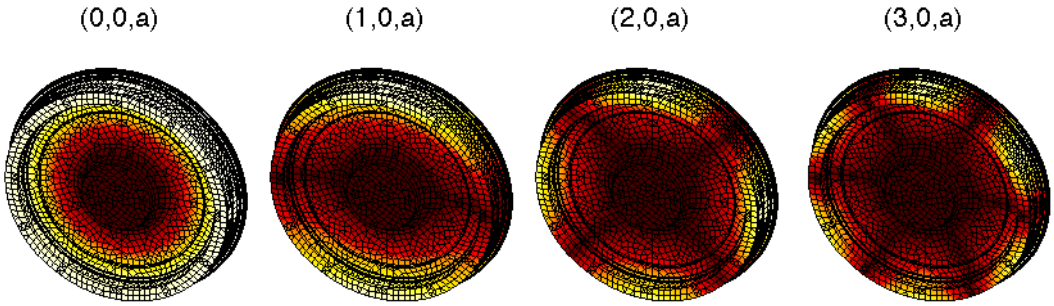

Figure 5.2: Shape of the lateral velocity field v_Y on the wheel surface. The frequency of the lateral unit-excitation force corresponds to the wheel mode eigen-frequency.

The simple sound-radiation model is validated for cases with pure lateral and pure radial wheel excitation. Figure 5.3 shows the difference between the BEM and the simple model results for the case of lateral wheel excitation. Results are presented in terms of the absolute difference of the radiated sound power levels, $\Delta L_W = L_W^{BEM} - L_W^{simple}$. Figure 5.4 shows the validation results for the case of radial wheel excitation. The absolute differences between BEM and the simple model are practically identical for both the lateral and the radial excitation. This indicates that the differences between the two approaches (BEM and simple model) are independent of the wheel excitation.

The absolute differences are, however, dependent on the velocity-field shape, i.e. wheel modes. Differences are in the range of 0.5 to 4 dB, with the simple model overestimating the sound power compared to BEM results. This is attributed to

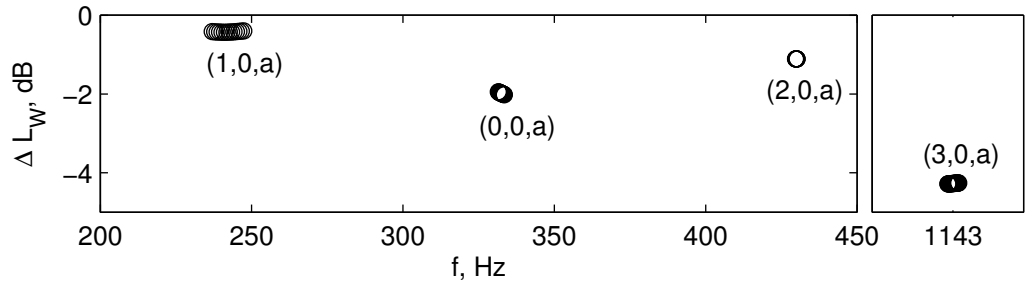

Figure 5.3: Absolute sound-power level difference $\Delta L_W = L_W^{BEM} - L_W^{simple}$ for lateral wheel excitation for frequencies around the selected wheel modes.

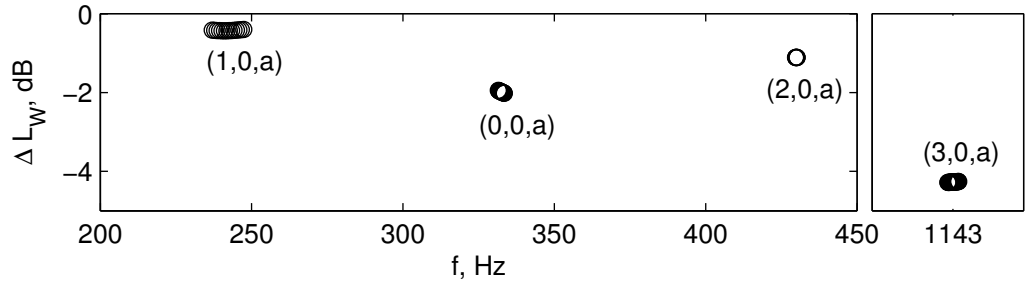

Figure 5.4: Absolute sound-power level difference $\Delta L_W = L_W^{BEM} - L_W^{simple}$ for radial wheel excitation for frequencies around the selected wheel modes.

ground reflections, which are included in the BE model, and to the evaluation of the sound field over a half-sphere. In contrast, Thompson and Jones [74] computed the radiation efficiencies by evaluating the sound field over a sphere, without ground reflections. A monopole placed directly in front of a hard reflecting surface leads to a 3 dB sound power increase (double power). In practical cases, this increase depends on the source geometry, its shape of vibration and the relation between the sound wavelength and the distance between the source and the reflecting surface.

5.1.2 Validation for a curve squeal case

The second part of the validation consists of evaluating the radiated sound power for a simulated curve squeal case. The contact forces were obtained using the squeal model developed in Chapter 4, with the squeal case being defined with a friction coefficient value of 0.35 and a lateral creepage value of -0.014. Negative values of the lateral creepage are obtained for the case of under-radial curving of the wheelset [6]. The vehicle rolling velocity is 50 km/h and the simulation time step is 36 μs. Figure 5.5 shows the lateral and vertical contact-force amplitude spectra, which are obtained from the force time histories. The wheel is excited simultaneously with lateral and vertical forces.

Good agreement is found between BEM and the simple model results in terms of the radiated sound power presented in Figure 5.6 (a). The absolute difference

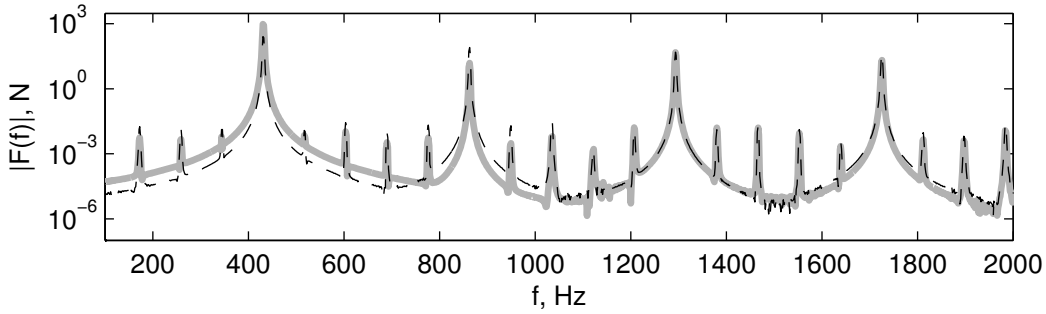

Figure 5.5: Magnitude of the contact-force amplitude spectra: (- - black) lateral contact force; (— grey) vertical contact force.

between the two results is presented in Figure 5.6 (b). Differences in the radiated sound-power levels are comparable to the differences found in the validation with the unit-excitation force, Section 5.1.1. Larger differences, up to 5 dB, are observed at frequencies where the sound power levels are relatively low. The overall (total) sound-power level is lower than the maximum differences. From the BEM results, the overall sound power is 136.3 dB, compared to 138.9 dB obtained from the simple model results. This gives a difference of less than 3 dB between the two approaches.

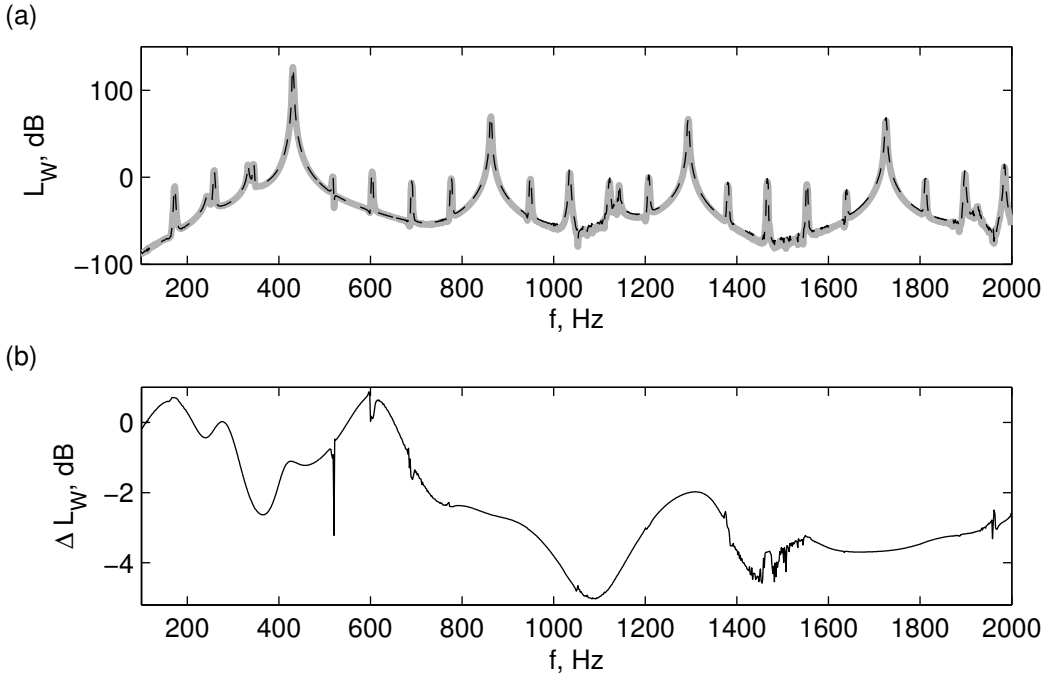

Figure 5.6: Radiated sound power for the squeal case $\mu = 0.35$, $\gamma_y = -0.014$ and $\Delta y^{WR} = -15$ mm: (a) sound-power spectrum: (- - black) simple model; (— grey) BEM; (b) absolute difference between BEM and the simple model results.

In summary, the implementation of the simple sound-radiation model is found

valid with acceptable results compared to the BEM approach. Differences between the results of the two approaches are attributed to the influence of ground reflections included in the BE model used in the validation. These were not included in the BE model used by Thompson and Jones [74]. The simple model for sound radiation from a railway wheel is an approximate model and more sources of error may exist.

5.2 Validation of the contact model

The steady-state nature of the tangential point-contact model developed in Section 4.3.2 may influence the accuracy of the squeal model. Especially important is the ability to predict squeal occurrence (squeal or no squeal) and squeal amplitudes.

In this section, the point-contact model is validated against the transient Kalker's variational contact model in a two-fold validation approach. The contact model is first validated for the case of prescribed motion. Then, a validation within the squeal model is performed with the system dynamics defining the demands on the contact model.

The main question is up to which frequency does the steady-state point-contact model give acceptable results compared to the transient Kalker's variational model. This also defines the validity limit of the time-domain engineering model for curve squeal. The case with prescribed motion puts different demands on the contact model compared to the case when the wheel and rail dynamics are included. In the latter case, the contact model input is variable and depends on the system response and the contact forces. Due to the coupling between the system response and the contact forces, i.e. input and output, it is sensible to validate the tangential point-contact model in dynamic conditions. This closely replicates the real operating conditions of the contact model and gives more information about its applicability. To show the differences between the two validation approaches, the model is validated with prescribed creepage as well.

5.2.1 Validation with prescribed motion

The contact models are first considered as stand-alone entities, with the dynamic response of the wheel and the rail not included in Equations (4.19), (4.20), (4.29) and (4.30). The case of prescribe wheel/rail motion corresponds to a prescribed creepage between the wheel and the rail. Figure 5.7 describes the procedure graphically.

The input lateral creepage is varying sinusoidally around a mean value γ_y^0 with amplitude γ_y^a and frequency f:

$$\gamma_y(t) = \gamma_y^0 + \gamma_y^a \sin(2\pi f t). \tag{5.4}$$

Two validation cases are defined, each case with different creepage parameters and wheel/rail nominal contact position. Case 1 is defined with $\gamma_y^0 = -0.01$ and $\gamma_y^a = 0.005$ with the nominal contact point defined with $\Delta y^{WR} = -10$ mm. Frequencies

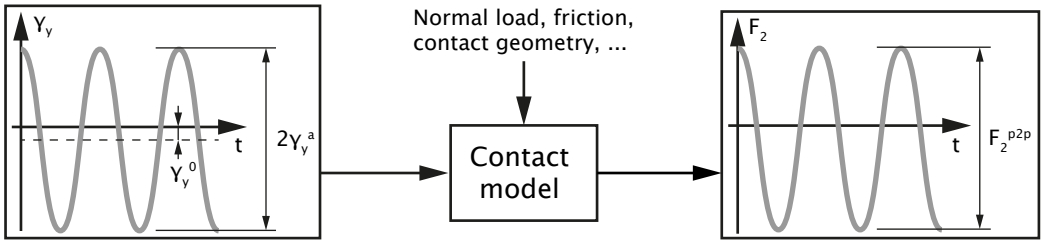

Figure 5.7: Procedure of the contact model validation with prescribed variation of the lateral creepage.

for which the validation was performed are 240, 330, 430, 1140, 1900, 2100 and 3000 Hz.

Case 2 parameters are $\gamma_y^0 = -0.005$ and $\gamma_y^a = 0.005$ with the wheel/rail contact point $\Delta y^{WR} = -15$ mm. This validation case was run for creepage variation frequencies of 240, 330, 430, 1100, 2100, 3100, 4100, 5200 and 6300 Hz. The vertical wheel pre-load $F_{L3} = 65$ kN, the rolling velocity $v = 50$ km/ and the simulation time-step length $\Delta t = 36$ μs are common to both cases.

Results are given in terms of the lateral contact force expressed with its peak-to-peak (p2p) amplitude value F_2^{p2p}, as shown on Figure 5.7. The procedure shown in Figure 5.7 is carried out twice: once with Kalker's variational contact model and once with the point-contact model. Results of Kalker's model are taken as reference.

Figure 5.8 (a) and (b) presents the validation results in terms of the lateral force amplitudes for Case 1 and Case 2, respectively. Relative differences between Kalker's model and the point-contact model are presented in Figure 5.8 (c) for both cases. Significant differences are noticed between Kalker's model and the point-contact model results. The differences between the two contact models are frequency dependent. In addition, the two validation cases show different behaviour.

Case 1 shows a higher relative difference between the two contact models compared to Case 2, see Figure 5.8 (c). However, in both cases the point-contact model deviates substantially for frequencies above roughly 400 Hz. The L/a_x ratio, introduced in Section 3.2.1, has a value of 2.9 (vehicle velocity $v = 50$ km/h and contact length $a_x = 12$ mm). This is well below the $L/a_x = 10$ ratio suggested by Knothe and Groß-Thebing [40], under which transient contact conditions should be considered. Under these conditions, an observed tendency is that the lateral force amplitude obtained from Kalker's variational model steadily decreases with increasing frequency. The same decrease is significantly less pronounced in the results of the tangential point-contact model. This is attributed to the steady-state nature of the point-contact model, which is unable to describe high-frequency processes in the contact area properly.

An important difference between validation Case 1 and Case 2 is found in the values of the lateral contact-force amplitude. Case 2 shows very high values of the force amplitude compared to Case 1. This is attributed to the different creepage-variation parameters and the different geometry of the surfaces in contact. The

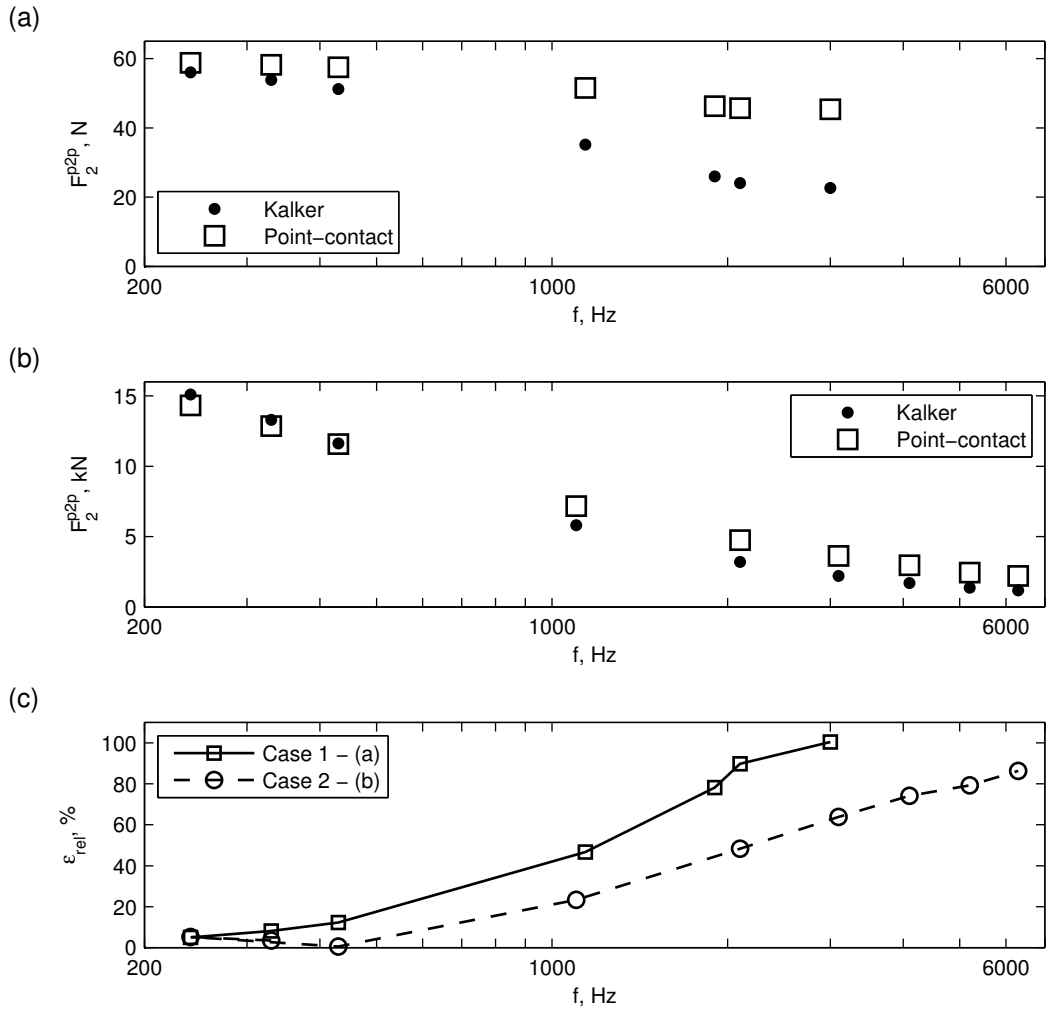

Figure 5.8: Peak-to-peak amplitudes of the lateral contact force due to harmonic creepage variation: (a) Case 1; (b) Case 2: (•) Kalker's variational model; (□) point-contact model; (c) relative difference between the contact models in the validation: (-□-) Case 1; (-o-) Case 2.

differences between the cases point to a dependency of the validation results on the creepage-variation parameters.

In conclusion, the results obtained from the validation with prescribed creepage are in line with observations from Knothe and Groß-Thebing [40]. To solve transient contact problems that involve a prescribed motion or prescribed force, the contact model should be chosen according to the guidelines given in [40], discussed in Section 3.2.1. As is seen from Figure 5.8, the differences between results of a transient and steady-state contact model are large for the prescribed creepage case. According to these results, a transient contact model should be used in squeal models even for simulating squeal of lower frequencies (around 400 Hz). However, the differences between the point-contact model and Kalker's transient model become significantly

lower when the models are compared within the squeal model. This is discussed in the following section.

5.2.2 Validation in dynamic conditions

The displacement response terms are included in Equations (4.19), (4.20), (4.29) and (4.30), which leads to the contact model input being subject to dynamic variations determined by the system itself. Under these circumstances the wheel/rail system dynamics will determine the frequency of the response. However, without further interventions instability would be obtained only at a single frequency (and its higher harmonics).

In an attempt to obtain more response frequencies from the wheel/rail system, the wheel dynamics is altered. Only one wheel mode at a time is included in the wheel response. Figure 5.9 shows examples of the vertical-lateral wheel cross receptance obtained when a single mode is included in the wheel response, with its modal damping set to:

$$\zeta_{incl} = 10^{-6}, \tag{5.5}$$

Other modes were critically damped, $\zeta_{not-incl} = 1$. The wheel suspension was retained, along with the original rail dynamics. The wheel Green's functions are obtained from the modified receptances.

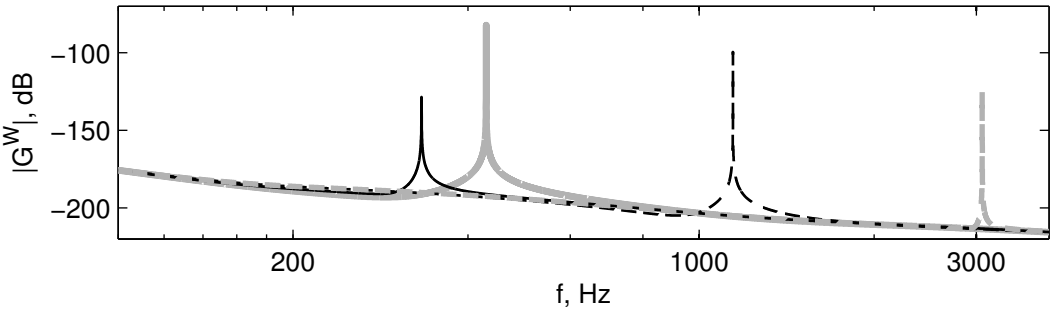

Figure 5.9: Examples of the wheel vertical-lateral cross receptance for cases when a single mode is included and with $y^W = -4$ mm: (— black) mode $(0, 0, a)$; (— grey) mode $(2, 0, a)$; (- - black) mode $(3, 0, a)$; (- - grey) mode $(5, 0, a)$.

In the present approach, the number of simulations is equal to the number of wheel modes (34 modes, see Table 4.1), as one simulation per wheel mode is carried out. The simulation parameters are: $\Delta y^{WR} = -15$ mm wheel/rail contact point, $\mu = 0.6$ friction coefficient, $\gamma_y = -0.04$ lateral creepage, $v = 50$ km/h vehicle velocity, $F_{L3} = 65$ kN vertical wheel pre-load and $\Delta t = 36$ μs simulation time-step length.

Table 5.2 presents the lateral contact-force amplitudes obtained from the validation in dynamic conditions. Only wheel modes for which the system has responded with unstable motion (squeal) are presented, other modes did not result in squeal. The same results are presented graphically in Figure 5.10 (a). Wheel modes that

Mode	f_r, Hz	K F_2^{p2p}, N	P F_2^{p2p}, N	L/a_x
$(1,0,a)$	243.2	6609.7	5917.6	4.76
$(0,0,a)$	332.8	3117.5	3000.1	3.48
$(2,0,a)$	429.9	9601.3	9859.8	2.69
$(3,0,a)$	1143.2	15836.2	17222.3	1.01
$(4,0,a)$	1923.9	11037.6	12973.8	0.6
$(5,0,a)$	3070.8	12242.2	11748.6	0.38
$(6,0,a)$	4131.1	5917.8	6180.4	0.28
$(7,0,a)$	5215.9	7073.2	7223.4	0.22
$(8,0,a)$*	6315.6	72.8	38.1	0.18

Table 5.2: Numeric results of the validation in dynamic conditions. The mode eigen-frequency, lateral force p2p amplitudes and L/a_x ratios are given. * = modes resulting in low amplitudes; K = Kalker's model; P = point-contact model.

resulted in squeal are axial modes with zero nodal circles, which agrees with observations from the literature [77, 42, 72].

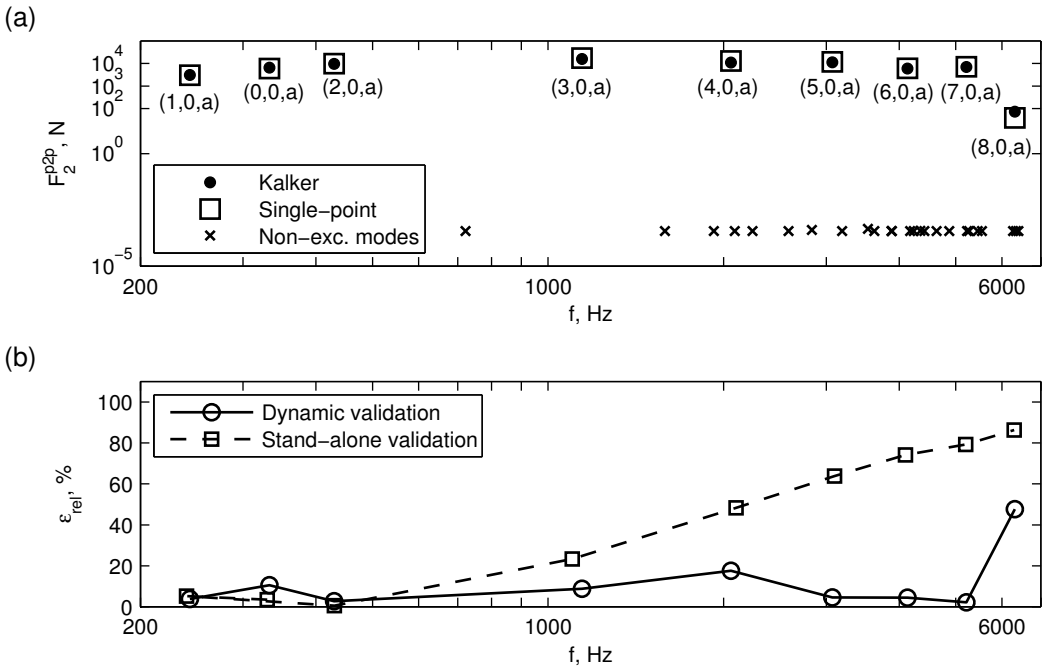

Figure 5.10: Results of the validation under dynamic conditions: (a) lateral contact-force p2p amplitudes, (•) Kalker, (□) point-contact model, (×) wheel modes that were not excited; (b) relative difference between the two contact models: (-o-) dynamic and (-□-) stand-alone validation.

Good agreement between Kalker's model and the point-contact model results is noticed, especially for squeal cases with high lateral force amplitudes. The case with mode $(8,0,a)$ provides a low force amplitude and a high relative difference

between the two contact models. Relative differences computed from results of both prescribed-motion and dynamic validations are presented in Figure 5.10 (b). While the relative difference is frequency dependent for the case of the prescribed-motion validation, such a dependency is not seen in the validation within the squeal model. In comparison to the prescribed-motion validation, the steady-state point-contact model shows good results for L/a_x ratios as low as 0.22. For such a low L/a_x ratio the contact conditions are definitely transient, yet the steady-state model returns results which are very close to Kalker's transient model results.

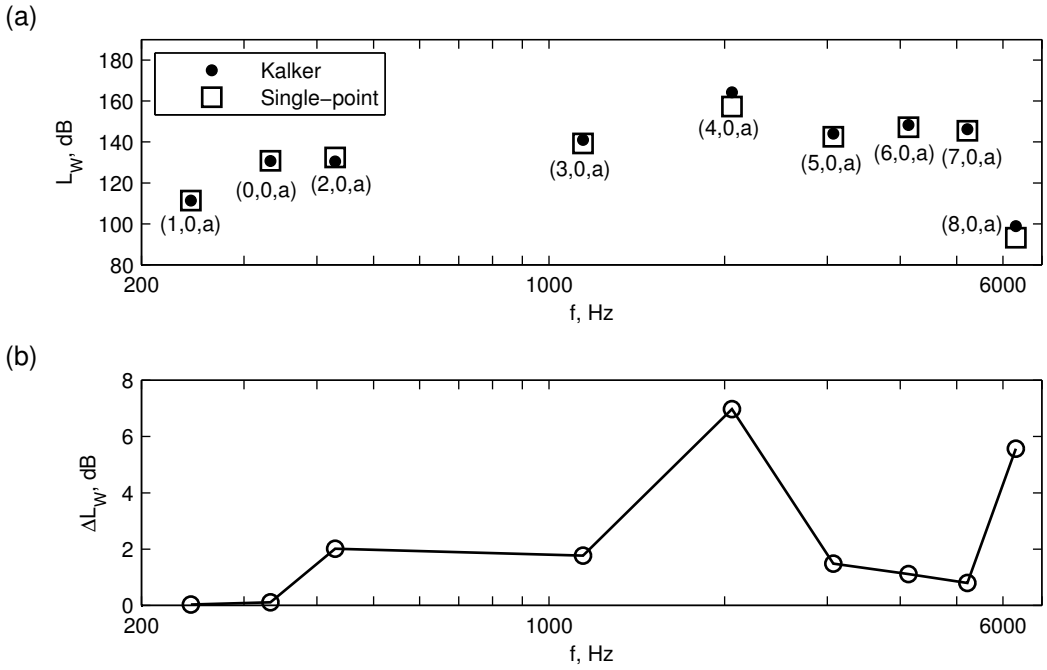

Figure 5.11: Results of the validation under dynamic conditions: (a) radiated sound-power levels: (•) Kalker, (□) point-contact model; (b) relative difference between the contact models.

The differences between the point-contact and Kalker's variational model are expressed in terms of the radiated sound power in Figure 5.11. The sound power is evaluated with the simple model for sound radiation (Section 4.4) for each dynamic validation case where squeal was obtained. In the evaluation of the sound radiation, the initial wheel model was retained with all modes included. A difference of around 2 dB between the contact models is observed in Figure 5.11 (b) for most cases. Two cases, at modes $(4, 0, a)$ and $(8, 0, a)$, show high differences in the overall radiated sound power. The difference occuring at mode $(4, 0, a)$ cannot be attributed to the force-amplitude difference, which is relatively low at that mode (see Figure 5.10). The large power-level difference at mode $(4, 0, a)$ is due to the differences in the lateral force amplitude spectrum obtained from the two contact models. Figure 5.12 shows a detail of the lateral force amplitude spectra. The peak in the lateral force spectrum obtained from Kalker's model is closer to the resonance peak in the

receptance. In comparison, the lateral force peak in the spectrum obtained from the point-contact model is further away from the resonance peak. The lateral force spectrum obtained from the squeal model with Kalker's contact model excites the wheel closer to the $(4, 0, a)$ eigen-frequency. This leads to a stronger vibration field on the wheel and, consequently, higher sound radiation observed in Figure 5.11.

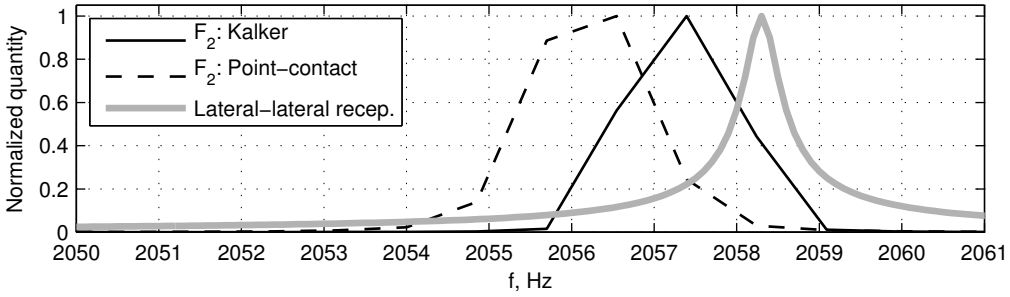

Figure 5.12: Amplitude spectra of the lateral contact force and lateral point receptance around the wheel mode $(4, 0, a)$: (— black) Kalker, (- - black) point-contact model, (— grey) lateral point receptance. Quantities are normalized with their maximum values.

Regarding the wheel mode $(8, 0, a)$, the difference in the force amplitude is high, leading to a high difference in the radiated sound power as well. However, the lateral force amplitude obtained with this mode is low, as is the radiated sound power. Because of the relatively small amplitudes, it is not possible to asses the validity of the tangential point-contact model for the $(8, 0, a)$ mode with certainty.

The presented validation results indicate that the wheel and rail dynamics put different demands on the contact model compared to the prescribed-motion case. In the prescribed-motion validation, the point-contact model shows high differences above 400 Hz. When used in the squeal model, acceptable results are obtained from the point-contact model for frequencies up to at least 5 kHz. The tangential point-contact model may be valid even for frequencies above 5 kHz, but only wheel modes up to 7 kHz are included in the model, which limits the validation. However, even below 5 kHz differences may still arise at certain wheel modes, which are most noticeable in the radiated sound power.

An additional validation case

This section is concluded with limitations of the dynamic validation procedure. The proposed validation method requires the definition of simulation parameters (nominal contact position, friction and creepage) of the squeal case used in the procedure. It is not known in advance whether the chosen parameter combination will result in a significant number of excited wheel modes during the validation procedure. This means that to obtain more information at different frequencies, squeal simulations with different parameters may be required.

The additional dynamic validation case presents a situation where the chosen squeal case gives useful information only up to 2 kHz. The squeal case parameters are: $\Delta y^{WR} = -10$ mm wheel/rail contact point, $\mu = 0.3$ friction coefficient, $\gamma_y = -0.01$ lateral creepage, $v = 50$ km/h vehicle velocity, $F_{L3} = 65$ kN vertical wheel pre-load and $\Delta t = 36$ μs simulation time-step length. Figure 5.13 (a) shows the p2p amplitude values of the lateral contact force, with numeric values presented in Table 5.3.

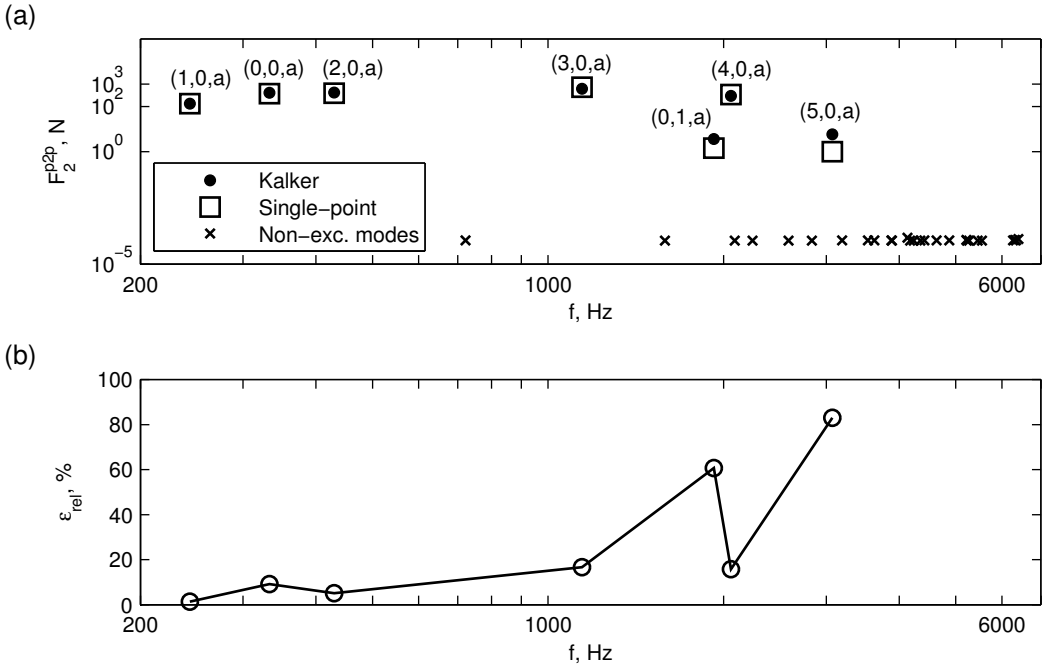

Figure 5.13: Additional dynamic validation case: (a) lateral contact-force p2p amplitudes: (•) Kalker, (□) point-contact model, (×) wheel modes that were not excited; (b) relative difference between the contact models.

Mode	f_r, Hz	K F_2^{p2p}, N	P F_2^{p2p}, N	L/a_x
$(1,0,a)$	243.2	133.8	135.7	4.76
$(0,0,a)$	332.8	407.4	369.9	3.48
$(2,0,a)$	429.9	416.4	394.9	2.69
$(3,0,a)$	1143.2	619	722	1.01
$(0,1,a)$*	1923.9	3.6	1.4	0.6
$(4,0,a)$	2058.3	294.2	340.7	0.56
$(5,0,a)$*	3070.8	5.8	1	0.38

Table 5.3: Numeric results of the additional dynamic validation case. The mode eigen-frequency, force p2p amplitudes and L/a_x ratios are given. * = modes resulting in low amplitudes; K = Kalker's model; P = point-contact model.

Significant differences are noticed when comparing the results of the additional case to results of the dynamic validation case of Figure 5.10. Not all axial wheel modes with zero nodal circles develop the instability and, additionally, the mode $(0, 1, a)$ is excited. Modes $(0, 1, a)$ and $(5, 0, a)$ show significant differences between Kalker's and the point-contact model results. These differences are presented in Figure 5.13 (b). Similarly to the case with mode $(8, 0, a)$ of Figure 5.10, low force-amplitude modes show high relative differences. Interestingly, the mode $(4, 0, a)$, with a frequency between the $(0, 1, a)$ and $(5, 0, a)$ mode frequencies, has a high force amplitude and a low relative difference. This indicates that modes with low force amplitudes should be approached with some caution.

The additional validation case does not give as much information as the case presented in Figure 5.10. From the additional case, the validity of the point-contact model is confirmed for frequencies up to at least 2 kHz. In the initial validation case the model was shown to be valid for up to at least 5 kHz. It is therefore preferable to validate a contact model on more cases to get a clearer picture of its behaviour under dynamic conditions.

5.2.3 Conclusion

The proposed contact model (Section 4.3) was validated against Kalker's variational contact model with a two-fold approach. First, the contact model was validated independently of the squeal model, with an imposed creepage variation. Secondly, the model was validated within the squeal model.

Results of the two validations point indicate that the two validation approaches put significantly different demands on the contact model. The validation with prescribed motion (Section 5.2.1) gives results which are in line with observations from the literature [9, 40]. In contrast, the results of the validation in dynamic conditions (Section 5.2.2) provide a completely different picture.

The squeal model with the tangential point-contact model predicts squeal occurrence equally well as the squeal model with Kalker's variational contact model. This is true even for high-frequency squeal, where the L/a_x ratio is significantly lower than ten and transient phenomena should be considered [40]. The obtained results also seem to support Kalker's statement that transient contact processes may be described as a succession of steady-states [37] (see discussion at the end of Section 3.2.1).

Results of the validation with prescribed motion do not indicate that the point-contact model would be able to describe the contact processes during squeal satisfactorily. The applicability of a contact model for squeal modelling should therefore not be judged solely on the basis of an imposed-motion (or imposed-force) validation. In conclusion, the applicability of a contact model for dynamic wheel/rail interaction modelling should be determined in conditions that replicate the real application as closely as possible.

Chapter 6

Parameter studies

In this chapter the proposed engineering model for squeal is used to investigate the influence of different parameters on curve squeal occurrence and amplitudes. The influence of the lateral creepage and friction coefficient on curve squeal occurrence and amplitudes is investigated in Section 6.1. Three different wheel/rail nominal contact points are used in the investigation. This enables for the influence of the vertical-lateral dynamics coupling to be determined as well.

The influence of wheel damping on curve squeal is investigated in Section 6.2. For each wheel mode excited in squeal the modal damping value for which squeal at that mode is eliminated is determined. This approach gives information about wheel modes that are susceptible to squeal, the severity of squeal related to each mode, and the damping required to eliminate squeal.

6.1 Lateral creepage/friction study

The vehicle curving behaviour has a direct influence on curve squeal by influencing the amount of lateral creepage and the wheel/rail contact position [56, 19, 72]. In addition, the friction in the wheel/rail contact area is another parameter that significantly influences squeal.

The combination of lateral creepage and friction defines the amount of input energy in the wheel/rail vibrating system. Moreover, the wheel/rail lateral contact position influences the amount of the vertical-lateral dynamics coupling, which is held responsible for squeal development (see Section 4.2.1, Figure 4.4). It is therefore expected that these kinematic and friction parameters have a significant influence on squeal occurrence and amplitudes. The aim of the present study is to investigate into more detail the influence of the mentioned parameters.

Both low and high values of the angle of attack, defining the amount of lateral creepage, were observed in practice [19, 77, 18]. In addition, the wheel/rail friction coefficient is difficult to measure, resulting in uncertainties with regards to its values. To account for the rather wide range of observed lateral creepage values and the

uncertainties in the friction coefficient, a relatively large parameter space is defined:

$$-0.06 \leq \gamma_y \leq -0.002, \qquad \Delta\gamma_y = 0.002, \tag{6.1}$$

$$0.1 \leq \mu \leq 0.6, \qquad \Delta\mu = 0.05. \tag{6.2}$$

The terms $\Delta\gamma_y$ and $\Delta\mu$ are the creepage and friction steps between adjacent values used in the study. Three wheel/rail contact positions are used in the study and are defined by Equation (4.1) in Section 4.1.1. Other simulations parameters common to all cases are: $v = 50$ km/h rolling velocity, $\Delta t = 36$ μs time-step length, $F_{L3} = 65$ kN vertical wheel pre-load and zero longitudinal and spin creepage ($\gamma_x = \gamma_\omega = 0$).

Simulations with the engineering squeal model were run until the limit cycle was achieved. However, a limit of eight seconds was set for the simulated rolling time. If the instability does not develop until the maximum time is reached, it is considered that squeal would not occur in practice. In addition, the sound radiation is computed for cases with a force rms level $L_{F_2} \geq 10$ dB rel. 1 N. Squeal with a lateral force level below 10 dB is not considered severe. The radiated sound power level and the sound frequency content are computed using the simple model for sound radiation described in Section 4.4.

Results of the squeal model are presented in terms of the lateral force rms[1] level L_{F_2},

$$L_{F_2} = 20 \log \left(\frac{F_2^{rms}}{1\ \mathrm{N}} \right). \tag{6.3}$$

The rms value of the lateral contact force is determined from n_s samples of the force time history as

$$F_2^{rms} = \sqrt{\frac{1}{n_s} \sum_{t=t_d}^{t_d+(n_s-1)\Delta t} \left(F_2(t) - \bar{F}_2 \right)^2}, \tag{6.4}$$

where $\bar{F}_2$ is the mean value of the force in the considered time interval. By subtracting the mean value $\bar{F}_2$ of the lateral force, the dynamic lateral force is obtained. As a result, cases that do not develop squeal, or where the lateral force approaches a constant value, have zero or very low values of the force rms level. The dominant frequency of the force response is determined as well.

6.1.1 Contact position $\Delta y^{WR} = -5$ mm

Results of the parameter study for the contact position $\Delta y^{WR} = -5$ mm are presented in Figure 6.1. The figure presents the lateral force rms levels, the dominant force-response frequency, the radiated sound power levels and the dominant sound frequency for each simulated case. Squeal does not develop for low lateral creepage and friction values, see Figure 6.1 (a) and (c). With increasing values of creepage and friction friction both lateral force and sound power levels are seen to increase considerably.

[1]The "rms" abbreviation stands for "root mean square", also known as the quadratic mean.

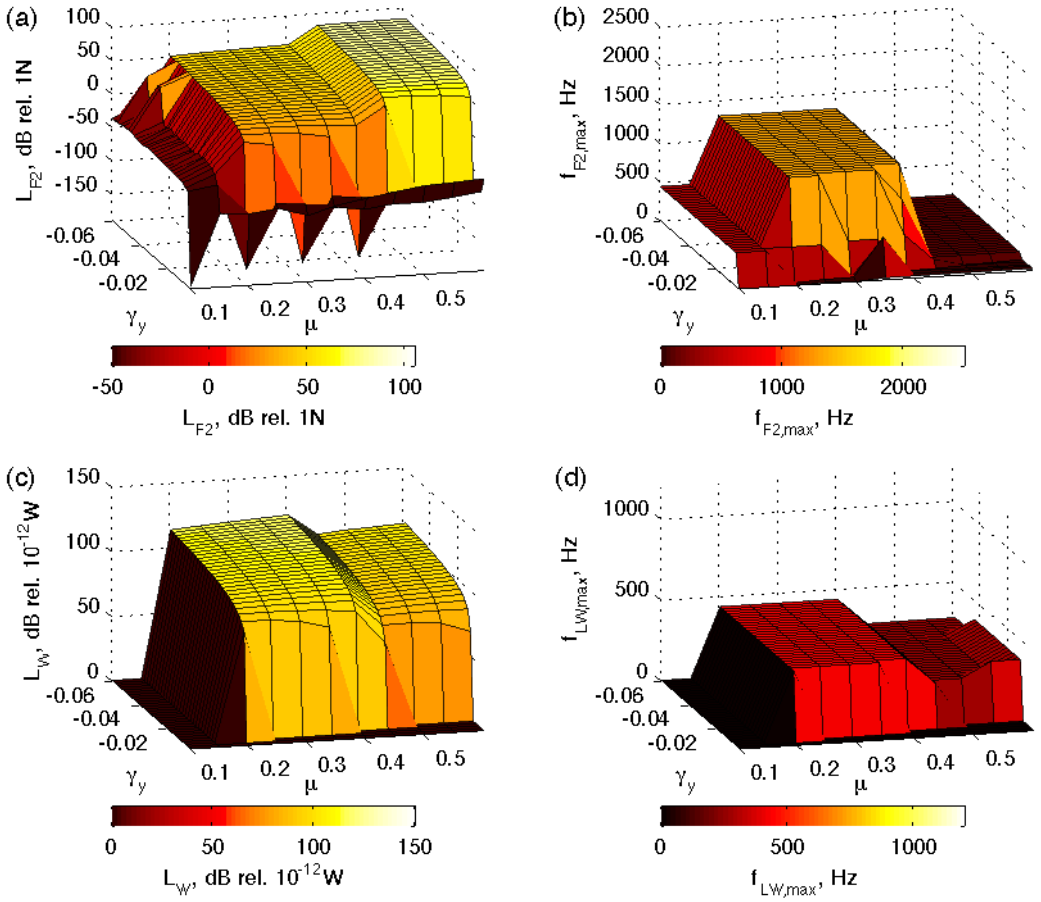

Figure 6.1: Contact position $\Delta y^{WR} = -5$ mm: (a) lateral force amplitude rms levels; (b) dominant response frequency of the contact force; (c) radiated sound power levels; (d) dominant frequency of the radiated sound.

In Figure 6.1 (b), three different frequencies dominate in the lateral force response. The 434 and 1292 Hz frequencies correspond to the eigen-frequency and the third harmonic of the $(2, 0, a)$ wheel mode ($f_r = 429.9$ Hz). The presence of higher harmonics is a consequence of the non-linear behaviour of the system [23].

The instability occurring at around 90 Hz results in considerably higher force levels. This type of instability takes place for friction values above 0.45, which is seen in Figure 6.1 (a) and (b). The primary vertical suspension of the wheelset is found responsible for this instability. Once the vertical suspension damping is sufficiently increased, the 90 Hz instability disappears. A similar vibrational phenomenon was already investigated within the context of rail corrugation by Kurzeck [45].

Results for the radiated sound presented in Figure 6.1 (c) and (d) show the importance of wheel modes in sound radiation. The dominant sound frequency (see Figure 6.1 (d)) is, in the investigated cases, coincident with a wheel mode eigen-frequency and not its higher harmonics. Axial wheel modes are especially efficient at sound radiation [74]. The excited $(2, 0, a)$ wheel mode results in relatively high

radiated sound power levels in the order of $L_W \approx 100 \ldots 120$ dB. In comparison, cases developing suspension-related vibrations radiate significantly less sound ($L_W \approx 90 \ldots 106$ dB), despite having higher force levels.

6.1.2 Contact position $\Delta y^{WR} = -10$ mm

Results of the parameter study for the contact position $\Delta y^{WR} = -10$ mm are given in Figure 6.2. It is seen that friction does not influence significantly the occurrence of squeal. However, the influence of lateral creepage is still present.

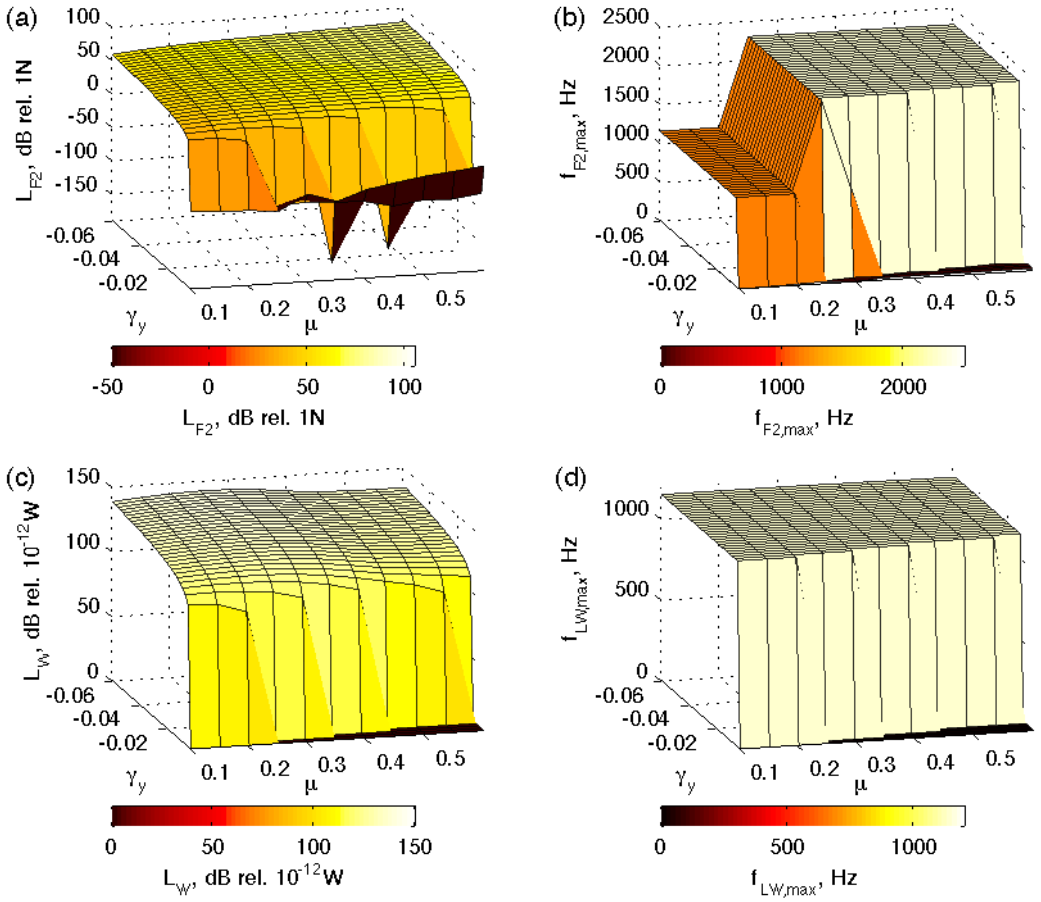

Figure 6.2: Contact position $\Delta y^{WR} = -10$ mm: (a) lateral force amplitude rms levels; (b) dominant response frequency of the contact force; (c) radiated sound power levels; (d) dominant frequency of the radiated sound.

The different contact position leads to the excitation of the $(3, 0, a)$ wheel mode ($f_r = 1143.2$ Hz). The force responds with two dominant frequencies, either 1143 Hz or 2282 Hz, see Figure 6.2 (b). These frequencies correspond to the $(3, 0, a)$ mode eigen-frequency and its second harmonic.

The radiated sound power, Figure 6.2 (c), shows very high radiated sound power

levels in the order of $L_W \approx 120 \ldots 140$ dB. The dominant sound frequency corresponds to the squealing wheel mode eigen-frequency, see Figure 6.2 (d).

Different behaviour between the lateral force and the sound power levels is noticed when comparing Figure 6.2 (a) with Figure 6.2 (c). The force levels increase with increasing friction, while the sound power levels show a maximum around 0.25 friction coefficient. To explain this, the forces amplitude spectra have to be considered in relation to the wheel receptance. The resonance peaks in the wheel receptance are very narrow. Maximum sound radiation is obtained when a peak in the excitation force spectrum is coincident with a resonance peak. This is explained for two simulation cases on Figure 6.3.

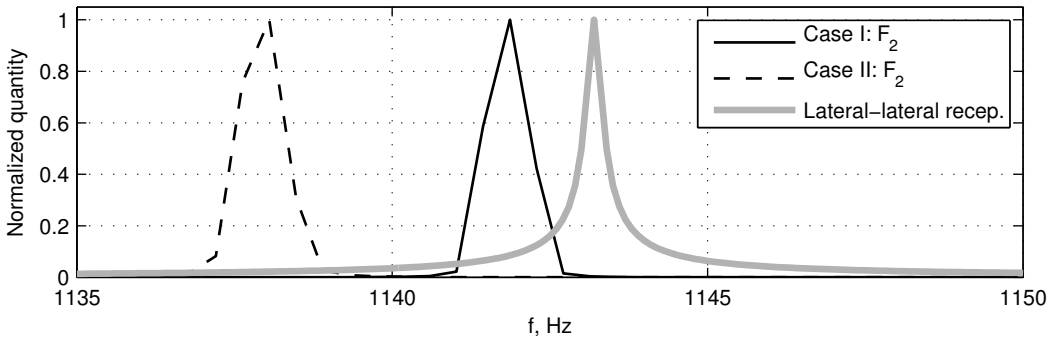

Figure 6.3: Amplitude spectra of the lateral force and lateral point receptance around the wheel mode $(3, 0, a)$ eigen-frequency. Case I (— black): $\mu = 0.25$, $\gamma_y = -0.04$. Case II (- - black): $\mu = 0.55$, $\gamma_y = -0.04$. Lateral point receptance (— grey). Quantities are normalized with their maximum values.

Case I in Figure 6.3 has a peak in the force spectrum close to a resonance peak in the receptance. The friction value in Case I is 0.25. A shift away from the resonance peak is noticed in the force spectrum of Case II, which has a friction value of 0.55. Both cases have the same lateral creepage value of -0.04. Because of the shift in the force spectrum, Case II results in lower sound power levels compared to Case I. A 7 dB higher sound power level is obtained in Case I, despite it having a 10 dB lower lateral force level than Case II (see Figures 6.2 (a) and (c)).

6.1.3 Contact position $\Delta y^{WR} = -15$ mm

Results of the parameter study for the $\Delta y^{WR} = -15$ mm contact position are presented in Figure 6.4. The friction and lateral creepage influence is similar to the influence observed in the $\Delta y^{WR} = -5$ mm position results in Figure 6.1.

The force-response dominant frequencies in Figure 6.4 (b) are consistent with the $(2, 0, a)$ wheel mode for all studied cases. The same observation is valid for the dominant sound frequency presented in Figure 6.4 (d). The radiated sound power is in the order of $L_W \approx 120 \ldots 140$ dB, comparable to results of the $\Delta y^{WR} = -10$ mm position. A maximum in the sound power occurs for 0.3 friction value.

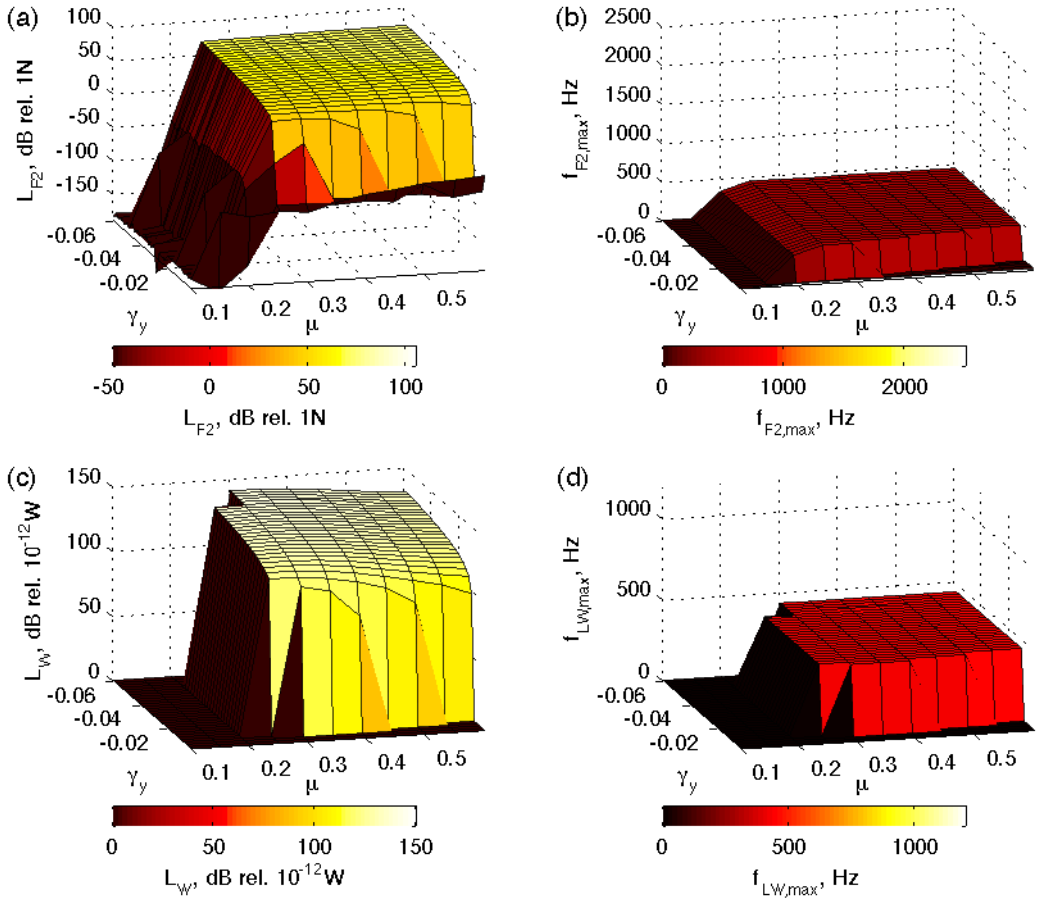

Figure 6.4: Contact position $\Delta y^{WR} = -15$ mm: (a) lateral force amplitude rms levels; (b) dominant response frequency of the contact force; (c) radiated sound power levels; (d) dominant frequency of the radiated sound.

6.1.4 Discussion

A strong influence of the wheel/rail contact position is seen from results presented in Section 6.1.1, 6.1.2 and 6.1.3. The contact position influences the contact area size and shape, as well as the wheel vertical-lateral dynamics coupling (see Figure 4.4 (c)). The vertical-lateral dynamics, which define the geometric coupling strength, are a very important factor in squeal. The coupling dynamics have a strong influence on which wheel mode is excited into squeal. These also influence the radiated sound power levels.

The maxima observed in the results for the sound power levels are a consequence of the wheel/rail friction. Friction influences squeal frequencies by slightly shifting the system response frequency, as shown on Figure 6.3. Mathematically, an increase in friction can be interpreted as additional damping in the wheel/rail system. In a single-degree-of-freedom system, an increase in damping will cause a decrease in the system response frequency. Despite the great complexity of the wheel/rail system,

a similar behaviour can be expected. An increase in friction will cause the response of the wheel/rail system to shift towards lower frequency. This explains the shift observed in Figure 6.3.

The dominant sound frequency is, in the investigated cases, coincident with the excited mode eigen-frequency. This is a result of the high amplitudes of the vertical force, which has its dominant frequency component coincident with the excited mode eigen-frequency. Figure 6.5 presents an example of the time histories of the contact forces and the corresponding amplitude spectra. It is noticed that the vertical force has a significantly higher response at 430 Hz, which is the $(2, 0a)$ mode eigen-frequency. The higher harmonics in the vertical force are significantly lower than the fundamental. In comparison, the lateral force has maximum response at the third harmonic, but this maximum is not significantly higher than the response at other harmonics. In combination, the lateral and the vertical force excite the wheel most at a frequency close to the excited wheel mode eigen-frequency. The dominant frequency of the radiated sound is therefore coincident with the exited wheel mode eigen-frequency.

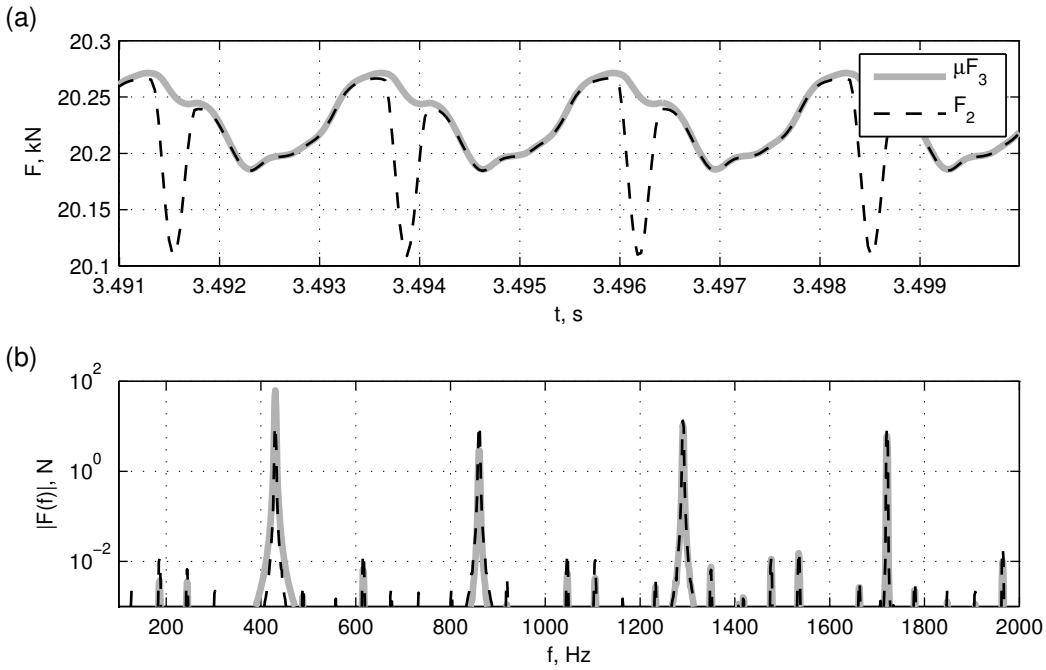

Figure 6.5: Simulation case $\Delta y^{WR} = -5$ mm, $\gamma_y = -0.012$, $\mu = 0.3$: (a) detail of contact forces response: (- - black) lateral force F_2; (— grey) vertical force multiplied by the friction coefficient, μF_3; (b) amplitude spectra of the contact forces: (- - black) lateral force; (— grey) vertical force.

In addition, it should be noted that stick-slip is best noticed in the lateral force response, which shows a sudden decrease when stick takes place. The vertical force shows less deviations from a purely sinusoidal shape than the lateral force response.

These deviations in the vertical force response are caused by the coupling between the vertical and lateral directions.

Results of contact positions $\Delta y^{WR} = -10$ mm and $\Delta y^{WR} = -15$ mm share similarities with respect to the lateral force and sound power levels. Compared to these positions, the $\Delta y^{WR} = -5$ mm position results have significantly lower levels. Differences of up to 20 dB in the sound power levels are noticed for the same simulation parameters. This further emphasizes the importance of the wheel/rail contact position.

In particular, the $\Delta y^{WR} = -10$ mm contact position is the most critical amongst the studied positions as squeal occurs even for low wheel/rail friction values. The application of friction modifiers in real situations with this contact position may not lead to improvements with regard to curve squeal levels. This partly explains the findings from the literature [18, 2], where squeal was not completely eliminated despite the application of friction modifiers. However, a change in the wheel/rail friction may influence the vehicle dynamics and result in a different, more favourable, contact position during curving. With so many different parameters and interconnected influences it is not surprising that mixed findings are encountered in both the literature and practice.

Interestingly, the contact position does not significantly influence the value of the lateral creepage threshold, which is the minimum lateral creepage value above which squeal occurs. Instead, this threshold shows a stronger dependence on the friction value and increases with increasing friction. This may be another consequence of the additional damping introduced by friction.

The creepage/friction parameter study demonstrated that wheel/rail kinematic and friction parameters are very important to the occurrence and amplitudes of squeal. The investigated parameter space is large and results are strongly dependent on the parameter combination.

Finally, only axial modes with zero nodal circles, $(2, 0, a)$ and $(3, 0, a)$ were found to be squealing. This observation is in accordance with findings presented in the contact model validation, Section 5.2.2.

6.2 Wheel modal damping study

As discussed in Section 2.3.2, wheel damping is often applied to mitigate curve squeal and rolling noise. This approach makes sense, as the railway wheel is the main sound radiator in curve squeal and a significant contributor to higher-frequency (above 1 kHz) rolling noise [72]. However, to the author's knowledge, no studies about the influence of wheel damping on curve squeal frequencies and amplitudes exist in the literature. The aim of this section is to investigate the relationship between wheel modal damping and the occurrence, amplitude and frequency of squeal.

Figure 6.6 shows the procedure of the modal damping study. The procedure starts by defining the parameters of the squeal case under investigation. For the given parameters, squeal is simulated using the engineering model and results are

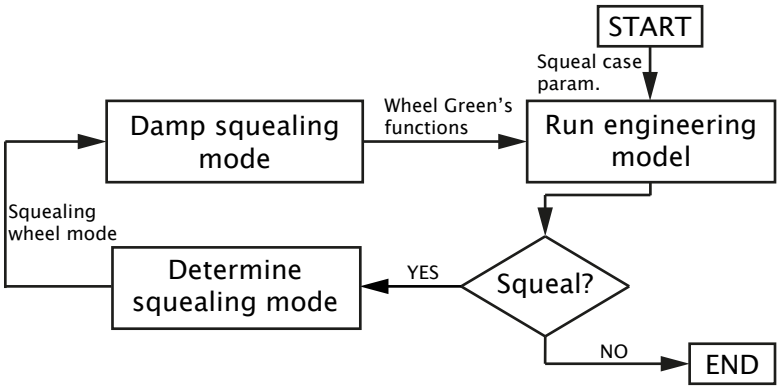

Figure 6.6: Procedure of the wheel modal damping study.

obtained in terms of the lateral contact force. The results are then analysed to determine whether squeal occurs or not. If squeal occurs, the wheel mode responsible for squeal is identified, along with the damping factor value for which squeal is eliminated at that mode. The determined damping factor value is referred to as the "squeal-critical" modal damping factor.

In the next step, the squeal case is simulated again, but with the modified wheel dynamics where the previously considered mode (or modes) is squeal-critically damped. The damping of other modes is set according to Equation (4.11). From the simulation results, the eventual squeal amplitude and frequency are determined. If squeal persists, the wheel mode excited in squeal is considered and its squeal-critical damping factor is determined. The described procedure is repeated as long as squeal switches to another mode after the squealing mode is damped.

The squeal-critical modal damping factor is determined in a procedure similar to the damping-study procedure of Figure 6.6. The main difference is that the wheel model is significantly changed for the purpose of determining the critical damping. Only the squealing wheel mode and the wheel suspension effects are included in the wheel dynamic response. The modal damping of the included mode is gradually increased until squeal does not occur in the simulations any more. The squeal-critical damping of the considered mode is then used in the wheel model that includes all wheel modes and the new wheel Green's functions are obtained.

Δy^{WR}, mm	μ	γ_y	Results
-15	0.25	-0.012	Figure 6.7
-15	0.25	-0.04	Figure 6.8
-15	0.4	-0.012	Figure 6.9
-15	0.4	-0.04	Figure 6.10
-15	0.6	-0.012	Figure 6.11
-15	0.6	-0.04	Figure 6.12

Table 6.1: Squeal cases used in the wheel modal damping study.

The study is conducted on squeal cases defined in Table 6.1. A combination of cases with moderate and high friction coefficient values is chosen, along with moderate and high lateral creepage values. All cases have the same nominal contact position $\Delta y^{WR} = -15$ mm.

Study results for each squeal case and each squealing mode are presented in terms of the lateral force rms-level L_{F_2} and the squeal-critical modal damping factor ζ_{sq}. Each result series, which gives the results for one squeal case, begins with the results of the initial squeal simulation with the original wheel dynamics. The next result point gives the results of the simulation with the altered wheel dynamics, where the previously squealing mode(s) is squeal-critically damped. This progression of results (and squeal) is indicated by arrows in the force rms-level plots. Figure 6.7 to 6.12 show the results of the damping study, with the numerical values of the squeal-critical damping factor and the mode frequency given as well.

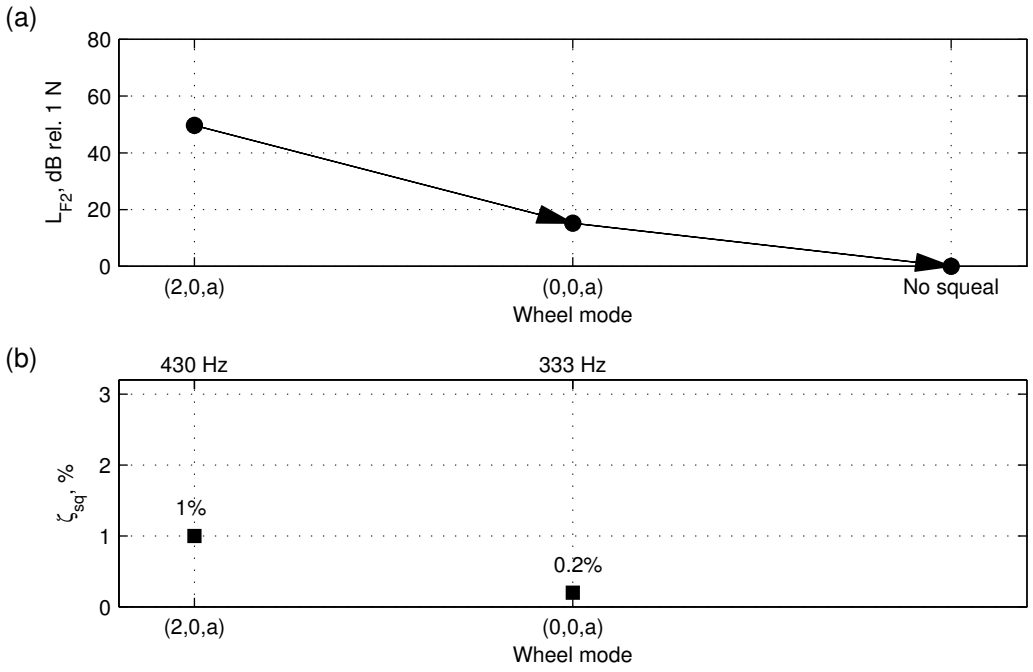

Figure 6.7: Squeal case $\mu = 0.25$, $\gamma_y = -0.012$ damping study results: (a) lateral contact-force rms levels corresponding to excited wheel modes; (b) squeal-critical modal damping factors of excited wheel modes.

The friction coefficient has a significant influence on the number of wheel modes that are successively excited into squeal. The cases with $\mu = 0.25$ friction, presented in Figures 6.7 and 6.8, show a relatively simple behaviour. Squeal moves only once, to wheel mode $(0, 0, a)$ with significantly lower force amplitudes. After the $(0, 0, a)$ mode is critically damped, squeal is completely eliminated. Low friction cases require low values of modal damping for squeal to be eliminated at the excited mode. In contrast, cases with friction coefficient values $\mu = 0.4$ (Figures 6.9 and 6.10) and $\mu = 0.6$ (Figures 6.11 and 6.12) show a more complex behaviour. Squeal successively

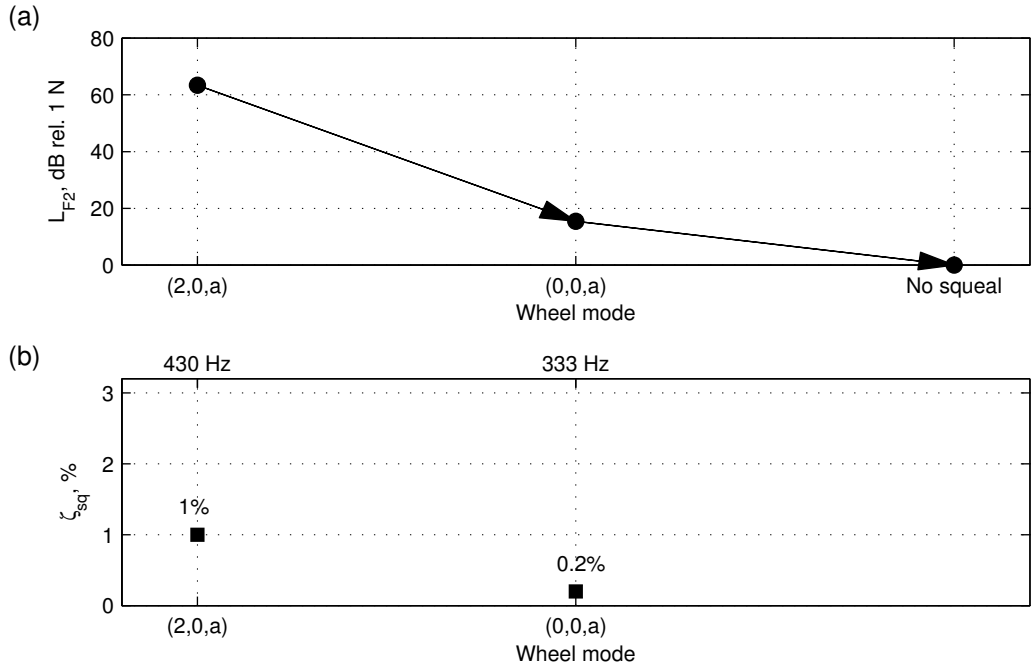

Figure 6.8: Squeal case $\mu = 0.25$, $\gamma_y = -0.04$ damping study results: (a) lateral contact-force rms levels corresponding to excited wheel modes; (b) squeal-critical modal damping factors of excited wheel modes.

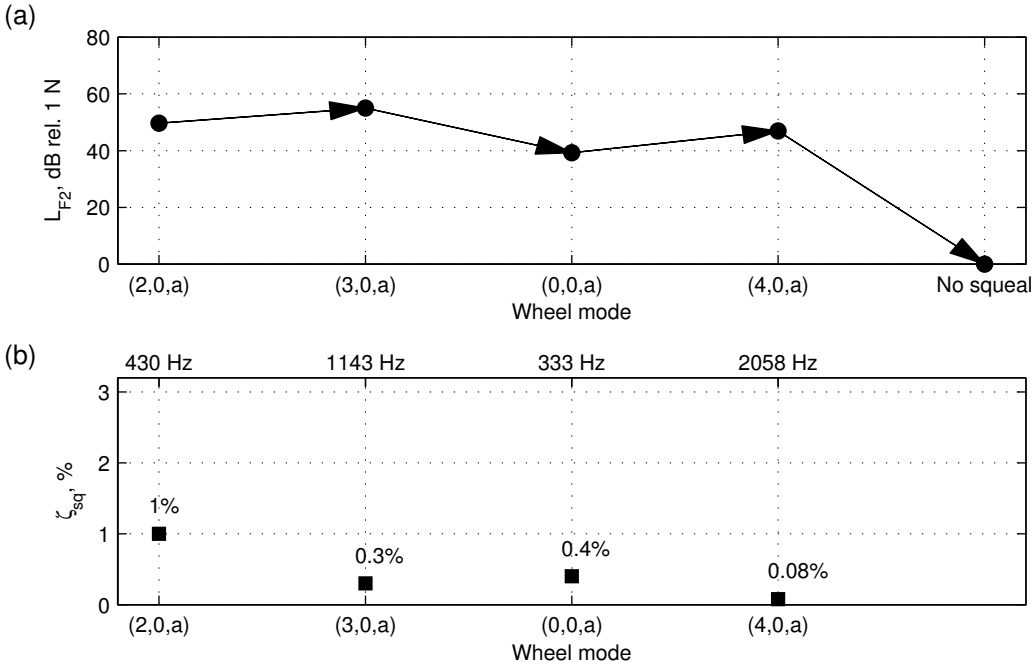

Figure 6.9: Squeal case $\mu = 0.4$, $\gamma_y = -0.012$ damping study results: (a) lateral contact-force rms levels corresponding to excited wheel modes; (b) squeal-critical modal damping factors of excited wheel modes.

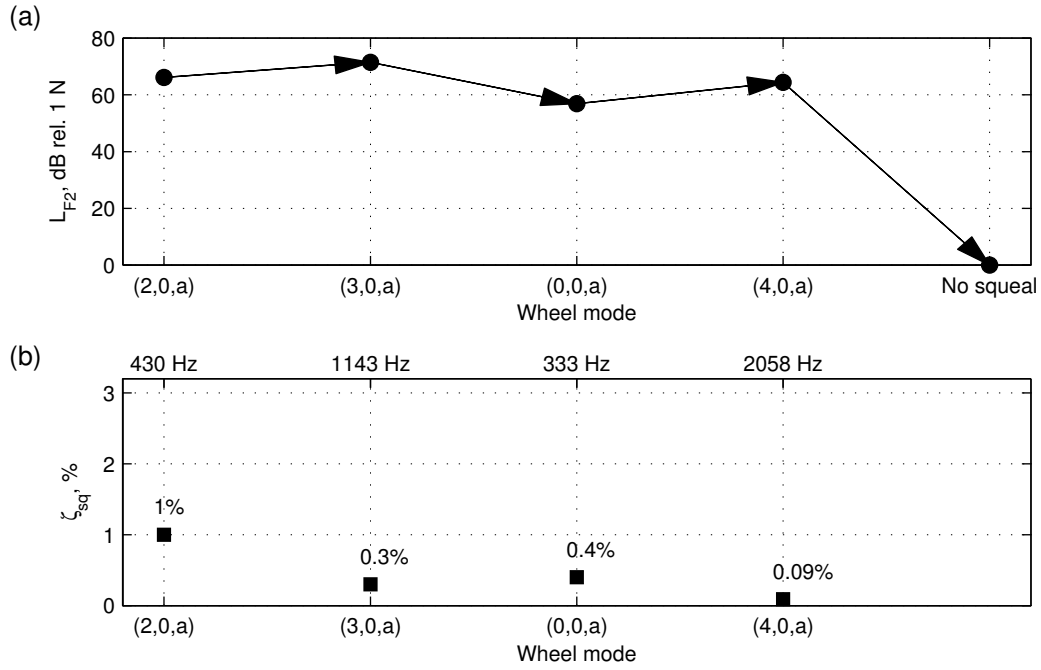

Figure 6.10: Squeal case $\mu = 0.4$, $\gamma_y = -0.04$ damping study results: (a) lateral contact-force rms levels corresponding to excited wheel modes; (b) squeal-critical modal damping factors of excited wheel modes.

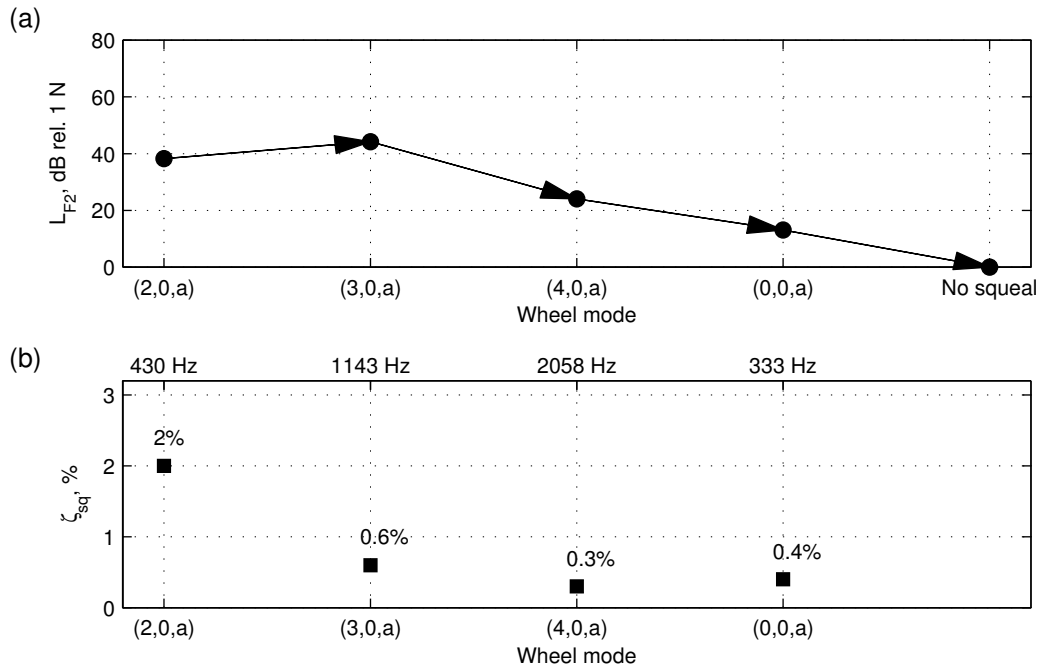

Figure 6.11: Squeal case $\mu = 0.6$, $\gamma_y = -0.012$ damping study results: (a) lateral contact-force rms levels corresponding to excited wheel modes; (b) squeal-critical modal damping factors of excited wheel modes.

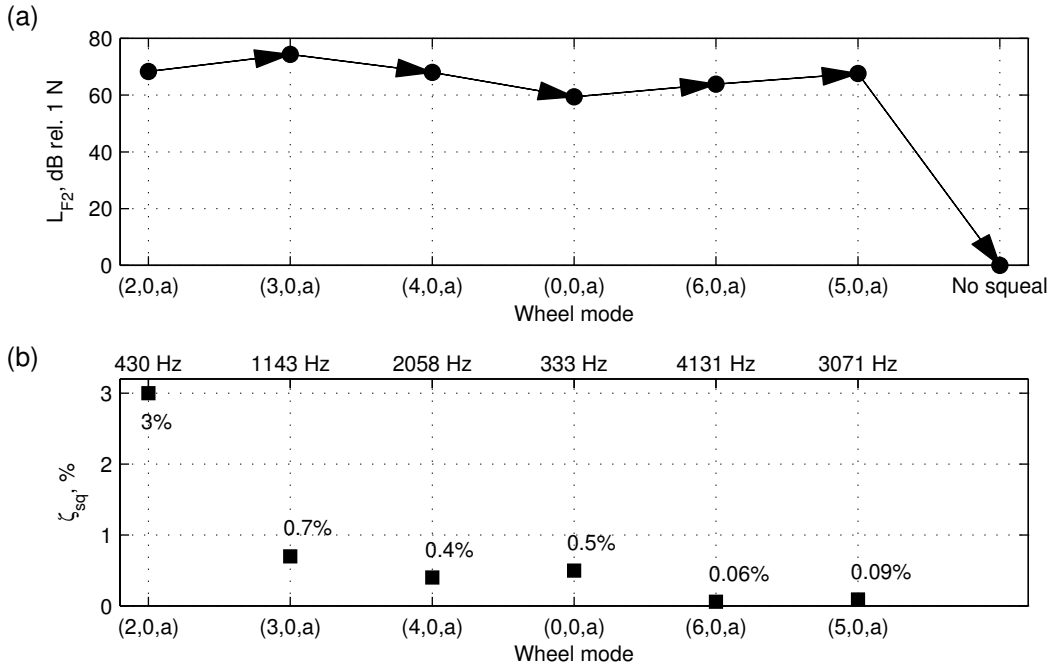

Figure 6.12: Squeal case $\mu = 0.6$, $\gamma_y = -0.04$ damping study results: (a) lateral contact-force rms levels corresponding to excited wheel modes; (b) squeal-critical modal damping factors of excited wheel modes.

moves from one axial mode with zero nodal circles to another. During the analysis of the rather extreme squeal case $\mu = 0.6$ and $\gamma_y = -0.04$ (Figure 6.12), six modes are successively excited into squeal. Moreover, the lateral force level does not necessarily decrease as squeal moves to another wheel mode.

The friction coefficient shows a strong influence on the results and higher friction leads to a higher number of wheel modes that are susceptible to squeal. In contrast, the influence of the lateral creepage is significantly lower. Higher lateral creepage, in most cases, leads to higher lateral force levels during squeal. Only in high-friction case ($\mu = 0.6$) does a high increase in creepage lead to more modes being susceptible to squeal, which can be seen by comparing Figures 6.11 and 6.12. A possible explanation is that the friction coefficient has a stronger influence on the energy input in the system than lateral creepage.

The squeal-critical damping factor is relatively low for the $\mu = 0.4$ and $\mu = 0.25$ squeal cases, but slightly higher for cases with $\mu = 0.6$ friction. In addition to defining the energy input, friction may be considered to influence the vertical-lateral coupling dynamics, where higher friction strengthens the coupling. Still, this does not completely explain the influence of friction on the presented results. Significant uncertainties concerning the influence of friction on curve squeal remain, and more research is required in order to develop a clear understanding.

Table 6.2 presents the succession of wheel modes that are excited into squeal for each squeal case. The importance of wheel/rail friction is also seen from the table.

Cases with $\mu = 0.4$ and $\mu = 0.6$ result in a slightly different succession of excited modes. The same wheel modes are excited, but for higher friction mode $(4, 0, a)$ precedes mode $(0, 0, a)$. With the exception of the $(0, 0, a)$ mode, squeal successively moves to higher frequencies in both cases.

μ	γ_y	**Wheel-modes succession**
0.25	-0.012	$(2,0,a) \rightarrow (0,0,a)$
0.25	-0.04	$(2,0,a) \rightarrow (0,0,a)$
0.4	-0.012	$(2,0,a) \rightarrow (3,0,a) \rightarrow (0,0,a) \rightarrow (4,0,a)$
0.4	-0.04	$(2,0,a) \rightarrow (3,0,a) \rightarrow (0,0,a) \rightarrow (4,0,a)$
0.6	-0.012	$(2,0,a) \rightarrow (3,0,a) \rightarrow (4,0,a) \rightarrow (0,0,a)$
0.6	-0.04	$(2,0,a) \rightarrow (3,0,a) \rightarrow (4,0,a) \rightarrow (0,0,a) \rightarrow (6,0,a)$ $\rightarrow (5,0,a)$

Table 6.2: Succession of excited wheel modes for squeal cases considered in the wheel modal damping study.

The presented results indicate that squeal is easier to mitigate and even completely eliminate for cases with moderate to high friction. In extreme cases the damping treatment has to increase the modal damping of a significant number of modes. Ideally, all wheel modes considered susceptible to squeal (axial modes with zero nodal circles) should be damped. A favourable finding is that the amount of wheel damping required to eliminate squeal is relatively low, which supports Thompson's claim [72]. These damping values should be easily achievable in practice. Moreover, the critical damping of the initially squealing mode is, in the investigated squeal cases, higher than the damping of subsequently squealing modes. In practice, it may be enough to damp the initially squealing mode as that may also increase the damping of other wheel modes. However, this may not always be the case as squeal was observed even when resilient wheels were used [2].

When squeal moves to another wheel mode the force rms level does not necessarily decrease. Cases with force amplitudes that are higher than the initial ones are commonly observed in the study. However, in the present study a small number of cases was analysed and general conclusions should not be drawn. A more extensive study should be performed that involves different nominal wheel/rail contact positions and a larger sample of squeal cases. This study may lead to a more accurate determination of the influence of friction and creepage. The extensive study was not carried out in the present work because the procedure is very time-consuming and requires a significant number of iterations. Still, the performed study gives interesting insights into the behaviour of curve squeal.

Chapter 7

Conclusions and future work

7.1 Conclusions

In this thesis, a model for curve squeal in the time domain has been presented. The model is suitable for use in engineering practice because it is computationally efficient and addresses the complete chain, from source to radiated sound power.

The starting point of this thesis is the high-frequency wheel/rail interaction model developed by Pieringer [55, 56]. The central features of Pieringer's squeal model is the Green's functions approach and the use of Kalker's variational contact model [37]. On the one hand, Green's functions enable the inclusion of any linear wheel and rail model and result in fast time-domain computations in contrast to numerical integration techniques. On the other hand, the computational cost associated with Kalker's variational contact model is high. This makes Pieringer's model impractical for everyday engineering use due to the long computation times.

To make the model suitable for engineering practice several modifications and extensions are introduced. The tangential-contact model is identified as the greatest factor affecting the computational cost. Kalker's variational contact model for normal contact is not as computationally expensive and was retained because it enables the consideration of non-Hertzian contacts. Therefore, effort was put into developing a tangential point-contact model that would give acceptable results in the squeal model, but with significantly improved computation times. The tangential point-contact model considers the contact variables in a global manner. This is in contrast to Kalker's variational theory [37], which models contact processes on the contact-particle level.

The engineering model for curve squeal is completed by implementing a computationally efficient model for sound radiation from the railway wheel, which was developed by Thompson and Jones [74]. The model implementation is shown to be valid by comparing the simple-model results against BEM computations.

The proposed tangential point-contact model requires the wheel/rail friction model to be defined in a stringent manner. The global friction model has to ac-

count for the friction properties of the complete contact area. This is in strong contrast to the Coulomb friction model used in Kalker's contact model, which is a local friction model that defines friction properties between contact particles. The global friction model, called regularized friction is obtained using Kalker's model for each geometry of the surfaces in contact and friction coefficient value. The regularized friction model describes the transition from the full-stick conditions in the contact towards full-slip conditions.

Besides the friction model, the point-contact model requires a suitable definition of the contact compliances in the tangential directions. The contact compliances are determined in a stringent manner from the elastic half-space. The tangential contact spring is non-linear and depends on the actual force value.

According to Knothe and Groß-Thebing [40], to properly describe transient processes a contact model should be able to describe the change of contact variables within the contact area. According to that definition, the tangential point-contact model is not a transient contact model. Because of the global consideration of the contact, the point-contact model cannot describe the variation of contact variables within the contact area. However, the validation of the point-contact model against Kalker's variational model shows that the point-contact model can be used for transient problems.

To determine the applicability of a contact model for dynamic wheel/rail interaction modelling, a two-fold validation procedure is proposed. Firstly, the model is validated independently with a prescribed motion (stand-alone validation). The prescribed wheel/rail motion equates to the case with prescribed creepage (or force). Secondly, the model is validated with the system dynamics defining the input to the contact model (validation in dynamic conditions). The wheel dynamics was changed to influence the response frequency of the system, and evaluate the model at different frequencies.

The stand-alone validation of the point-contact model against Kalker's variational model shows significant differences already at 400 Hz, where the steady-state nature of the point-contact model starts to influence results. In contrast, the validation in dynamic conditions shows that the model gives acceptable results up to at least 5 kHz. The engineering model for squeal is, in addition, able to predict the occurence of squeal as equally well as Pieringer's model [55, 56]. The results of the two validation approaches indicate that the inclusion of the system dynamics puts significantly different demands on the contact model than the prescribed-motion case. When the system dynamics are included, the contact model input is variable and depends on the system response and the contact forces. The observations from the two validation procedures lead to an important conclusion: the applicability of a contact model for dynamic wheel/rail interaction modelling should be determined in conditions that replicate the real application as closely as possible.

A study of the influence of kinematic parameters and friction was carried out using the proposed engineering model. The kinematic parameters investigated are lateral creepage and the wheel/rail lateral contact position, which are parameters related to the vehicle curving behaviour. The study demonstrated that wheel/rail

kinematic parameters and friction are very important for the occurrence and amplitude of squeal. The lateral wheel/rail contact position which influences the vertical-lateral geometric coupling strength is especially important. This coupling is held responsible for the development of squeal. For one of the investigated contact positions squeal occurs even for low wheel/rail friction values. In this case the application of friction modifiers is not expected to provide benefits. Instead, solutions have to be sought through improvements in the vehicle curving behaviour. In addition, it is also seen that wheel/rail friction introduces additional damping in the system. For higher friction, the lateral creepage value above which squeal occurs increases. However, once the creepage threshold value is reached, squeal is more severe than for lower wheel/rail friction values.

The wheel is generally recognized to be the most significant sound radiator in curve squeal. A parameter study of the wheel modal damping influence on curve squeal occurrence and amplitudes has therefore been carried out. Squeal amplitudes are quantified using the lateral force rms levels. Despite the rather limited study interesting conclusions are drawn from the results. In the investigated cases, the wheel/rail friction shows a strong influence on the number of wheel modes that are susceptible to squeal. In contrast, the influence of lateral creepage is significantly lower, but in combination with high friction, high creepage can lead to more wheel modes becoming susceptible to squeal. Concerning the mitigation of curve squeal, it is easier to eliminate squeal for cases with low to moderate friction. The modal damping values required to eliminate squeal are, in the investigated cases, rather low (3% and lower). However, the wheel damping treatment should increase the damping of the wheel modes found susceptible to squeal in the considered squeal case. If only the initially squealing wheel mode is damped, squeal may move to another mode with another frequency and amplitude. The amplitude does not necessarily decrease as squeal moves to another wheel mode. The findings of the wheel modal damping study partially explain why resilient wheels do not eliminate squeal in all cases, as was observed in practice [2].

Summing up, the development, validation and application of an engineering model for curve squeal in the time domain has been presented. The model allows for fast evaluations of curve squeal cases defined by the nominal contact position, lateral creepage and wheel/rail friction. Real non-Hertzian wheel/rail geometry can be considered along with any linear wheel and rail model. Moreover, the model enables the evaluation of the radiated sound power from the railway wheel. Sound pressure levels at various distances from the wheel can then be obtained by post-processing the model results.

7.2 Future work

Feasible directions for future work can be divided into two categories: extensions to the contact model and extensions to the squeal model. Both categories are discussed in the following two sections.

7.2.1 Extensions of the contact model

Most interesting are extensions of the rolling contact model to include multi-point contact and to be able to model conformal contact. Both extensions would provide a significant advance in the modelling of wheel/rail interaction.

Multi-point contact is the case when multiple contact points exist between the wheel and the rail. This situation usually arises in very tight curves when the wheel flange comes into contact with the rail gauge corner. Under these conditions two contact points may coexist: wheel tread/rail head contact and wheel flange/rail gauge corner contact. Though commonly considered that flange contact mitigates squeal, some cases were reported where severe squeal occurs in conjunction with flange contact [18]. The occurrence of multiple contacts between wheel and rail may alter the system dynamics significantly. Extensions of the contact model, but also to the squeal model, are therefore necessary to include multi-point contact.

Conformal contact is again related to flange contact. The wheel-flange thickness is comparable to the dimensions of the contact area, which makes the elastic half-space assumption invalid. For a proper and correct evaluation of the problem involving flange contact, the contact model should be extended to include conformal contact. One possibility is to extend Kalker's variational normal contact model for the case of conformal contact. Instead of the half-space influence coefficients, coefficients determined from a detailed FE model of the wheel and rail can be used.

7.2.2 Extensions of the squeal model

Extensions of the squeal model are assumed to lead to a higher degree of accuracy of the model results. In the engineering model, the contact angle is not taken into account along with the longitudinal dynamics of the wheel and rail. The extension of the squeal model to account for the contact angle would presumably lead to higher accuracy of the model and may even influence squeal results significantly. As it was seen, vertical-lateral dynamics coupling is very important to the generation of squeal. The contact angle is a parameter that is expected to influence that coupling further.

The proposed engineering model for squeal does not account for the longitudinal dynamics of the wheel and rail, and only cases with constant rolling velocity are investigated. The extension of the squeal model to include longitudinal dynamics would provide the opportunity to investigate the influence of longitudinal creepage on squeal. This would enable the consideration of curving cases with braking or traction of the vehicle.

Another aspect not considered in the engineering model is that creepage and the wheel/rail contact position may vary during the time the vehicle negotiates a curve. Both quantities should be available prior to squeal simulations and obtained from multi-body dynamics simulations of vehicle curving. While the inclusion of time-dependent creepage in the model is straightforward, the varying contact position is more complex to implement. The varying contact position requires the simultaneous

consideration of multiple sets of wheel and rail Green's functions. The displacement response has to be evaluated at all predicted contact positions on the wheel and rail. This is possible, but would result in a deterioration in the computational efficiency of the engineering model.

Moreover, a more detailed and extensive study of the wheel modal damping should be carried out. This would provide a clearer picture of the influence of lateral creepage and wheel/rail friction on curve squeal. The model results could then be validated by measurement of squeal generated from wheels with various damping treatments.

As it stands, the engineering model is not validated against field or laboratory measurements. The inclusion of some of the above mentioned extensions to the squeal and contact models would enable validation of the model by comparing simulations to existing measurements. The measurements performed on the Australian railway network [18] could be then used for the model validation. Therefore, the main directions of future work are to extend the contact model to include multi-point contact and for the squeal model to take into account the contact angle and longitudinal dynamics.

References

[1] Burden of disease from environmental noise - Quantification of healthy life years lost in Europe. Technical report, WHO, 2011.

[2] Railway noise Technical Measures Catalogue. Technical Report UIC003-01-04fe, UIC International Union of Railways, July 2013.

[3] Annual European Union greenhouse gas inventory 1990–2012 and inventory report 2014. Technical Report 09/2014, European Environment Agency, May 2014.

[4] A. Alonso and J. G. Giménez. Tangential problem solution for non-elliptical contact areas with the FastSim algorithm. *Vehicle System Dynamics*, 45(4):341–357, 2007.

[5] A. Alonso and J. G. Giménez. Non-steady state modelling of wheel-rail contact problem for the dynamics simulation of railway vehicles. *Vehicle System Dynamics*, 46(3):179–196, 2008.

[6] E. Andersson, M. Berg, and S. Stichel. *Rail Vehicle Dynamics*. Division of Rail Vehicles, KTH, Stockholm, 2007.

[7] P. Andersson. *Modelling Interfacial Details in Tyre/Road Contact - Adhesion Forces and Non-Linear Contact Stiffness*. PhD thesis, Department of Civil and Environmental Engineering, Chalmers University of Technology, Göteborg, Sweden, 2005.

[8] J. B. Ayasse and H. Chollet. Determination of the wheel rail contact patch in semi-Hertzian conditions. *Vehicle System Dynamics*, 43(3):161–172, 2005.

[9] L. Baeza, F. J. Fuenmayor, J. Carballeira, and A. Roda. Influence of the wheel-rail contact instationary process on contact parameters. *Journal of Strain Analysis for Engineering Design*, 42:377–387, 2007.

[10] M. L. Boas. *Mathematical Methods in the Physical Sciences*. John Wiley & Sons, third edition, 2006.

[11] H. Brick. *Application of the Boundary Element Method to combustion noise and half-space problems*. PhD thesis, Department of Civil and Environmental Engineering, Chalmers University of Technology, Göteborg, Sweden, 2009.

[12] J. F. Brunel, P. Dufrénoy, M. Naït, J. L. Muñoz, and F. Demilly. Transient model for curve squeal noise. *Journal of Sound and Vibration*, 293:204–218, 2006.

[13] F. W. Carter. On the Action of a Locomotive Driving Wheel. *Proceedings of the Royal Society of London. Series A*, 112(760):151–157, 1926.

[14] O. Chiello, J. B. Ayasse, N. Vincent, and J. R. Koch. Curve squeal of urban rolling stock—Part 3: Theoretical model. *Journal of Sound and Vibration*, 293:710–727, 2006.

[15] A. Cigada, S. Manzoni, and M. Vanali. Vibro-acoustic characterization of railway wheels. *Applied Acoustics*, 69:530–545, 2008.

[16] D. G. Crighton, A. P. Dowling, J. E. F. Williams, M. A. Heckl, and F. A. Leppington. *Modern Methods in Analytical Acoustics: Lecture Notes*. Springer, 1996.

[17] B. E. Croft. *The Development of Rail-head Acoustic Roughness*. PhD thesis, Institute of Sound and Vibration Research, University of Southampton, Southampton, United Kingdom, October 2009.

[18] D. Curley, D. C. Anderson, J. Jiang, and D. Hanson. Field trials of gauge face lubrication and top-of-rail friction modification for curve noise mitigation. In *Proceedings of the 11th IWRN, Uddevalla*, volume 2, pages 511–518, September 2013.

[19] F. G. de Beer, M. H. A. Janssens, and P. P. Koojiman. Squeal noise of rail-bound vehicles influenced by lateral contact position. *Journal of Sound and Vibration*, 267:497–507, 2003.

[20] EC. EU transport in figures - statistical pocketbook 2014, 2014.

[21] U. Fingberg. A model of wheel-rail squealing noise. *Journal of Sound and Vibration*, 143(3):365–377, 1990.

[22] J. G. Giménez, A. Alonso, and E. Gómez. Introduction of a friction coefficient dependent on the slip into the FastSim algorithm. *Vehicle System Dynamics*, 43(4):233–244, 2005.

[23] C. Glocker, E. Cataldi-Spinola, and R. I. Leine. Curve squealing of trains: Measurement, modelling and simulation. *Journal of Sound and Vibration*, 324:365–386, 2009.

[24] A. Gross-Thebing. Frequency-Dependent Creep Coefficients for Three-Dimensional Rolling Contact Problems. *Vehicle System Dynamics*, 18(6):359–374, 1989.

[25] A. Guiral, A. Alonso, L. Baeza, and J. G. Giménez. Non-steady state modelling of wheel-rail contact problem. *Vehicle System Dynamics*, 51(1):91–108, 2013.

[26] M. A. Heckl and I. D. Abrahams. Curve squeal of train wheels, part 1: mathematical model for its generation. *Journal of Sound and Vibration*, 229(3):669–693, 2000.

[27] M. A. Heckl and I. D. Abrahams. Curve squeal of train wheels, part 2: which wheel modes are prone to squeal? *Journal of Sound and Vibration*, 3(229):695–707, 2000.

[28] H. Hertz. Ueber die Berührung fester elastischer Körper. *Journal für reine und angewandte Mathematik*, 92:156–171, 1882.

[29] N. Hoffmann, M. Fischer, R. Allgaier, and L. Gaul. A minimal model for studying properties of the mode-coupling type instability in friction induced oscillations. *Mechanics Research Communications*, 29:197–205, 2002.

[30] S. S. Hsu, Z. Y. Huang, S. D. Iwnicki, D, C. J. C. Jones, G. Xie, and P. D. Allen. Experimental and theoretical investigation of railway curve squeal. *Proc. Inst. Mech. Eng., Part F: J. Rail and Rapid Transit*, 221:59–73, 2007.

[31] Z. Y. Huang, D. J. Thompson, and C. J. C. Jones. Squeal Prediction for a Bogied Vehicle in a Curve. *Notes on Numerical Fluid Mechanics*, 99:313–319, 2008.

[32] S. Iwnicki, S. Björklund, and R. Enblom. Wheel-rail contact mechanics. In R. Lewis and U. Olofsson, editors, *Wheel-Rail Interface Handbook*, chapter 3, pages 58–92. Woodhead Publishing, 2009.

[33] J. Jiang, D. C. Anderson, and R. Dwight. The mechanisms of curve squeal. In *Proceedings of the 11th IWRN, Uddevalla*, volume 2, pages 655–662, September 2013.

[34] K. L. Johnson. *Contact mechanics*. Cambridge University Press, 1985.

[35] J. J. Kalker. Survey of Wheel-Rail Rolling Contact Theory. *Vehicle System Dynamics*, 5:317–358, 1979.

[36] J. J. Kalker. A Fast Algorithm for the Simplified Theory of Rolling Contact. *Vehicle System Dynamics*, 11:1–13, 1982.

[37] J. J. Kalker. *Three-Dimensional Elastic Bodies in Rolling Contact*, volume 2 of *Solid mechanics and its applications*. Kluwer Academic Publishers, 1990.

[38] J. J. Kalker. Wheel-rail rolling contact theory. *Wear*, 144:243–261, 1991.

[39] K. Knothe and A. Gross-Thebing. Derivation of Frequency Dependent Creep Coefficients Based on an Elastic Half-Space Model. *Vehicle System Dynamics*, 15(3):133–153, 1986.

[40] K. Knothe and A. Gross-Thebing. Short wavelength rail corrugation and non-steady state contact mechanics. *Vehicle System Dynamics*, 46(1-2):49–66, 2008.

[41] K. Knothe, R. Wille, and B. W. Zastrau. Advanced Contact Mechanics - Road and Rail. *Vehicle System Dynamics*, 35(4-5):361–407, 2001.

[42] J. R. Koch, N. Vincent, H. Chollet, and O. Chiello. Curve squeal of urban rolling stock—Part 2: Parametric study on a 1/4 scale test rig. *Journal of Sound and Vibration*, 293:701–709, 2006.

[43] K. Kraft. Der Einfluß der Fahrgeschwindigkeit auf den Haftwert zwischen Rad und Scheine. *Archiv für Eisenbahntechnik*, 22:58–78, 1967.

[44] W. Kropp. *Ein Modell zur Beschreibung des Rollgeräusches eines unprofilierten Gürtelreifens auf rauher Strassenoberfläche*. PhD thesis, Fortschritt-Berichte Reihe 11, Nr 166, VDI Verlag, Düsseldorf, Germany, 1992.

[45] B. Kurzeck. Combined friction induced oscillations of wheelset and track during the curving of metros and their influence on corrugation. *Wear*, 271:299–310, 2011.

[46] R. Lewis and U. Olofsson. Basic tribology of the wheel-rail contact. In R. Lewis and U. Olofsson, editors, *Wheel-Rail Interface Handbook*, chapter 2, pages 34–57. Woodhead Publishing, 2009.

[47] G. Lundberg and H. Sjövall. Stress and deformation in elastic contacts. Göteborg, 1958.

[48] I. Merideño, J. Nieto, N. Gil-Negrete, A. Landaberea, and J. Iartza. Numerical vibro-acoustic analysis of railway wheels with and without damping solutions. *Noise Control Engineering Journal*, 60(4):458–472, 2012.

[49] A. D. Monk-Steel and D. J. Thompson. Models for railway curve squeal noise. In *VIII International Conference on Recent Advances in Structural Dynamics*, Southampton, United Kingdom, 14-16 July 2003.

[50] A. D. Monk-Steel, D. J. Thompson, F. G. de Beer, and M. H. A. Janssens. An investigation into the influence of longitudinal creepage on railway squeal noise due to lateral creepage. *Journal of Sound and Vibration*, 293:766–776, 2006.

[51] C. M. Nilsson, C. J. C. Jones, D. J. Thompson, and J. Ryue. A waveguide finite element and boundary element approach to calculating the sound radiated by railway and tram rails. *Journal of Sound and Vibration*, 321:813–836, 2009.

[52] A. Nordborg. Wheel/rail noise generation due to nonlinear effects and parametric excitation. *Journal of the Acoustical Society of America*, 111(4):1772–1781, 2002.

[53] B. Paul and J. Hashemi. Contact pressures on closely conforming elastic bodies. *Journal of Applied Mechanics*, 48(3):543–548, 1981.

[54] F. J. Periard. *Wheel-Rail Noise Generation: Curve Squealing by Trams*. PhD thesis, Delft University of Technology, Delft, Netherlands, 1998.

[55] A. Pieringer. *Time-domain modelling of high-frequency wheel/rail interaction*. PhD thesis, Department of Civil and Environmental Engineering, Chalmers University of Technology, Göteborg, Sweden, 2011.

[56] A. Pieringer. A numerical investigation of curve squeal in the case of constant wheel/rail friction. *Journal of Sound and Vibration*, 333(18):4295–4313, 2014.

[57] A. Pieringer, L. Baeza, and W. Kropp. Modelling of railway curve squeal including effects of wheel rotation. In *Proceedings of the 11th IWRN, Uddevalla*, volume 2, pages 479–486, September 2013.

[58] A. Pieringer, W. Kropp, and D. J. Thompson. nvestigation of the dynamic contact filter effect in vertical wheel/rail interaction using a 2D and a 3D non-Hertzian contact model. *Wear*, 271(1-2):328–338, 2011.

[59] J. Piotrowski and H. Chollet. Wheel-rail contact models for vehicle system dynamics including multi-point contact. *Vehicle System Dynamics*, 43(6-7):455–483, 2005.

[60] J. Piotrowski and W. Kik. A simplified model of wheel/rail contact mechanics for non-Hertzian problems and its application in rail vehicle dynamic simulations. *Vehicle System Dynamics*, 46(1-2):27–48, 2008.

[61] O. Polach. Creep forces in simulations of traction vehicles running on adhesion limit. *Wear*, 258:992–1000, 2005.

[62] P. J. Remington. Wheel/rail squeal and impact noise: What do we know? What we don't know? Where do we go from here? *Journal of Sound and Vibration*, 2(116):339–353, 1985.

[63] M. J. Rudd. Wheel/rail noise - Part II: Wheel squeal. *Journal of Sound and Vibration*, 46(3):381–394, 1976.

[64] E. Schneider and K. Popp. Noise generation in railway wheels due to rail-wheel contact forces. *Journal of Sound and Vibration*, 120(2):227–244, 1988.

[65] Z. Y. Shen, J. K. Hedrick, and J. A. Elkins. A Comparison of Alternative Creep Force Models for Rail Vehicle Dynamics Analysis. *Vehicle System Dynamics*, 12(1-3):79–83, 1983.

[66] Z. Y. Shen and Z. Li. A fast non-steady state creep force model based on the simplified theory. *Wear*, 191:242–244, 1996.

[67] J.-J. Sinou and L. Jézéquel. Mode coupling instability in friction-induced vibrations and its dependency on system parameters including damping. *European Journal of MechanicsA/Solids*, 26:106–122, 2007.

[68] T. R. Spurr. A Theory of Brake Squeal. *Proc. Inst. Mech. Eng., Part D: J. Automob. Eng.*, pages 33–52, 1961.

[69] G. Squicciarini, S. Usberti, A. Barbera, R. Corradi, and D. J. Thompson. Curve squeal in the presence of two wheel/rail contact points. In *Proceedings of the 11th IWRN, Uddevalla*, volume 2, pages 671–678, 2013.

[70] H. Stappenbeck. Das Kurvengeräusch der Strassenbahn - Möglichkeiten zu seiner Unterdrückung. *VDI Zeitschrift*, 96(6):171–175, 1954.

[71] D. J. Thompson. Wheel-Rail Noise Generation, Part II: Wheel Vibration. *Journal of Sound and Vibration*, 161(3):401–419, 1993.

[72] D. J. Thompson. *Railway Noise and Vibration: Mechanisms, Modelling and Means of Control*. Elsevier, Oxford, UK, 2009.

[73] D. J. Thompson, M. H. A. Janssens, and F. G. de Beer. Track-Wheel Interaction Noise Software Theoretical Manual. TNO-report HAG-RPT-990211, TNO Institute of Applied Physics, November 1999.

[74] D. J. Thompson and C. J. C. Jones. Sound radiation from a vibrating railway wheel. *Journal of Sound and Vibration*, 253(2):401–419, 2002.

[75] C. J. M. van Ruiten. Mechanism of squeal noise generated by trams. *Journal of Sound and Vibration*, 120(2):245–253, 1988.

[76] P. J. Vermeulen and K. L. Johnson. Contact of Nonspherical Elastic Bodies Transmitting Tangential Forces. *Transactions of the ASME, Journal of Applied Mechanics*, 31(E2):338–340, 1964.

[77] N. Vincent, J. R. Koch, H. Chollet, and J. Y. Guerder. Curve squeal of urban rolling stock—Part 1: State of the art and field measurements. *Journal of Sound and Vibration*, 293:691–700, 2006.

[78] E. A. H. Vollebregt. Numerical modeling of measured railway creep versus creep-force curves with CONTACT. *Wear*, 314:87–95, 2014.

[79] E. A. H. Vollebregt and H. M. Schuttelaars. Quasi-static analysis of two-dimensional rolling contact with slip-velocity dependent friction. *Journal of Sound and Vibration*, 331:2141–2155, 2012.

[80] E. A. H. Vollebregt and P. Wilders. FASTSIM2: a second-order accurate frictional rolling contact algorithm. *Computational Mechanics*, 47:105–116, 2011.

[81] G. Xie, P. D. Allen, S. D. Iwnicki, A. Alonso, D. J. Thompson, C. J. C. Jones, and Z. Y. Huang. Introduction of falling friction coefficients into curving calculations introduction of falling friction coefficients into curving calculations for studying curve squeal noise. *Vehicle System Dynamics*, 44(sup 1):261–271, 2006.

[82] W. Yan and D. Fischer. Applicability of the Hertz contact theory to rail-wheel contact problems. *Archive of Applied Mechanics*, 70(4):255–268, 2000.

[83] I. Zenzerovic, A. Pieringer, and W. Kropp. Towards an Engineering Model for Curve Squeal. In *Proceedings of the 11th IWRN, Uddevalla*, volume 2, pages 495–502, 2013.